DEVELOPMENT OF BIOMIMETIC HUMAN LUNG ALVEOLUS CHIP

Kun Man

Dissertation Prepared for the Degree of

DOCTOR OF PHILOSOPHY

UNIVERSITY OF NORTH TEXAS

May 2023

APPROVED:

Yong Yang, Major Professor
Narendra Dahotre, Committee Member
Moo-yeal Lee, Committee Member
Brian Meckes, Committee Member
Huaxiao Yang, Committee Member
Vijay Vaidyanathan, Chair of Department of Biomedical Engineering
Shengli Fu, Interim Dean of the College of Engineering
Victor Prybutok, Dean of the Toulouse Graduate School

Man, Kun. *Development of Biomimetic Human Lung Alveolus Chip*. Doctor of Philosophy (Biomedical Engineering), May 2023, 128 pp., 7 tables, 43 figures, numbered chapter references.

The potential of physiologically relevant in vitro cell culture models for studying physiological and pathophysiological phenomena has been widely recognized as replacements for animal and conventional in vitro models. To create models that accurately replicate the structure and function of tissues and organs, it is essential to comprehend the biophysical and mechanical features of the extracellular matrix (ECM) and incorporate them into the in vitro cell culture models. Therefore, we first aimed to investigate how nanotopography can modulate cell behaviors by studying cell behaviors on nanostructures of various aspect ratios on a cobalt-chromium-molybdenum (CoCrMo) alloy surface. We also explored the impact of nanofibrous membranes on the formation of alveolar epithelium, which is critical for lung alveolar interstitium chips. In addition, we investigated the effect of mechanical stretch on cell behaviors and focused on how the dimensionality of the stretch affects cell behaviors. To create physiologically relevant in vitro models based on our findings, we engineered a stem cell niche using a combination of nanofibrous membranes, mechanical stretch, and a soft substrate, and evaluated its impact on stem cell behaviors. Finally, we created a biomimetic human lung interstitium chip for application in physiological and pathophysiological in vitro studies.

ACKNOWLEDGEMENTS

First, I am deeply grateful to my advisor, Dr. Yong Yang, for his kind and continuous guidance, encouragement, and support throughout my Ph.D. journey. He introduced me to the world of biomedical engineering, and the experience and knowledge gained from working with him will continue to benefit me in the future.

I am thankful to Dr. Jiafeng Liu, Dr. Kai Wang, Dr. Qiang Wei, Laurence A. Blake, Yufeng Zhou, and Sooyeon Kang, for their help and support during my Ph.D. study. Thank Nhu Nguyen, Reagan Stewart, Jung Yeon Lee, Jade Webb, Olivia Wang, Joanna Fang, Cindy Liang, and Zadie Guo, for their help in conducting experiments.

I would like to thank my committee members, Dr. Narendra Dahotre, Dr. Moo-yeal Lee, Dr. Brian Meckes, and Dr. Huaxiao Yang, for their time and insightful comments.

I am thankful to Dr. Vijay Vaidyanathan, chair of the UNT biomedical engineering department, for his support. Thank Jaimie Tesdahl and Edward Gates for their help.

I would like to thank the collaborators, Dr. Narendra Dahotre and his lab members Yee-Hsien Ho and Sangram Mazumder, Dr. Brian Meckes and his student Afia Ibnat Kohon, Dr. Hamid Sadat, and his student Khang Phan, Dr. Feng Zhao, and her student Yeh-Chia Tseng from Texas A&M University, Dr. Michael Story from UT Southwestern.

I would like to thank Dr. Jinluo Wang, my advisor during my Master's study, for his continuous guidance and encouragement during my study and life.

I am grateful to my parents and brother for their love and support throughout my Ph.D. journey and life. Their unwavering support has made this journey possible. I am also grateful to my dear wife, Guiping Xiao, for her love and support. She makes my life better and teaches me more about family values.

TABLE OF CONTENTS

Page

LIST OF TABLES

Page

LIST OF FIGURES

Page

CHAPTER 1

INTRODUCTION

1.1 Physiologically Relevant *in vitro* Models

The investigation of human physiology, pathology, and disease treatment has mainly relied on animal models. Although animal models allow the investigation in a living system, they are costly, time-consuming and have ethical issues. Moreover, because of the difference in physiology and anatomy of organs in different species, the responses of animals to some treatments can differ from each other and from those of human, which may result in inconsistent data on new drug testing and new drug failure in clinical testing.[1] These highlight the urgent need for *in vitro* platforms as a replacement. Conventional *in vitro* models, in which the cells are cultured on plastic surfaces, have advanced our understanding of biology and pathology, but the cell behaviors significantly deviate from their *in vivo* counterparts. Cell behaviors are highly affected by the surrounding microenvironment, so it is crucial to understand the effects of the microenvironmental cues on cell behaviors and incorporate these cues when developing biomimetic *in vitro* models.

1.2 Microenvironmental Cues in Human Tissues and Organs

A cell is considered as the minimal, independently functioning unit of a living organism. Typically, a group of many similar cells or related cells work together to perform a specific function in human body, called a tissue. In a tissue, the cells are surrounded and supported by extracellular matrix (ECM). The ECM serves as a scaffold to stabilize the physical architecture of tissues and organs throughout the body. Still, it is also a complex network that plays an active and complex role in regulating cell behavior and

signaling (Figure 1.1).[2-4]

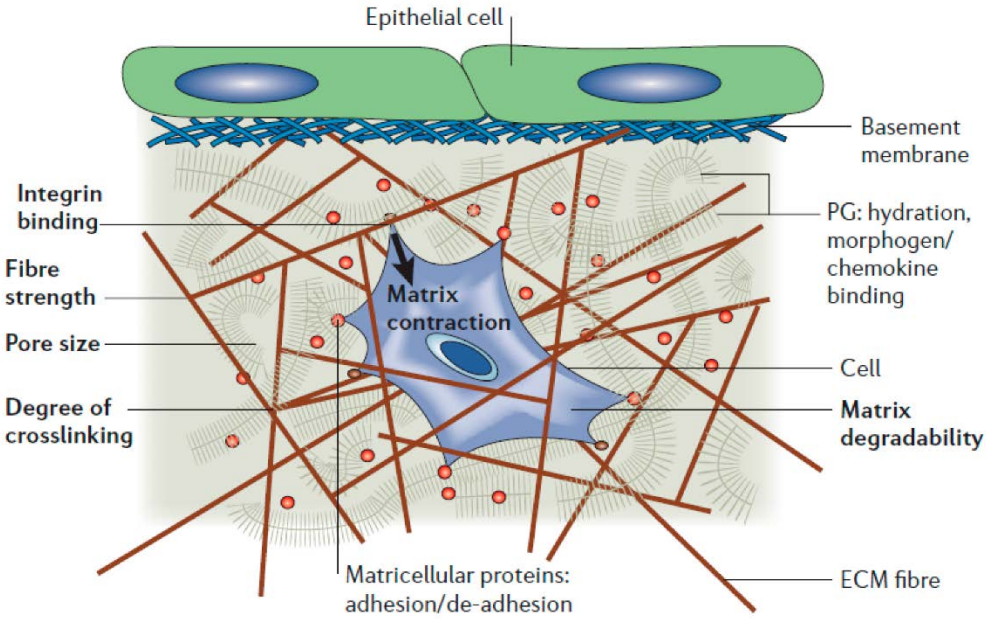

Figure 1.1: Schematic of the ECM microenvironment for cells *in vivo*.[4]

The ECM acts as a reservoir for both structural and functional constituents including polysaccharide, fibrous proteins (e.g., collagen, fibronectin, and elastin), molecular mediators (e.g., hormone and growth factors), ECM-modifying enzymes, and other matrix molecules. The cell-cell interactions and cell-ECM interactions contribute to the ECM content and organization. The ECM composition and properties are tissue-specific and highly dynamic and are heterogeneous among the different regions of a tissue, which is critical to tissue development and homeostasis. Classically, the regulation of cell behavior has been attributed principally to genetic and molecular mediators such as hormone and transcription factors.[5] For example, pancreatic beta cells release the hormone insulin into the blood in response to an increased level of blood glucose. The insulin stimulates adipocytes and liver cells to take up the excess glucose to decrease glucose concentration to normal range.[6, 7]

Besides biochemical cues, increasing evidence has demonstrated the critical influence of biophysical and mechanical mechanisms, i.e., the ECM structure and geometry at the micro- and nanoscale, ECM elasticity, and mechanical forces, on cell behavior, tissue and organ development, and homeostasis.[8] The variations in the composition and structure of the components among tissues and different regions of tissue affect the structure and biomechanical properties of the ECM network, as well as cell behavior and signaling.[9-11] For example, fibrillar collagens, including collagen types I, II, III, V, XI, XXIV, and XXVII, are abundantly expressed in tissue and form hierarchical structures. The length of the fibrils varies, and the diameter ranges from 10 nm to 500 nm, which depend on the stage of development and collagen type. The fibril formation is also affected by other biomolecules such as decorin and biglycan.[11, 12] Human lamina cribrosa (LC) is the main structural component of optic nerve head in human eyes, which is formed by stacks of collagenous cribriform plates with main composition of collagen types I, III, and IV and with high strength.[13, 14] The deformation and displacement of the LC have been increasingly implicated as the primary pathophysiologic mechanism of glaucomatous optic neuropathy.[15, 16] The ECM of the skin is composed of random-oriented collagen fibers (mainly types I and III), fibrin, elastin, and proteoglycans. Fiber structure defines the rigid mechanical property of skin, while elastic fibers enable stretching. Proteoglycans, including hyaluronan, decorin, create an osmotically active hydrated interstitial space.[17-19] The stiffness of tissues varies with ECM composition and structure, and the alterations are often associated with diseases.[20, 21] For example, the Young's modulus of normal lung ECM is 1-5kPa, while it can be increased to 20-100kPa and 20-30 kPa in lung fibrosis and lung cancer, respectively. The disease

progression results from the interaction between fibroblasts and the ECM: The elastin and type V collagen expression are increased in abnormal conditions, which induces the myofibroblast differentiation, and in return, myofibroblast differentiation promotes elastin and type V collagen and results in stiffer ECM.[22-24] The nanostructure and stiffness of tissues are shown in Figure 1.2.[21]

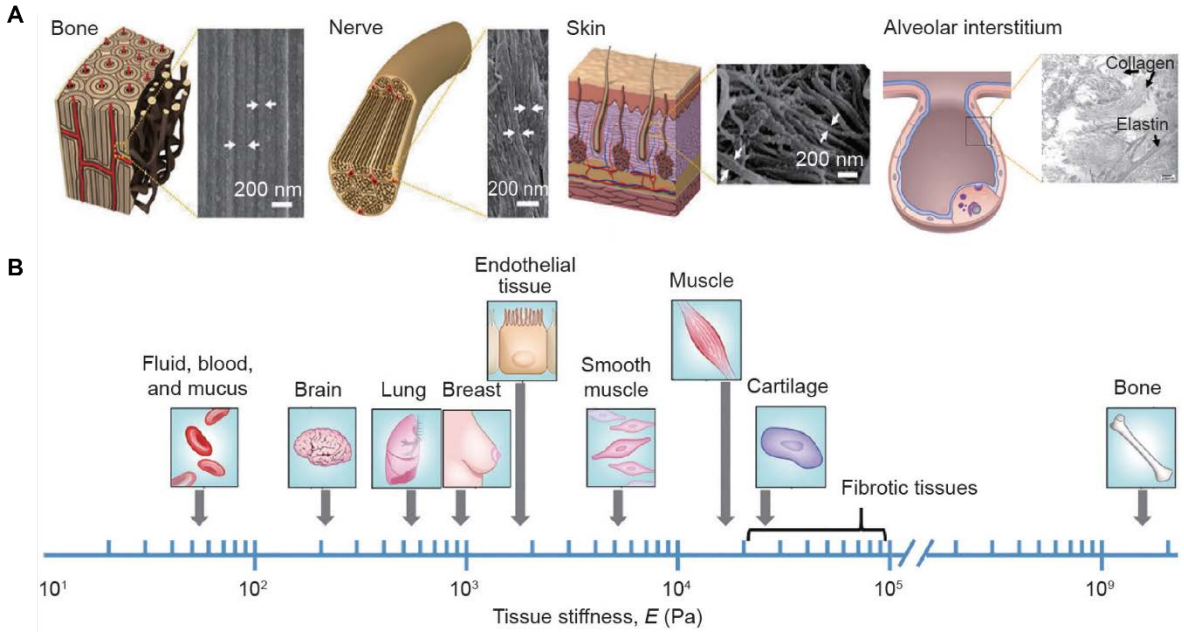

Figure 1.2: Biophysical properties of various human tissues. (A) The illustrations and scanning electron microscope (SEM) images show the structure of bone, nerve, skin, and alveolar interstitium. (B) The stiffness of human tissues.[21]

Tissues are subject to large-scale extrinsic mechanical forces. These mechanical forces are integral parts of the microenvironment that modulate the cellular phenotype and play essential roles in the development and homeostasis of tissues and organs. For example, the skin is a dynamic, self-renewing barrier subjected to various mechanical forces, including tensile stretch and compression from body movement and pushing forces from underlying tissues.[25, 26] The heart beats pump blood and, thus, supply cells, tissues and organs with oxygen and nutrients. At the cellular level within the heart, the mechanical forces convert to electrical and biochemical signals that alter the cardiac

function.[27] The deviation in the mechanical forces is often associated with organ dysfunction and many diseases.[28-30] For example, vascular endothelial cells and smooth muscle cells undergo cyclic strain stress from blood pressure and blood flow shear stress. Mechanical forces play important roles in cell proliferation, angiogenesis, vascular maintenance, and remodeling. However, excessive mechanical force during hypertension has been reported to perturb these processes and cause cardiovascular abnormalities.[28, 29] In this study, we focused on investigating the effects of nanotopography and mechanical stretch on cell behaviors and developing biomimetic *in vitro* models based on these findings.

1.3 Nanotopography Modulation of Cell Behavior

The micro- and nanoscale structures in tissues influence cell behaviors and functions *in vivo*.[31] However, traditional *in vitro* studies culture cells on two-dimensional (2-D) plastic surfaces, where cell behavior often differs from their *in vivo* counterparts. The development of micro- and nanotechnology has enabled the replication of complex topographical features in *in vitro* cell culture models. Substrates with different geometries have been produced for cell culture, as shown in Figure 1.3. The nanoposts, nanospheres, nanopits, and nanotubes are isotropic, while the nanogratings and aligned nanofibers are anisotropic. Randomly oriented nanofibers are also commonly used, as are less ordered or more complicated nanotopographies.[32, 33]

Photolithography and electron beam lithography are commonly used technologies in micro- and nanofabrication. The fabricated nanotopographies are often used as molds to replicate the structures using elastomeric stamps, typically polydimethylsiloxane (PDMS). Other techniques include micelle lithography, anodization polymer demixing,

chemical etching, and phase separation processes.[34, 35] 3D bioprinting now enables the fabrication of complex structures such as 3D structures with various nanotopographies using layer by layer printing and a variety of biomedical materials can be printed, from hard metals for bone implantation to soft hydrogels for mimicking soft tissues.[36, 37] Nanofibrous network is one of the distinct nanostructures in the ECM of tissues. Currently, several techniques, such as temperature-induced phase separation, drawing, melt spinning, and electrospinning, are used for nanofiber fabrication. Among which, electrospinning is most widely used due to its efficiency and simplicity. Moreover, a wide range of biomaterials can be used for electrospinning, and the fiber network properties are controllable, such as fiber diameter, orientation, density, and porosity.[38, 39]

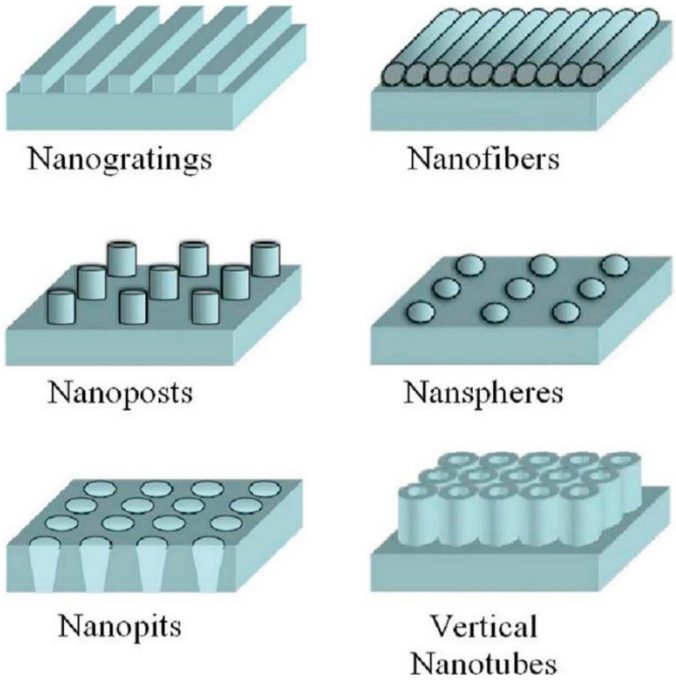

Figure 1.3: Schematic of representative nanotopographic geometries developed as cell culture substrates.[32]

Tissue functions depend heavily on cell characterization (e.g., shape and polarity), organization and communication. Nanotopography has been shown to modulate cell

behaviors through contact guidance, and the influence is now under extensive investigation, such as cell morphology, orientation, adhesion, migration, proliferation, and stem cell pluripotency and differentiation.[40, 41] For example, the neurons have many extensions, axons, and dendrites, responsible for communicating with target cells and receiving information from adjacent neurons for signal transmission. The neuronal cell polarization can be directed by micro- or nanogrooves, which allow isolation and biochemically analysis of axons *in vitro*.[42] Cells sense the ECM through adhesions, and adhesion formation plays a vital role in subsequent activities, such as cell growth, migration, and differentiation.[43] Nanotopograhies provide cell adhesion sites and guide focal adhesion formation, and both nanopattern structure and density can influence focal adhesion formation. Followed by cell adhesion, the cell migration can be directed through selective focal adhesion formation on nanopatterns.[33, 44] Cell proliferation can also be modulated by nanotopographies.[45, 46] Nanotube topography on TiO2 substrate has been reported to increase osteoblast growth by 300-400% compared to flat TiO2 surface, which is most likely caused by the providing increased surface area and promoting the filopodia formation.[46] Controlling substrate nanotopography is an effective approach for regulating stem cell expansion and differentiation.[47-49] For example, aligned poly(l-lactic acid) nanofiber has been reported to promote neural stem cell differentiation compared to flat surface or microscale fibers.[48]

1.4 Mechanical Stretch Modulation of Cell Behavior

Mechanical stretch is one of the mechanical forces experienced by various tissues and organs and is related to their physiology and pathology. Regarding mimicking the mechanical stretch *in vivo*, different *in vitro* models that are capable of subjecting cells to

one-dimensional (1D, uniaxial), two-dimensional (2D, biaxial, equibiaxial or circumferential) or three-dimensional (3D, radial) mechanical stretch have been developed.

A lung-on-a-chip platform with uniaxial mechanical stretch has been developed. The alveolar epithelial and capillary endothelial cells cultured on both sides of an elastic membrane align perpendicularly to the strain and form an intact alveolar-capillary interface. The mechanical strain enhances the uptake and transport of nanoparticles across the interface, which is similar to *in vivo* study.[50] This lung-on-a-chip design has also been used to model several lung diseases,[51, 52] human kidney glomerulus,[53] and human small intestine.[54]

Commercially available Flexcell^{TM} systems and similar systems can apply uniaxial, biaxial or equibiaxial strain to cells cultured on a flexible membrane *in vitro*. These systems have been widely used to simulate the mechanical stretch and thus to study related physiology and pathology in human body. For example, the study of cardiomyocyte hypertrophy,[55] vascular remodeling,[56] lung inflammatory response,[57] and lung fibrosis.[24, 58] The uniaxial strain has been reported to promote bone marrow mesenchymal stem cell (MSC) differentiation into vascular smooth muscle cells (SMCs) compared to equiaxial strain. While biaxial strain enhances the formation of mature elastic fibers and collagen matrix in engineered blood vassals, which increases the vascular compliance compared to uniaxial strain. To better mimic the mechanical strain experienced by SMCs in blood vessels, a novel device with circumferential 2D mechanical stretch has been developed. Compared to cells under static condition, the SMCs under this 2D mechanical strain orient perpendicularly to the strain direction with

a contractile phenotype similar to the *in vivo* state. A progeria model has been developed by increasing this circumferential 2D mechanical strain rate. The gene expression and inflammation marker expression under progeria condition are similar to *in vivo* study.[59-61]

The 3D radial cyclic mechanical stretch models have also been developed to simulate the lung periodic stretch, which is more like the *in vivo* lung movement.[62, 63] The exposure of alveolar epithelial cells to the circulatory environment indicated that cyclic mechanical stress affected the cell function: the permeability of the epithelial barrier was significantly increased, inducing higher metabolic activity. For the cells exposed to the 3D cyclic mechanical strain, a higher level of the inflammatory marker IL-8 is produced than in cells in static condition.[62]

High-throughput mechanical stretch platforms enable large-scale analysis *in vitro*. An integrated strain array (ISA) has been produced by integrating multiple PDMS cell culture wells with an acrylic pneumatic compartment with a pressure control system. Each well has a cylindrical pillar in the center supporting a PDMS membrane. Under vacuum, the membrane around the pillar is pulled down, causing the center region to be stretched biaxially. The spacing and volume of the wells match that of 96-well plates, allowing high-throughput analysis by using standard techniques.[64] By using aforementioned ISA, it has been shown that 15% mechanical strain induces canine kidney epithelial cell cycle entry, in which E-cadherin-mediated cell-cell adhesion is required.[65]

1.5 Outline of This Study

The development of *in vitro* cell culture model showed great promise in physiological and pathophysiological study. To mimic the structure and function of tissues

and organs *in vitro*, it is crucial to understand the importance of biophysical and mechanical characteristics in the ECM of tissues and reproduce and incorporate these characteristics in *in vitro* cell culture models. To understand the nanotopography modulation of cell behavior, we first investigated the cell behaviors on nanostructure with various aspect ratios on the surface of cobalt–chromium–molybdenum (CoCrMo) alloy. Then, the effect of nanofibrous membrane on alveolar epithelium formation was investigated, which is important for lung alveolar interstitium chip. We also investigated mechanical stretch modulation of cell behavior and focused on the stretch dimensionality effects on cell behavior. To develop an *in vitro* model based on these studies, we engineered a stem cell niche with a combination of nanofibrous membrane, mechanical stretch, and soft substrate, and explored the influence on stem cell behavior. Finally, we developed a biomimetic human lung interstitium chip for physiological and pathophysiological studies *in vitro*.

1.6 References

[1] R. Greek, A. Menache, Systematic reviews of animal models: methodology versus epistemology, Int J Med Sci 10(3) (2013) 206-21.

[2] J.G. Betts, K.A. Young, J.A. Wise, E. Johnson, B. Poe, D.H. Kruse, O. Korol, J.E. Johnson, M. Womble, P. DeSaix, Anatomy and physiology, 2013.

[3] C. Frantz, K.M. Stewart, V.M. Weaver, The extracellular matrix at a glance, Journal of cell science 123(24) (2010) 4195-4200.

[4] L.G. Griffith, M.A. Swartz, Capturing complex 3D tissue physiology in vitro, Nature reviews Molecular cell biology 7(3) (2006) 211-224.

[5] T.N. Wight, Versican: a versatile extracellular matrix proteoglycan in cell biology, Current opinion in cell biology 14(5) (2002) 617-623.

[6] B.N. Brown, S.F. Badylak, Extracellular matrix as an inductive scaffold for functional tissue reconstruction, Translational Research 163(4) (2014) 268-285.

[7] A. Sainio, H. Järveläinen, Extracellular matrix macromolecules as potential targets of cardiovascular pharmacotherapy, Advances in Pharmacology 81 (2018) 209-240.

[8] F. Guilak, D.M. Cohen, B.T. Estes, J.M. Gimble, W. Liedtke, C.S. Chen, Control of stem cell fate by physical interactions with the extracellular matrix, Cell stem cell 5(1) (2009) 17-26.

[9] K.E. Kadler, C. Baldock, J. Bella, R.P. Boot-Handford, Collagens at a glance, Journal of cell science 120(12) (2007) 1955-1958.

[10] F.H. Silver, J.W. Freeman, G.P. Seehra, Collagen self-assembly and the development of tendon mechanical properties, Journal of biomechanics 36(10) (2003) 1529-1553.

[11] S. Mwenifumbo, M.M. Stevens, ECM interactions with cells from the macro-to nanoscale, Biomedical nanostructures 1 (2007) 225-260.

[12] A. Corsi, T. Xu, X.D. Chen, A. Boyde, J. Liang, M. Mankani, B. Sommer, R.V. Iozzo, I. Eichstetter, P.G. Robey, Phenotypic effects of biglycan deficiency are linked to collagen fibril abnormalities, are synergized by decorin deficiency, and mimic Ehlers‐Danlos‐like changes in bone and other connective tissues, Journal of Bone and Mineral Research 17(7) (2002) 1180-1189.

[13] M. Rehnberg, T. Ammitzböll, B. Tengroth, Collagen distribution in the lamina cribrosa and the trabecular meshwork of the human eye, British journal of ophthalmology 71(12) (1987) 886-892.

[14] C. Braunsmann, C.M. Hammer, J. Rheinlaender, F.E. Kruse, T.E. Schäffer, U. Schlötzer-Schrehardt, Evaluation of lamina cribrosa and peripapillary sclera stiffness in pseudoexfoliation and normal eyes by atomic force microscopy, Investigative ophthalmology & visual science 53(6) (2012) 2960-2967.

[15] T.E. Ogden, J. Duggan, K. Danley, M. Wilcox, D.S. Minckler, Morphometry of nerve fiber bundle pores in the optic nerve head of the human, Experimental eye research 46(4) (1988) 559-568.

[16] G. Tezel, K. Trinkaus, M.B. Wax, Alterations in the morphology of lamina cribrosa pores in glaucomatous eyes, British journal of ophthalmology 88(2) (2004) 251-256.

[17] F.M. Watt, H. Fujiwara, Cell-extracellular matrix interactions in normal and diseased skin, Cold Spring Harbor Perspectives in Biology 3(4) (2011) a005124.

[18] M.T. Lam, A. Nauta, N.P. Meyer, J.C. Wu, M.T. Longaker, Effective delivery of stem cells using an extracellular matrix patch results in increased cell survival and proliferation and reduced scarring in skin wound healing, Tissue Engineering Part A 19(5-6) (2013) 738-747.

[19] L.E. Tracy, R.A. Minasian, E.J. Caterson, Extracellular matrix and dermal fibroblast function in the healing wound, Advances in wound care 5(3) (2016) 119-136.

[20] B.R. Seo, P. DelNero, C. Fischbach, In vitro models of tumor vessels and matrix: engineering approaches to investigate transport limitations and drug delivery in cancer, Advanced drug delivery reviews 69 (2014) 205-216.

[21] Y. Yang, K. Wang, X. Gu, K.W. Leong, Biophysical regulation of cell behavior—cross talk between substrate stiffness and nanotopography, Engineering 3(1) (2017) 36-54.

[22] A. Miyazawa, S. Ito, S. Asano, I. Tanaka, M. Sato, M. Kondo, Y. Hasegawa, Regulation of PD-L1 expression by matrix stiffness in lung cancer cells, Biochemical and biophysical research communications 495(3) (2018) 2344-2349.

[23] K. Wang, L. Shi, W. Linthicum, K. Man, X. He, Q. Wen, L.W. Rojanasakul, Y. Rojanasakul, Y. Yang, Substrate stiffness-dependent carbon nanotube-induced lung fibrogenesis, Nano letters 19(8) (2019) 5443-5451.

[24] M.E. Blaauboer, F.R. Boeijen, C.L. Emson, S.M. Turner, B. Zandieh-Doulabi, R. Hanemaaijer, T.H. Smit, R. Stoop, V. Everts, Extracellular matrix proteins: a positive feedback loop in lung fibrosis?, Matrix Biology 34 (2014) 170-178.

[25] O.T. Guenat, F. Berthiaume, Incorporating mechanical strain in organs-on-a-chip: Lung and skin, Biomicrofluidics 12(4) (2018) 042207.

[26] L.C. Biggs, C.S. Kim, Y.A. Miroshnikova, S.A. Wickström, Mechanical forces in the skin: roles in tissue architecture, stability, and function, Journal of Investigative Dermatology 140(2) (2020) 284-290.

[27] O. Friedrich, A.L. Merten, D. Schneidereit, Y. Guo, S. Schürmann, B. Martinac, Stretch in focus: 2D inplane cell stretch systems for studies of cardiac mechano-signaling, Frontiers in Bioengineering and Biotechnology 7 (2019) 55.

[28] N.F. Jufri, A. Mohamedali, A. Avolio, M.S. Baker, Mechanical stretch: physiological and pathological implications for human vascular endothelial cells, Vascular cell 7(1) (2015) 1-12.

[29] C. Li, Q. Xu, Mechanical stress-initiated signal transductions in vascular smooth muscle cells, Cellular signalling 12(7) (2000) 435-445.

[30] Y. Wang, J. Song, X. Liu, J. Liu, Q. Zhang, X. Yan, X. Yuan, D. Ren, Multiple effects of mechanical stretch on myogenic progenitor cells, Stem Cells and Development 29(6) (2020) 336-352.

[31] M.M. Stevens, J.H. George, Exploring and engineering the cell surface interface, Science 310(5751) (2005) 1135-1138.

[32] J. Shi, A.R. Votruba, O.C. Farokhzad, R. Langer, Nanotechnology in drug delivery and tissue engineering: from discovery to applications, Nano letters 10(9) (2010) 3223-3230.

[33] D.H. Kim, P.P. Provenzano, C.L. Smith, A. Levchenko, Matrix nanotopography as a regulator of cell function, Journal of Cell Biology 197(3) (2012) 351-360.

[34] J.J. Norman, T.A. Desai, Methods for fabrication of nanoscale topography for tissue engineering scaffolds, Annals of biomedical engineering 34(1) (2006) 89-101.

[35] A. Burklund, A. Tadimety, Y. Nie, N. Hao, J.X. Zhang, Advances in diagnostic microfluidics, Advances in clinical chemistry 95 (2020) 1-72.

[36] N. Shahrubudin, T.C. Lee, R. Ramlan, An overview on 3D printing technology: Technological, materials, and applications, Procedia Manufacturing 35 (2019) 1286-1296.

[37] Q. Yan, H. Dong, J. Su, J. Han, B. Song, Q. Wei, Y. Shi, A review of 3D printing technology for medical applications, Engineering 4(5) (2018) 729-742.

[38] S. Nemati, S.j. Kim, Y.M. Shin, H. Shin, Current progress in application of polymeric nanofibers to tissue engineering, Nano convergence 6(1) (2019) 1-16.

[39] D. Li, Y. Xia, Electrospinning of nanofibers: reinventing the wheel?, Advanced materials 16(14) (2004) 1151-1170.

[40] D.H. Kim, E.A. Lipke, P. Kim, R. Cheong, S. Thompson, M. Delannoy, K.-Y. Suh, L. Tung, A. Levchenko, Nanoscale cues regulate the structure and function of macroscopic cardiac tissue constructs, Proceedings of the National Academy of Sciences 107(2) (2010) 565-570.

[41] R.B. Dickinson, S. Guido, R.T. Tranquillo, Biased cell migration of fibroblasts exhibiting contact guidance in oriented collagen gels, Annals of biomedical engineering 22(4) (1994) 342-356.

[42] A.M. Taylor, M. Blurton-Jones, S.W. Rhee, D.H. Cribbs, C.W. Cotman, N.L. Jeon, A microfluidic culture platform for CNS axonal injury, regeneration and transport, Nature methods 2(8) (2005) 599-605.

[43] B.M. Gumbiner, Cell adhesion: the molecular basis of tissue architecture and morphogenesis, Cell 84(3) (1996) 345-357.

[44] N. Xia, C.K. Thodeti, T.P. Hunt, Q. Xu, M. Ho, G.M. Whitesides, R. Westervelt, D.E. Ingber, Directional control of cell motility through focal adhesion positioning and spatial control of Rac activation, The FASEB Journal 22(6) (2008) 1649-1659.

[45] C.J. Bettinger, Z. Zhang, S. Gerecht, J.T. Borenstein, R. Langer, Enhancement of in vitro capillary tube formation by substrate nanotopography, Advanced materials 20(1) (2008) 99-103.

[46] S. Oh, C. Daraio, L.H. Chen, T.R. Pisanic, R.R. Finones, S. Jin, Significantly accelerated osteoblast cell growth on aligned TiO2 nanotubes, Journal of Biomedical Materials Research Part A: An Official Journal of The Society for Biomaterials, The Japanese Society for Biomaterials, and The Australian Society for Biomaterials and the Korean Society for Biomaterials 78(1) (2006) 97-103.

[47] Y. Hou, W. Xie, L. Yu, L.C. Camacho, C. Nie, M. Zhang, R. Haag, Q. Wei, Surface roughness gradients reveal topography‐specific mechanosensitive responses in human mesenchymal stem cells, Small 16(10) (2020) 1905422.

[48] F. Yang, R. Murugan, S. Wang, S. Ramakrishna, Electrospinning of nano/micro scale poly (L-lactic acid) aligned fibers and their potential in neural tissue engineering, Biomaterials 26(15) (2005) 2603-2610.

[49] R.J. McMurray, N. Gadegaard, P.M. Tsimbouri, K.V. Burgess, L.E. McNamara, R. Tare, K. Murawski, E. Kingham, R.O.C. Oreffo, M.J. Dalby, Nanoscale surfaces for the long-term maintenance of mesenchymal stem cell phenotype and multipotency, Nature materials 10(8) (2011) 637-644.

[50] D. Huh, B.D. Matthews, A. Mammoto, M. Montoya-Zavala, H.Y. Hsin, D.E. Ingber, Reconstituting organ-level lung functions on a chip, Science 328(5986) (2010) 1662-1668.

[51] K.H. Benam, R. Villenave, C. Lucchesi, A. Varone, C. Hubeau, H.H. Lee, S.E. Alves, M. Salmon, T.C. Ferrante, J.C. Weaver, Small airway-on-a-chip enables analysis of human lung inflammation and drug responses in vitro, Nature methods 13(2) (2016) 151-157.

[52] D. Huh, D.C. Leslie, B.D. Matthews, J.P. Fraser, S. Jurek, G.A. Hamilton, K.S. Thorneloe, M.A. McAlexander, D.E. Ingber, A human disease model of drug toxicity–induced pulmonary edema in a lung-on-a-chip microdevice, Science translational medicine 4(159) (2012) 159ra147-159ra147.

[53] S. Musah, N. Dimitrakakis, D.M. Camacho, G.M. Church, D.E. Ingber, Directed differentiation of human induced pluripotent stem cells into mature kidney podocytes and establishment of a Glomerulus Chip, Nature protocols 13(7) (2018) 1662-1685.

[54] M. Kasendra, A. Tovaglieri, A. Sontheimer-Phelps, S. Jalili-Firoozinezhad, A. Bein, A. Chalkiadaki, W. Scholl, C. Zhang, H. Rickner, C.A. Richmond, Development of a primary human Small Intestine-on-a-Chip using biopsy-derived organoids, Scientific reports 8(1) (2018) 1-14.

[55] H.T. Facundo, R.E. Brainard, L.J. Watson, G.A. Ngoh, T. Hamid, S.D. Prabhu, S.P. Jones, O-GlcNAc signaling is essential for NFAT-mediated transcriptional reprogramming during cardiomyocyte hypertrophy, American Journal of Physiology-Heart and Circulatory Physiology 302(10) (2012) H2122-H2130.

[56] Y.X. Qi, Q.P. Yao, K. Huang, Q. Shi, P. Zhang, G.L. Wang, Y. Han, H. Bao, L. Wang, H.P. Li, Nuclear envelope proteins modulate proliferation of vascular smooth muscle cells during cyclic stretch application, Proceedings of the National Academy of Sciences 113(19) (2016) 5293-5298.

[57] J. Wu, Z. Yan, D.E. Schwartz, J. Yu, A.B. Malik, G. Hu, Activation of NLRP3 inflammasome in alveolar macrophages contributes to mechanical stretch-induced lung inflammation and injury, The Journal of Immunology 190(7) (2013) 3590-3599.

[58] M.E. Blaauboer, T.H. Smit, R. Hanemaaijer, R. Stoop, V. Everts, Cyclic mechanical stretch reduces myofibroblast differentiation of primary lung fibroblasts, Biochemical and biophysical research communications 404(1) (2011) 23-27.

[59] J.S. Park, J.S.F. Chu, C. Cheng, F. Chen, D. Chen, S. Li, Differential effects of equiaxial and uniaxial strain on mesenchymal stem cells, Biotechnology and bioengineering 88(3) (2004) 359-368.

[60] J. Ribas, Y.S. Zhang, P.R. Pitrez, J. Leijten, M. Miscuglio, J. Rouwkema, M.R. Dokmeci, X. Nissan, L. Ferreira, A. Khademhosseini, Biomechanical strain exacerbates inflammation on a progeria‐on‐a‐chip model, Small 13(15) (2017) 1603737.

[61] A.H. Huang, J.L. Balestrini, B.V. Udelsman, K.C. Zhou, L. Zhao, J. Ferruzzi, B.C. Starcher, M.J. Levene, J.D. Humphrey, L.E. Niklason, Biaxial stretch improves elastic fiber maturation, collagen arrangement, and mechanical properties in engineered arteries, Tissue Engineering Part C: Methods 22(6) (2016) 524-533.

[62] N.J. Douville, P. Zamankhan, Y.C. Tung, R. Li, B.L. Vaughan, C.F. Tai, J. White, P.J. Christensen, J.B. Grotberg, S. Takayama, Combination of fluid and solid mechanical stresses contribute to cell death and detachment in a microfluidic alveolar model, Lab on a Chip 11(4) (2011) 609-619.

[63] A.O. Stucki, J.D. Stucki, S.R.R. Hall, M. Felder, Y. Mermoud, R.A. Schmid, T. Geiser, O.T. Guenat, A lung-on-a-chip array with an integrated bio-inspired respiration mechanism, Lab on a Chip 15(5) (2015) 1302-1310.

[64] C.S. Simmons, J.Y. Sim, P. Baechtold, A. Gonzalez, C. Chung, N. Borghi, B.L. Pruitt, Integrated strain array for cellular mechanobiology studies, Journal of Micromechanics and Microengineering 21(5) (2011) 054016.

[65] B.W. Benham-Pyle, B.L. Pruitt, W.J. Nelson, Mechanical strain induces E-cadherin–dependent Yap1 and β-catenin activation to drive cell cycle entry, Science 348(6238) (2015) 1024-1027.

CHAPTER 2

NANOTOPOGRAPHICAL MODULATION OF CELL BEHAVIOR

2.1 Introduction

The ECM *in vivo* composed of different micro- and nanostructures, which play a key role on tissue and organ development and homeostasis. Many micro- and nanostructures have been developed to mimic the structure of ECM *in vitro* for biomedical applications.[1] To develop biomimetic *in vitro* cell culture models for physiological and pathophysiological study, we first investigated the effects of nanostructure with various aspect ratios (ARs) on the surface of cobalt–chromium–molybdenum (CoCrMo) alloy on cell behaviors, and then extended our study to nanofibrous membrane, which is more relevant to lung alveolar ECM structure, for the development of biomimetic lung alveolus chip.

In recent years, metallic materials such as titanium, stainless steel, and cobalt-chrome have been explored for their potential in biomedical applications, particularly bone tissue regeneration and orthopedic implants.[2] Among the materials, CoCrMo alloy has been widely used in orthopedic applications such as hip replacement due to its high corrosion resistance, wear resistance, strength, and hardness.[3-6] However, there are great concerns about the blood compatibility and anti-infection properties of metallic implants. Moreover, the capability to promote cell adhesion and new bone tissue formation is limited, which may cause implant failure or reduce the implant lifetime.[7, 8]

To improve the biocompatibility of implant materials, compositional and structural modification are commonly used methods.[7-10] The titanium oxide (TiO2) coating on CoCrMo is an example of promoting adhesion and spreading and osteogenic

differentiation marker hydroxyapatite nodule formation hMSCs.[7] Compared to chemical modification, the modification of surface structure provides a more stable and controllable way to promote their performance without inducing additional ion release or detrimental interactions with physiological fluids and has received more and more attention.[11, 12] In recent years, the influence of surface topography of implanted materials on their biocompatibility has been widely investigated, and the interactions of the alloy surface with various biomolecules *in vitro* are crucial for its long-term performance.[13, 14] For example, surface nanotube structure on TiO2 substrate has been reported to increase osteoblast growth by 300-400% compared to flat control and to promote filopodia formation.[14]

Despite the promising of surface structure modification for promoting implant performance, this method has rarely been reported in CoCrMo alloy. Previous studies reported that CoCrMo with well-defined microstructures could be obtained using selective laser melting or laser-directed energy deposition (L-DED) methods.[15-17] Our recent study showed that biocorrosion of the L-DED fabricated CoCrMo using potentiodynamic polarization (PDP) method can result in surface nanostructure with crest region at the Mo-enriched boundaries and a corresponding trough at the Co-rich regions. Moreover, the depth of the trough regions can be modified by adjusting the applied electrochemical potential values during PDP. Such surface nanostructure promoted pre-osteoblast MC3T3 cell adhesion and proliferation.

In this study, we first investigated if the surface nanostructures affect blood compatibility and antibacterial properties of the alloy, which are crucial for implants. Then, we investigated the effects of these nanostructures on pre-osteoblast MC3T3 cell and

human bone marrow mesenchymal stem cell (hMSC) behaviors in terms of cell adhesion, spreading, proliferation, and differentiation, for the understanding of nanotopography modulation of cell behaviors. Then, we extended our research to nanofibrous membranes, which are more relevant to *in vitro* ECM structure, and focused on the effect of the pore size on lung alveolar epithelium formation for the development of biomimetic lung alveolus chip.

2.2 Materials and Methods

2.2.1 Fabrication and Characterization of the Surface Structure of the Alloy

The L-DED was performed according to previous report using Ambit Mini Mill system equipped with Nd:YAG laser (1.06 μm wavelength).[15] Briefly, commercially available CoCrMo alloy powder was delivered to the focal plane of the laser beam (550 W laser power, 1 mm in diameter) through a hopper using Argon (Ar) as the carrier gas. The powder was melted at the focal plane and deposited onto the substrate at a 14.8 mm/s linear velocity. A 0.6mm overlap between consecutive laser tracks and 90° rotation after each layer was involved in the laser scanning pattern. The L-DED CoCrMo alloys were sectioned in the YZ plane, polished and subjected to PDP biocorrosion. The VSP 300 potentiostat/galvanostat (Bio-Logic, Seyssinet-Pariset, France) was used for performing PDP biocorrosion. Simulated body fluid (SBF) was used as the electrolyte, and the biocorrosion was conducted at 37 °C, with various potential differences for fabricating surface nanostructures of different depths.

Scanning electron microscopic (SEM) images of the L-DED CoCrMo alloys were taken using FEI Nova 230, and optical microscopic images were taken using Zeiss Axiolab 5 (Carl Zeiss Meditec, Jena, Germany). Energy Dispersive X-ray Spectrometry

(EDS) was performed using FEI ESEM Quanta to determine the elemental composition. Surface profilometry analysis of the L-DED CoCrMo alloys after biocorrosion was performed using a VK-X1000 surface profiler equipped with a laser microscope (Keyence, Osaka, Japan). The width of the crests (determined as the full width at half maximum) and depth of the throughs were measured from the surface profiles, and the AR of the surface nanostructures was calculated as the ratio of the average depth to the width.

Conventionally cast followed by homogenization heat-treated CoCrMo alloys were used as flat control, with a homogeneous elemental distribution. The samples were sterilized using an autoclave and rinsed with PBS before use.

2.2.2 Fabrication and Characterization of Nanofibrous Membranes

Nanofibrous membranes were fabricated by electrospinning a solution of polycaprolactone (PCL) in 1,1,1,3,3,3-hexafluoro-2-propanol (HFIP, 10%, w/v). Briefly, the PCL solution was loaded in a syringe with a blunt-tipped needle as the spinneret and connected to a syringe pump. A 4" x 4" square glass plate was placed on a 3" x 3" aluminum-covered plate as a collector, which was placed 16 cm below the needle tip. The needle tip was connected to a 14-kV voltage and the aluminum-covered plate was grounded. The PCL solution was ejected at a flow rate of 0.5 ml/hour and the nanofibers were deposited on the collector.

The formed nanofibrous membranes were sputter-coated with gold using Denton Vacuum Desk V sputter coater (Denton Vacuum, Moorestown, NJ, USA) and imaged using SEM (TM3030 Plus, Hitachi High-Technologies Co., Tokyo, Japan). The fiber diameter and membrane pore size were analyzed using ImageJ (http://rsb.info.nih.gov/ij/index.html). For the fiber diameter, a line was drawn across the

fiber, and then the length was measured. For the pore size, the images were adjusted using the threshold command and the area of each pore was analyzed using the “analyze particles” function. A histogram line graph was then generated to show the distribution of fiber diameters or pore sizes.

The fibrous membranes were sandwiched between two PDMS (Sylgard 184, Ellsworth Adhesives, Germantown, WA, USA) rings for cell culture via a µTA technique that we developed previously.[18] Briefly, a thin PDMS layer was spin-coated on a silicon wafer at 4000 rpm for 30 seconds and prebaked at 50 °C for 5 minutes. A PDMS ring was stamped on the PDMS layer and transferred onto the fibrous membrane, followed by curing at 45 °C for 2 hours. The PDMS ring and the fibrous membrane was gently peeled off from the collector and boned to another PDMS ring using the same method and cured at 45 °C overnight, with the fibrous membrane sandwiched between the two PDMS rings. For permeability test, the nanofibrous membrane was boned onto a transwell insert using the µTA technique. PCL films were used as flat control substrates and were fabricated by a spin-coating method. Briefly, 200 µL of 5% PCL (w/w) in HFIP solution was dropped onto a circular glass coverslip and then spun for 2 minutes at 4,000 rpm. The films were then air-dried in a chemical fume hood overnight to remove residual solvent.

2.2.3 Blood Compatibility

2.2.3.1 Platelet Adhesion

Each sample was fully covered with platelet rich plasma (PRP) (Zen-Bio, Research Triangle, NC, US) with a volume of 200 µl / cm^2 and incubated at 37 °C for 1 hour. The non-adherent platelets were then removed by rinsing the samples with PBS. Subsequently, the samples were fixed with 4% paraformaldehyde (PFA; Sigma-Aldrich,

St Louis, MO, USA) and 2% glutaraldehyde solution (Fisher Chemical, Fair Lawn, NJ, US) at room temperature for 2 hours and then dehydrated with gradient ethanol (30%, 50%, 70%, 80%, 90%, 95%, and 100%) and then hexamethyldisilazane (HMDS), 10 minutes for each step. The samples were stored in a desiccator and sputter-coated with gold using Denton Vacuum Desk V sputter coater before SEM observation. The adhered platelets were observed using FEI Quanta 200 ESEM and counted from SEM images.

2.2.3.2 Hemolysis Test

Healthy human blood containing 3.8% sodium citrate (Zen-Bio, US) was diluted with 0.9% sodium chloride solution (4:5, v/v). Each sample was dipped into a 15ml centrifuge tube containing 9.8 ml of 0.9% sodium chloride solution and incubated at 37 °C for 30 minutes. Subsequently, 200 µl of diluted blood was added to each tube and incubated at 37 °C for 1 hour. Meanwhile, diluted blood was added to 9.8 ml of deionized water as positive control and added to 0.9% sodium chloride solution as negative control. After centrifuging the tubes at 3,000 rpm for 5 minutes, the supernatants were collected and the absorbance (A) was measured at the wavelength of 545 nm using a Cytation 5 Cell Imaging Multi-Mode Reader (BioTek, Winooski, VT, USA). The hemolysis ratio (HR) was calculated by the following equation:

$$HR\ (\%) = (A_{sample} - A_{negative})/(A_{positive} - A_{negative}) \times 100\%$$

2.2.4 Antibacterial Properties

Escherichia coli (*E. coli,* ATCC 25922, US) were cultured in Tryptic Soy Broth (TSB; BD, Franklin Lakes, NJ, US) at 37 °C and 200 rpm to a concentration of approximately 10^8 colony forming units (CFU)/ml, and then were diluted 10-fold using TSB to a concentration of 10^4 CFU/ml. The samples were placed in petri dishes separately, and

the bacterial suspension was dipped onto the samples at 0.2 ml/cm^2. Meanwhile, the bacterial suspension was dipped onto Tryptic Soy Agar (TBA; BD) spread in a petri dish as negative control. All the dishes were placed in wet chambers and incubated at 37 °C for 24 hours. After incubation, the bacteria were collected by washing the samples with PBS (2 ml/cm^2) and diluted 1000-fold. Then, 10 µl of the solution was inoculated onto TBA plates and incubated at 37 °C for 18 hours, and the bacteria colonies were counted. The antibacterial activity (R) was calculated by the following formula:

$$R = (N_{negative} - N_{sample})/(N_{negative}) \times 100\%.$$

where $N_{negative}$ and N_{sample} were the colony number on the negative control and alloy samples, respectively.

2.2.5 Cell Culture

The murine calvarial pre-osteoblasts (MC3T3-E1, ATCC CRL-2593, Manassas, VA, US) were cultured in α-minimum essential medium (α-MEM, Gibco, Grand Island, NY, USA) supplemented with 10% fetal bovine serum (FBS; Sigma-Aldrich, USA), 100 U/ml penicillin and 100 µg/ml streptomycin (Life Technologies, Carlsbad, CA, USA). The hMSCs (Lonza, Bend, OR, USA) were cultured in mesenchymal stem cells growth medium (MSCGM, Lonza). The cells were seeded on the CoCrMo samples at a density of 10,000 cells/cm^2 (unless otherwise specified) and cultured at 37°C and 5% CO_2.

Human alveolar epithelial cells (A549; ATCC CCL-185, USA) were cultured in Dulbecco's Modified Eagle Medium (DMEM) with 10% FBS, 100 U/ml penicillin, and 100 µg/ml streptomycin (Life Technologies, US). The nanofibrous membranes or PCL films were oxygen plasma treated at the medium power setting for 1 minute in a plasma cleaner (Model PDC-001, Harrick Plasma, Ithaca, NY, USA) and then coated with 50 µg/ml type

I collagen (rat tail; Corning, Corning, NY, USA) overnight in the incubator. Cells were seeded at a density of 2 x 10^5 cells/cm^2 and cultured in the incubator of 37 °C and 5% CO_2.

2.2.6 MTT Assay

The cell viability was evaluated using MTT assay (Thermo Fisher Scientific, Waltham, MA, US). Briefly, after 5-day culture, the samples were transferred to 96-well plate. Then, 100 µL of fresh culture medium and 10 µL of 12 mM MTT stock solution were added to each well followed by incubation for 4 hours at 37°C. 10 µL of the MTT stock solution was added to 100 µL of fresh medium as negative control. After incubation, the medium was removed and 50 µL of DMSO was added to each well and mixed thoroughly with pipette. After incubation at 37°C for 10 minutes, the medium in each well was mixed again and transferred to a new well. The absorbance at 540 nm was measured using Cytation 5 Cell Imaging Multi-Mode Reader. The value of absorbance was normalized to that for the high AR samples.

2.2.7 Immunofluorescence Staining

After cell culture, the samples were rinsed gently with PBS and fixed with 4% PFA (Sigma-Aldrich, US) solution for 20 minutes at room temperature. Subsequently, the samples were rinsed 3 times with PBS and blocked for 1 hour at room temperature using PBST solution (PBS supplemented with 0.2% Triton X-100) containing 0.03 g/mL bovine serum albumin (BSA; Sigma-Aldrich, US) and 0.1% goat serum (v/v, Sigma-Aldrich, US). The samples were then incubated with Alexa Fluor 488 phalloidin (1:200, Life Technologies, US) and/or primary antibodies at 4°C overnight. The information regarding antibodies used for immunostaining and western blotting were listed in Table 2.1. After

rinsed 3 times with PBS, the samples were then incubated with secondary antibodies at room temperature for 1 hour. Subsequently, the nuclei were stained with SlowFade™ Gold Antifade Mountant with 4,6-diamidino-2-phenylindole (DAPI) (Life Technologies) and the images were taken using Zeiss LSM710 Confocal Microscope (Carl Zeiss, Germany) or Nikon Ti eclipse fluorescence microscope (Nikon, Melville, NY, USA). The fluorescent intensity, size, and number of paxillin per cell were analyzed using ImageJ.

Table 2.1: Antibodies for immunofluorescence staining and western blotting

Antibody	Vendor	Catalog #	Dilution
Paxillin	Abcam	ab32084	1:200 (IF)
ZO-1	Life Technologies	339100	1:100 (IF) 1:500 (WB)
ZO-3	Life Technologies	364000	1:200 (WB)
E-cadherin	Life Technologies	131700	1:1000 (WB)
Occludin	Life Technologies	331594	1:1000 (WB)
β-actin	Life Technologies	AM4302	1:1000 (WB)

2.2.8 Cell Morphology SEM Observations

After cultured for 5 days, the samples were prepared using the same method as described in 2.2.3.1 for SEM observation, and images were taken using FEI Quanta 200 ESEM.

2.2.9 Spinning Disc Assay

The MC3TC cells were seeded at a density of 5,000 cells/cm^2 and cultured for 1 day. Then, the samples were mounted in a petri dish exposed to three different shear stresses produced by spinning at 500 rpm, 1000 rpm, and 1500 rpm in PBS at room temperature for 2 minutes. The shear stresses were calculated using the following equation.

$$\tau = 0.8r(\rho\mu\omega^3)^{1/2}$$

where, τ is shear stress, r is radial position (0.04m), ρ (997kg/m^3) and μ (10^{-3} kg/m s) are the density and dynamic viscosity of PBS, ω is the angular speed.[19]

Before and after spinning, cell images were obtained using Nikon Ti eclipse microscope and the number of adherent cells were counted from at least four fields with a total of 70-250 cells for each sample.

2.2.10 Osteogenic Differentiation

After cultured for 21 days, the cells were fixed with 4% PFA for 1 hour and then stained with fast 5-bromo-4-chloro-3-indolyl phosphate and nitroblue tetrazolium (BCIP/NBT; VWR international, Radnor, USA) for 20 minutes at room temperature and then rinse with deionized water until the background was clear for alkaline phosphatase (ALP) staining. Images were taken using a Keyence BZ-X810 fluorescence microscope (Keyence, Osaka, Japan). The ALP activity was determined via colorimetry using ALP assay kit (Abcam, Waltham, MA, USA) according to the manufacturer's protocol. Briefly, the cells were harvested and lysed using ALP assay buffer. Then, the cell lysate was incubated with p-nitrophenyl phosphate (*p*NPP) for 1 hour, and the absorbance was measured at 405 nm. The protein concentration was measured using a standard bicinchoninic acid (BCA) Protein Assay Kit (Thermo Fisher Scientific), and ALP activity was normalized to protein quantity.

2.2.11 Western Blotting

The total proteins were extracted by lysing the cells with radioimmune precipitation assay (RIPA) buffer (Santa Cruz Biotechnology, Santa Cruz, CA, USA) that contained protease inhibitor for 30 minutes on ice followed by centrifuging at 4 °C, 12,000 rpm for 5

minutes and collecting the supernatant. Proteins were separated by 8% sodium dodecyl sulfate-polyacrylamide gel electrophoresis (SDS-PAGE) and transferred onto polyvinylidene fluoride (PVDF) membrane (Thermo Fisher Scientific). The membranes were blocked in 5% nonfat milk (RPI International, Mount Prospect, IL, USA) dissolved in Tris-buffered saline (TBS) with 0.1% Tween-20 (Thermo Fisher Scientific) at room temperature for 1 hour. Subsequently, the membrane was incubated with primary antibody and horseradish peroxidase (HRP) – conjugated secondary antibody. Protein bands were visualized by ECL detection kit (EMD Millipore, Burlington, MA, USA) and images were acquired using the ChemiDoc MP image system (Bio-Rad, Hercules, CA, USA). The band intensity was quantified using ImageJ and normalized to the expression of β-actin.

2.2.12 Permeability Assay

The epithelial permeability was measured in the 12-well transwell plate-based models including the epithelial cell monoculture on the nanofibrous membrane. 500 µl of 4 kDa (100 µg/ml) fluorescein isothiocyanate (FITC)-dextran (Sigma-Aldrich) was added to the insert and 1 ml of cell culture medium was added to the low compartment. The fluorescence intensity of the medium from the insert and the low compartment was measured after incubation for 2 hours.

The concentration of FITC-dextran was determined by fluorescence intensity that was compared to a calibration curve of FITC-dextran concentration vs fluorescence intensity. The apparent permeability P_{app} was calculated as $P_{app} = \frac{C_b V_b}{tA\Delta C}$, where C_b and V_b are the dextran concentration and solution volume in the low compartment of the transwell, t is the diffusion time, A is the total area of diffusion, ΔC is the concentration

change across the barrier.[20] The permeability coefficient of the epithelial barrier, P_{epi}, was determined from the P_{app} and the background permeability coefficient P_0 (measured in a transwell plate without epithelium) as follows: $\frac{1}{P_{epi}} = \frac{1}{P_{app}} - \frac{1}{P_o}$ (s/cm).

2.2.13 Statistical Analysis

All the data were reported as mean ± standard errors. The statistical significances were analyzed based on two-tailed t test by using Prism 8 (GraphPad software, San Diego, CA, US), with the significance level defined as $p < 0.05$.

2.3 Results and Discussion

2.3.1 Fabrication and Characterization of the Surface Structure of the Alloy

Well-defined microstructures were generated during the L-DED process, as shown in Figure 2.1A. To determine the elemental composition, an SEM EDS line scan was performed through adjacent grains, and the analysis revealed a selective concentration of Mo at the boundaries of the grains (Figure 2.1B). The optical microscopy image (Figure 2.1C) of the CoCrMo after PDP biocorrosion showed a clear differential etching of the Mo-rich gain boundaries and Co-rich cores, indicating the selective etching during the biocorrosion. The surface nanostructures of the etching were quantified using surface profilometry. The results indicated the presence of Mo-rich crests and Co-rich troughs. The width of the crests was calculated to be 0.510±0.097 μm, and the depth of the troughs increased with the applied potential difference. The AR of the surface nanostructures at 1.1 V, 1.7 V, and 2.1 V was shown in Figure 2.1D and was defined as low AR, Med AR, and High AR, respectively.

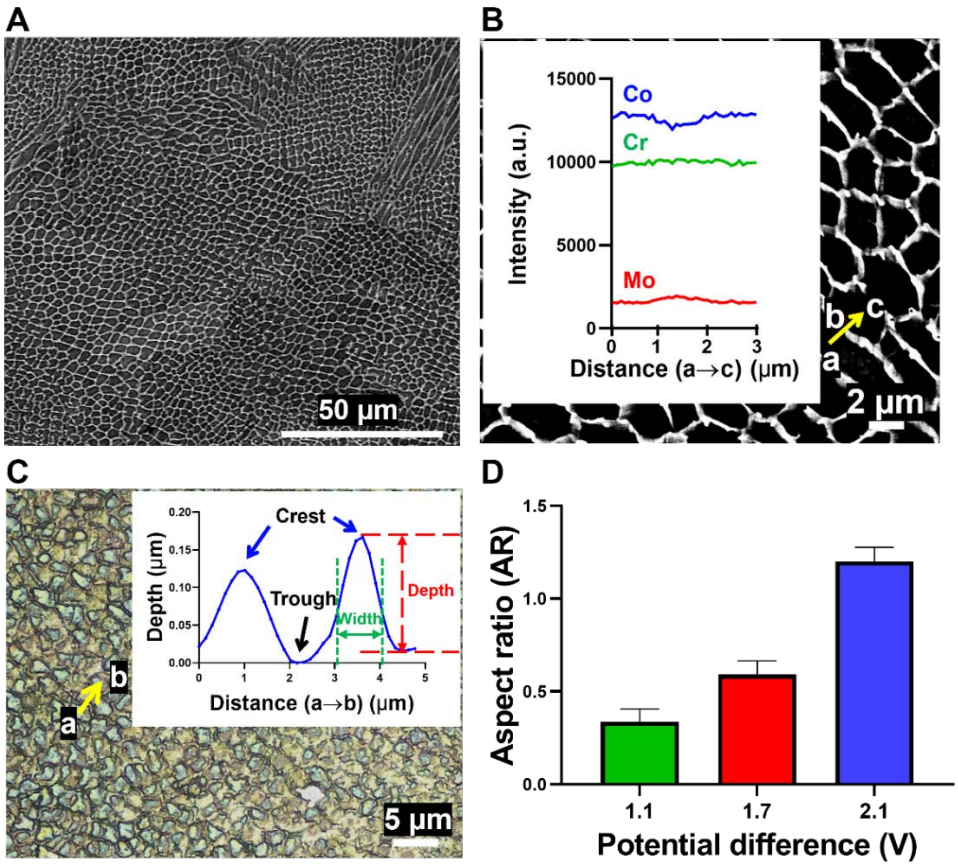

Figure 2.1: Characterization of the CoCrMo alloys. (A) Representative SEM image of the microstructure of the L-DED fabricated CoCrMo alloys. (B) Elemental composition analysis from SEM EDS line scan along two adjacent grains of the L-DED fabricated CoCrMo alloys. (C) Representative optical microscopic image and laser surface profilometry analysis (insert) of the L-DED CoCrMo after PDP biocorrosion. (D) AR of the surface nanostructures.

2.3.2 Fabrication and Characterization of Nanofibrous Membranes

Nanofibrous membranes of various pore sizes were generated by electrospinning PCL solution. By controlling the electrospinning time, nanofibrous membranes of three different pore sizes were fabricated, *i.e.*, small pores (S, 2.32 ± 1.52 µm^2), medium pores (M, 8.75 ± 5.79 µm^2), and large pores (L, 15.63 ± 9.79 µm^2) (Figure 2.2). Because all other processing parameters were kept unchanged, the fiber diameters of all these membranes were almost the same, *i.e.*, 890 ± 230 nm, 880 ± 240 nm, and 880 ± 210 nm for the small, medium, and large pore size membranes, respectively. Therefore, these

membranes allowed us to investigate the effects of the pore size on the epithelium formation.

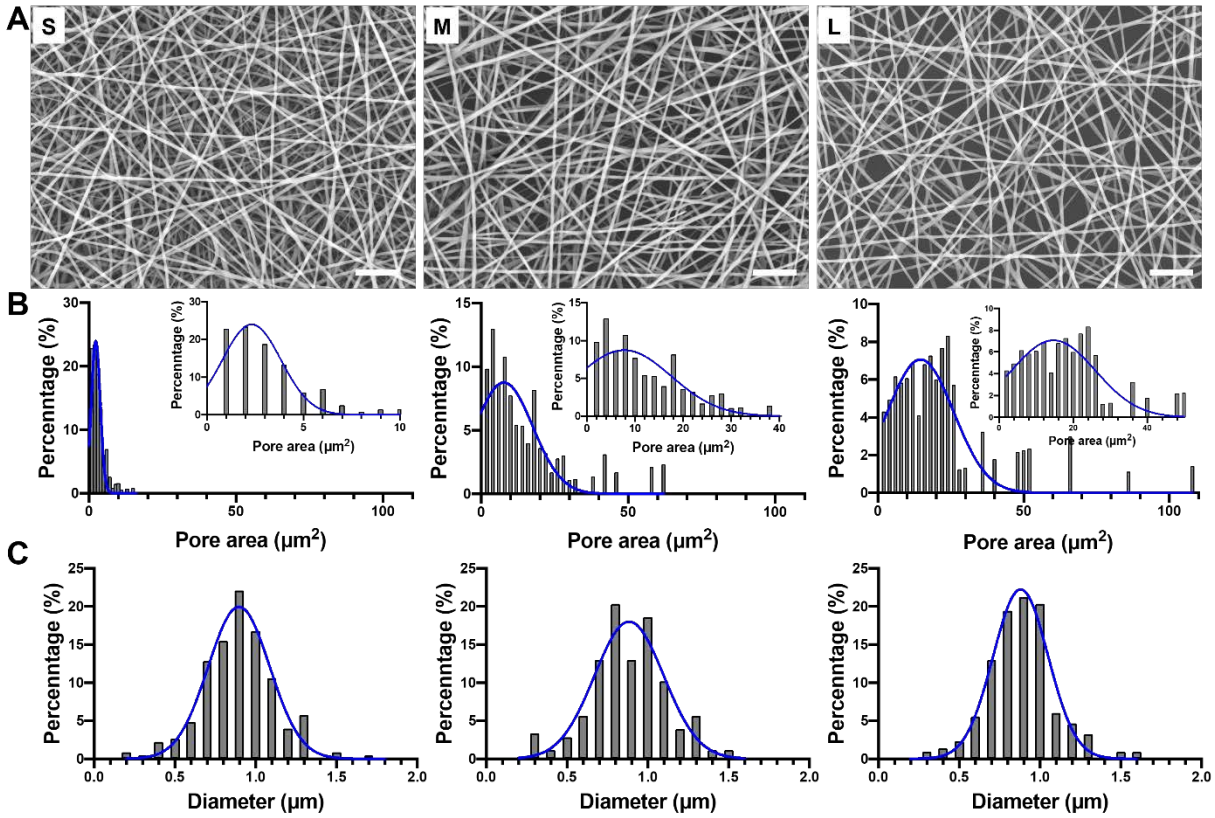

Figure 2.2: Characterization of the nanofibrous membranes. (A) SEM images of nanofibrous membranes of various pores. Scale bars: 20 μm. (B) Pore size distributions of these nanofibrous membranes. The insets magnify the distributions. (C) Fiber diameter distributions of these nanofibrous membranes.

2.3.3 Blood Compatibility

The blood compatibility of flat control and nanostructured surface with different AR were investigated via the platelet adhesion and hemolysis tests. Platelet adhesion, spreading and aggregation are considered to be a major mechanism of thrombosis, which needs to be minimized for biomedical materials. Figure 2.3A and 2.3B showed the morphology and number of adhered platelets on the sample surfaces. Platelet spreading and aggregation were observed on the flat control sample surface. In contrast, the

platelets showed round-shaped morphology and no aggregation were observed on nanostructured surface. The number of adhered platelets on medium and high AR samples significantly decreased compared to flat sample. Hemolysis was also utilized to evaluate blood compatibility, which is defined as the damage of erythrocytes with the release of hemoglobin into the plasma. The hemolysis ratios of all the samples were less than 5% (Figure 2.3C), which comes within permissible limit for blood-contacting biomaterials according to ASTM F 756 - 08. These results demonstrated that the blood compatibility of the CoCrMo alloy was enhanced by the medium and high AR nanostructure.

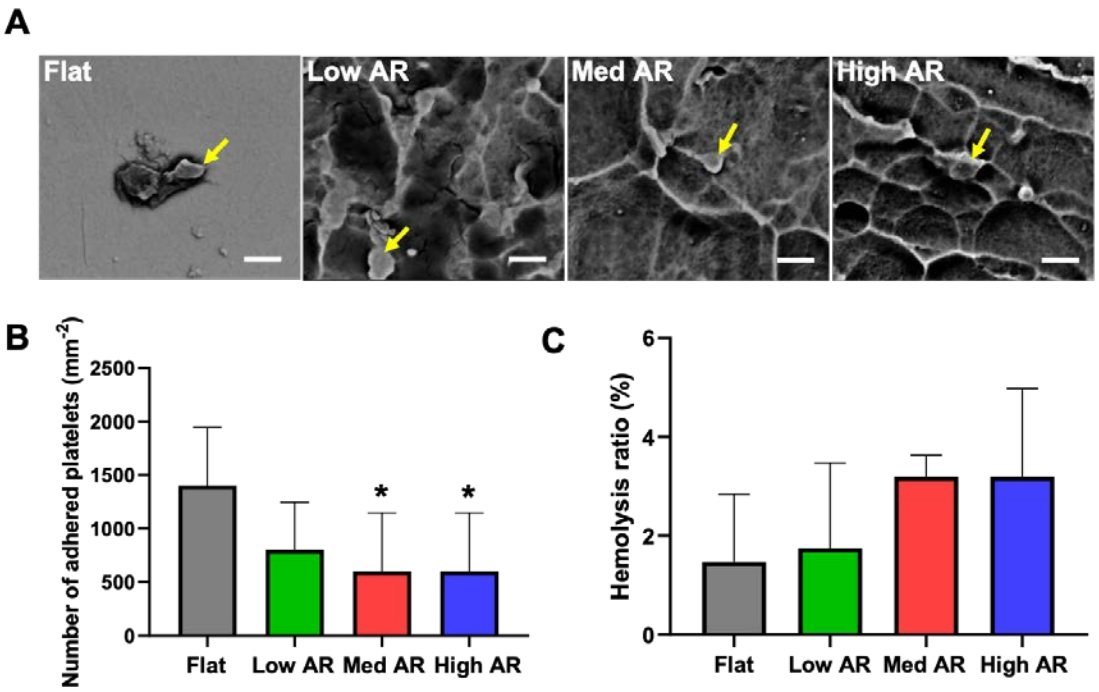

Figure 2.3: Blood compatibility of flat control and nanostructured samples. (A) SEM images of adherent platelets on the samples. The yellow arrowheads indicated platelets. Scale bars: 10 μm. (B) The corresponding number of adhered platelets. (C) Hemolysis ratio of different samples. *p < 0.05 compared to flat control sample. (n=3).

2.3.4 Antibacterial Properties

E. coli suspension was incubated on the surface of the alloy samples or TSA

(negative sample) for 24 hours followed by collected and transferred to TSA plates and incubated for 18 hours. Figure 2.4A showed the representative *E. coli* colonies on the TSA plates. More colonies were observed on the negative plate than all the alloy samples. The antibacterial activities of the alloy samples were also calculated and shown in Figure 2.4B. The antibacterial activities of the flat and all nanostructured CoCrMo alloys were more than 90%, indicating that the alloys had strong antibacterial activity. Bacterial infection has become the second leading cause of implantation failure according to clinical statistics.[21, 22] The antibacterial properties of alloys depend on their physical and chemical properties, such as composition, packing, density, configuration and surface topographies. Although reports shown that surface topographies affect bacterial adhesion, colonization and biofilm formation, conflicting data were found, and it is still far from conclusive.[20, 23] In the present study, the CoCrMo alloys with nanostructured surface maintained the antibacterial properties of the CoCrMo alloy, with the potential application for implantation.

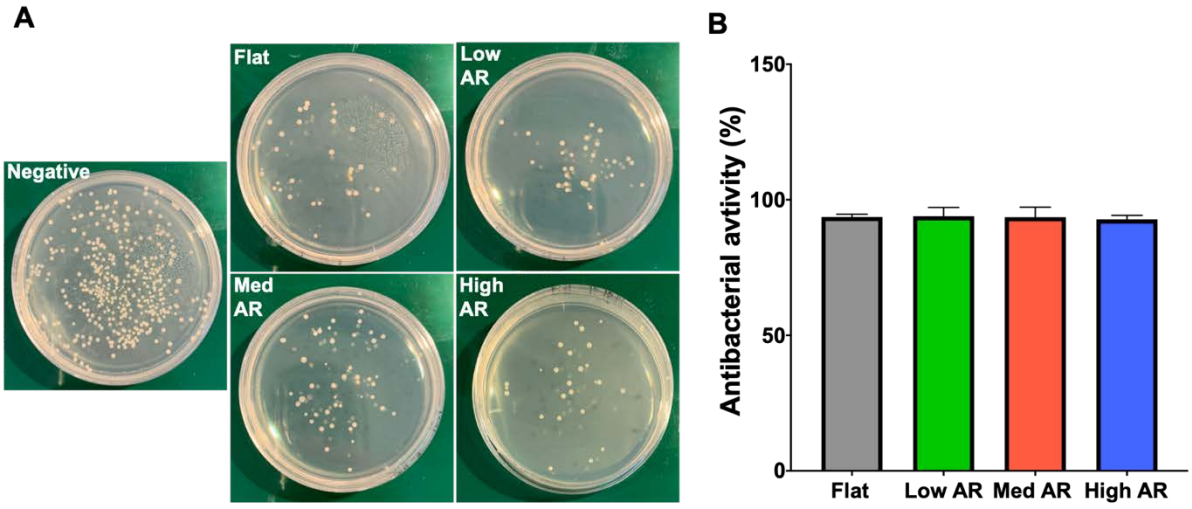

Figure 2.4: Antibacterial properties of the samples. (A) Typical photos of colonization by *E. coli* on negative sample and alloy samples. (B) Antibacterial activity of the alloy samples. (n=3).

2.3.5 Cell Viability

Cytocompatibility is critical to implant biomaterials, and thus the viability of cells cultured on the alloys was evaluated using MTT assay. The MTT results shown that the medium and high AR surface nanostructure promoted MC3T3 cell viability compared to flat control. And cells cultured on high AR surface nanostructure showed significantly higher cell viability than these on low and medium AR nanostructure surface (Figure 2.5). These observations indicated that cell growth was promoted by the nanostructure with medium and high AR on the CoCrMo alloy surface.

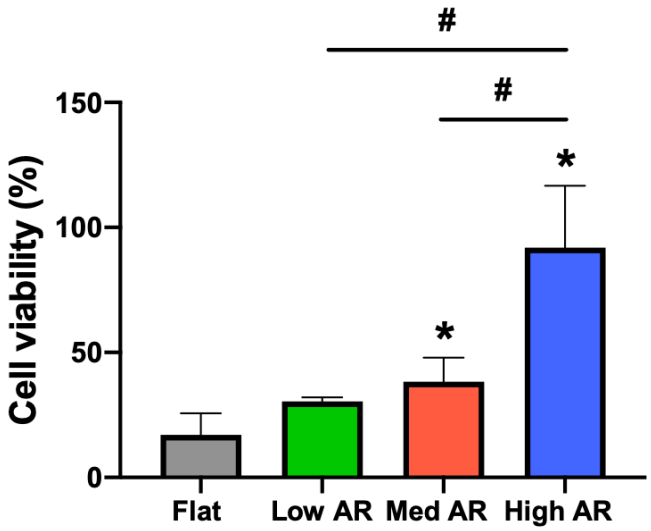

Figure 2.5: The viability of pre-osteoblasts on the samples after cultured for 5 days. Cell viability data were normalized to the mean value of the data of the high AR groups. (n=3). *: $p < 0.05$ compared to flat control surface. #: $p < 0.05$ between groups.

2.3.6 Cell Adhesion and Spreading

To understand how the nanostructures on the surface promoted cell growth, we examined the interactions between cells and the substrates. The immunofluorescence staining images shown that the MC3T3 cells on medium and high AR nanostructures displayed more mature focal adhesion protein paxillin (Figure 2.6A). The number of

paxillin per cell and the size of paxillin were further analyzed using ImageJ. The results showed that both the number and size of paxillin were increased on the medium and high AR nanostructures compared to those on flat surface (Figure 2.6B, C). The adhesive strength of MC3T3 cells on the alloy surface was also examined using a physical method, spinning disc assay, which was modified from ASTM F2664 – 11 and previous reports.[19, 24] (Described in 2.2.9). To alleviate the influence of cell−cell interactions, the cells were seeded at a low density (5000 cells/cm^2) and cultured for 1 day. The number of adherent cells on the flat surface decreased significantly after shear force was applied and deceased as the shear force increased. In contrast, the majority of cells remained attached on the nanostructured surfaces as the shear stress was applied and increased (Figure 2.6D).

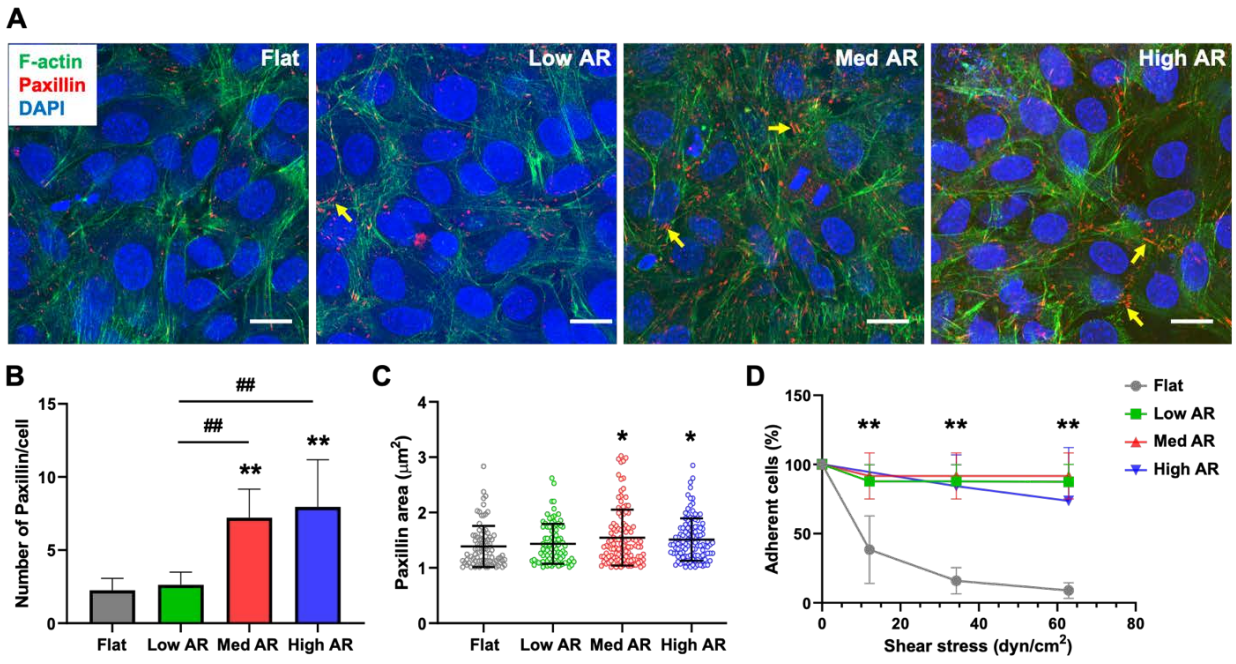

Figure 2.6: The adhesion and spreading of pre-osteoblasts on the samples. (A) Representative immunofluorescence images of the cells. The yellow arrows indicated mature paxillin. Scale bars: 20 μm. (B) Paxillin number per cell and (C) paxillin size analyzed form the images in (A). (D) Percentage of adherent cells as a function of applied shear stress. *: $p < 0.05$, **: $p < 0.01$ compared to flat surface. $^{\#}$: $p < 0.05$, $^{\#\#}$: $p < 0.01$ between groups.

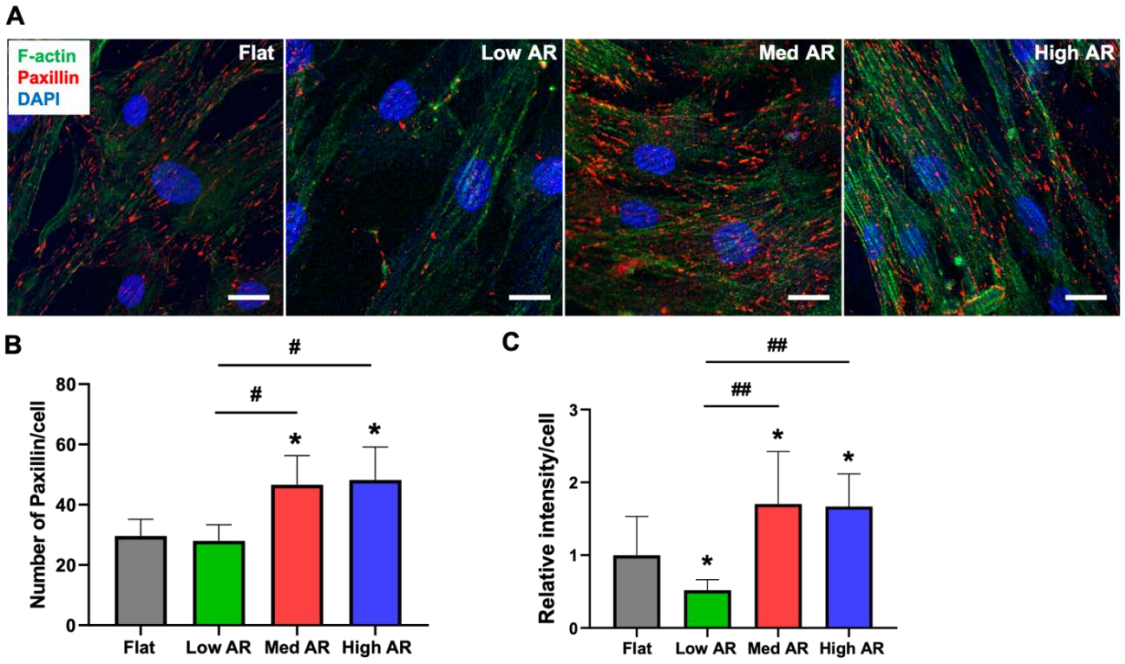

Figure 2.7: The adhesion and spreading of hMSCs on the samples. (A) Representative immunofluorescence images of the cells. Scale bars: 10 μm. (B) Paxillin number per cell and (C) F-actin intensity analyzed form the images in (A). *: $p < 0.05$ compared to flat surface. $^{\#}$: $p < 0.05$, $^{\#\#}$: $p < 0.01$ between groups.

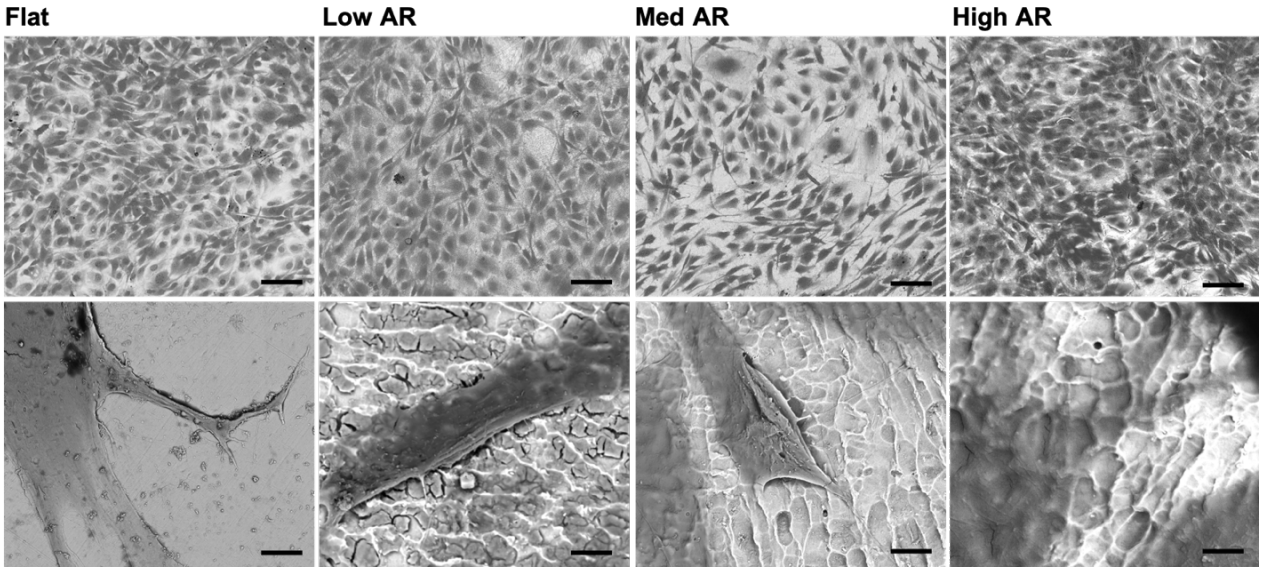

Figure 2.8: Low (first row) and high (second row) magnification SEM images of hMSCs on the samples. Scale bars: 100 μm and 5 μm.

The paxillin and F-actin expressions of hMSCs on the samples were also examined using immunofluorescence staining. The cells on the nanostructured surface

with medium and high AR displayed more mature paxillin and actin fibers, as shown in Figure 2.7. These results indicated that cell adhesion and spreading were promoted by the medium and high nanostructures on the alloy surface. The cell morphology and cell-substrate interaction of hMSCs were also inspected via SEM imaging (Figure 2.8). The cells showed spreading morphology on all the samples and the majority of cells exhibited bending membranes on the nanostructure surfaces.

The initial contact of cells on implanted material surfaces determines cell behaviors and is critical to cell growth and implant success. Previous studies shown that cells interact with surfaces at the micro or nanometer scale. Cells sense surface texture through adhesion receptors and induce focal adhesion formation and nanopatterns can help generate robust anchorage of cells, which have great potential for bone regeneration.[25-27] In this study, nanostructures with various ARs were fabricated on the surface of the 3D printed CoCrMo alloys. The cells cultured on the medium and high AR nanostructures formed more and mature focal adhesion and exhibited higher cell viability, which indicated that these nanostructures promoted cell adhesion and cell growth through focal adhesion-mediated cell anchoring. The cell membrane was bent towards the troughs of the nanostructures, particularly on the medium and large ratio nanostructures. This membrane deformation provides larger cell-substrate contact area and result in promoted cell adhesion and spreading, which is consistent with previous report that nano-micropatterns can control cell-substrate interactions and may benefit tissue integration after implantation.[28]

2.3.7 Osteogenic Differentiation

Osteogenic differentiation is a crucial aspect in the success of bone implantation.

This process involves the transformation of both pre-osteoblasts and stem cells into mature bone cells, known as osteoblasts, which are responsible for the formation of new bone tissue.[29, 30] Thus, we investigated the impact of the surface nanostructures with various AR on osteogenic differentiation of both MC3T3 cells and hMSCs. The expression of osteogenic differentiation marker ALP was analyzed using BCIP/NBT staining and quantified using ALP activity assay. The results showed that the nanostructures promoted osteogenic differentiation of both pre-osteoblasts MC3T3 cells and hMSCs. Moreover, the ALP expression was increased on the surfaces of the medium and high AR nanostructures compared to the surface of low AR nanostructure (Figure 2.9).

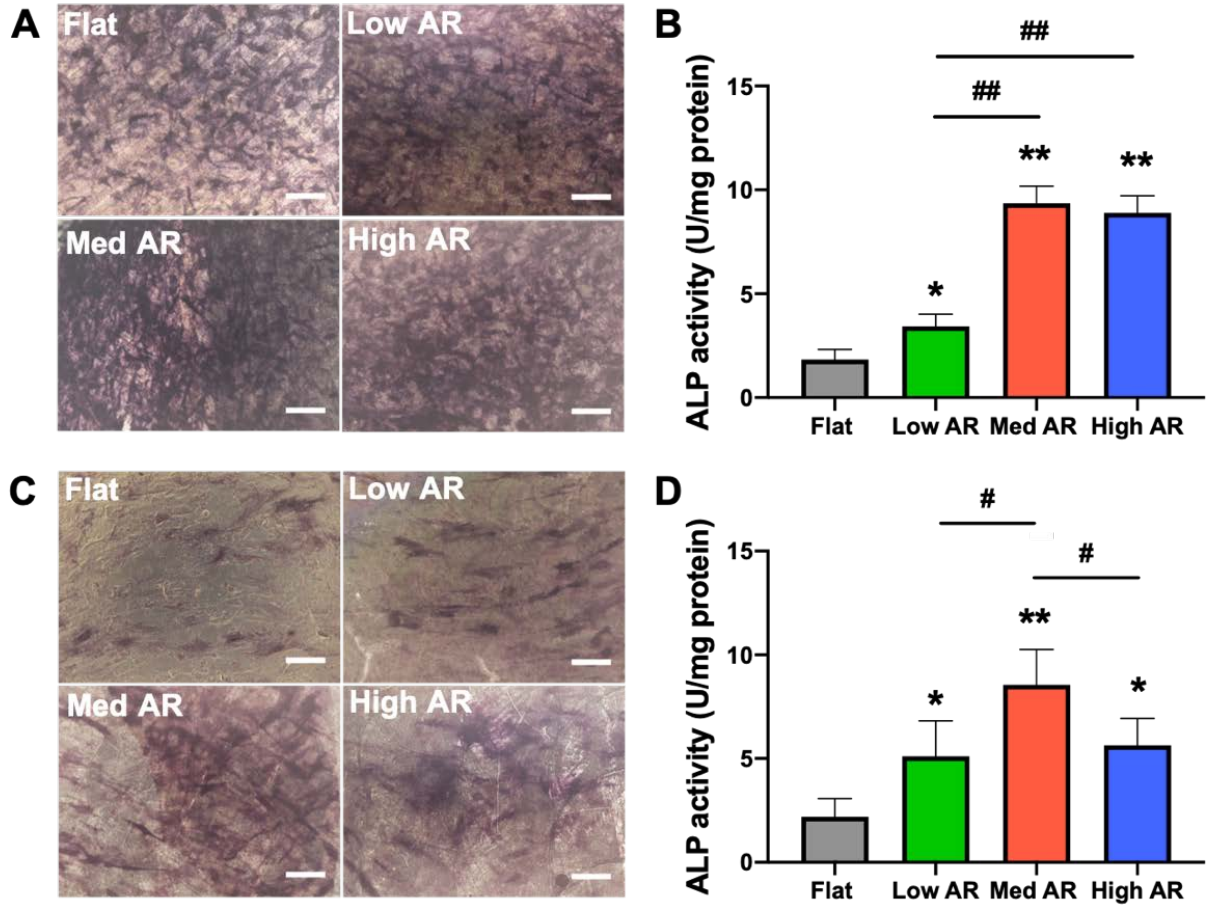

Figure 2.9: (A, C) ALP staining and (B, D) ALP activity of (A, B) pre-osteoblasts MC3T3 and (C, D) hMSCs cultured on the CoCrMo alloys. Scale bars: 200 µm. *: $p < 0.05$, **: $p < 0.01$ compared to flat surface. $^{\#}$: $p < 0.05$, $^{\#\#}$: $p < 0.01$ between groups.

Implant materials can act as scaffolds to promote osteogenic differentiation by providing a physical and chemical environment. Compared to chemical triggers, nanotopographical cues provide the benefits of a more stable, precisely controlled, and safer interface, and mechanical signals can be transmitted quicker than diffusion-based chemical signals.[31, 32] Studies have shown that nanoscale surface structures can affect the behaviors, including osteogenic differentiation of pre-osteoblasts and stem cells.[14, 33-35] The mechanisms may involve interactions of the cells with the nanotopography through focal adhesion, increase in intracellular tension, mechanotransduction pathways through cytoskeleton to nucleus, and possibly chromosome alteration.[34, 36, 37] Our study indicated that the medium and high AR nanostructures on the surface of CoCrMo alloys promoted osteogenic differentiation of both pre-osteoblasts MC3T3 cells and hMSCs, which may be attributed to the increased focal adhesion, actin fibers, and corresponding alteration of mechannotransduction.

2.3.8 Lung Alveolar Epithelium Formation

Human alveolar epithelial A549 cells were grown on these nanofibrous membranes and PCL flat surface as the control. After 10 days, the epithelial cells displayed continuous tight junction protein zonula occludens (ZO)-1 on the nanofibrous membranes compared to discrete ZO-1 expression on the flat control (Figure 2.10A). The pore size effects on the expression of tight junction proteins ZO-1, ZO-3, and occludin and adhesions junction protein E-cadherin were evaluated using western blot. In general, nanofibrous membranes upregulated the protein expression and the cells showed significantly higher expressions of ZO-1 and occludin on the medium and large pore membranes than the flat control (Figure 2.10B).

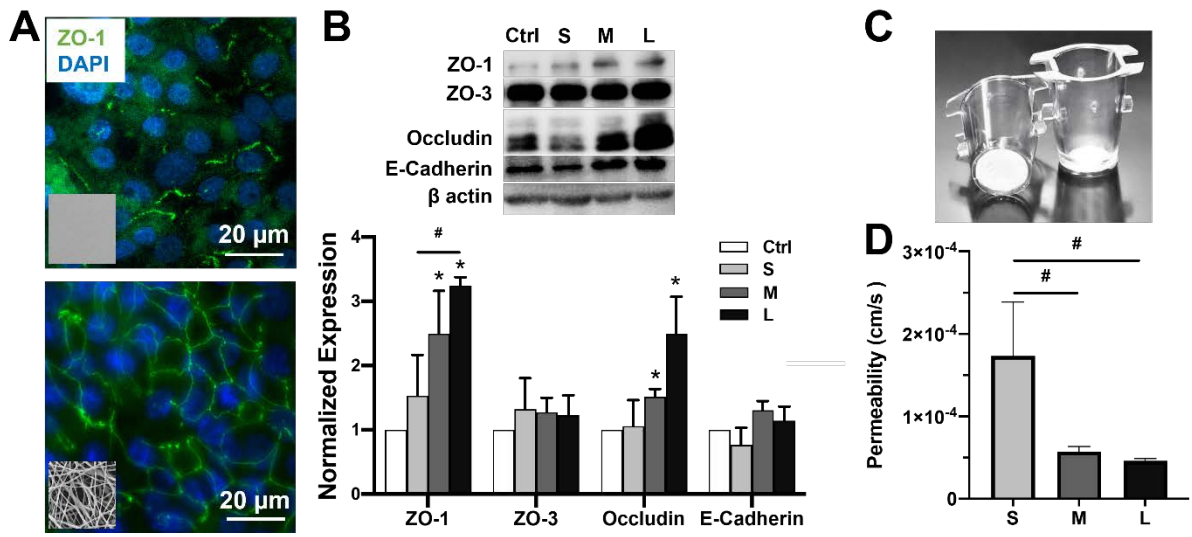

Figure 2.10: Lung alveolar epithelium formation on the nanofibrous membranes and PCL flat control substrate. (A) Representative immunofluorescence images of A549 cells cultured on PCL flat control and nanofibrous membranes (SEM images are presented in the insets) for 10 days. Green: ZO-1; blue: nuclei. (B) Western blotting of ZO-1, ZO-3, occludin, and E-cadherin of A549 cells cultured on the flat control and nanofibrous membranes with small (S), medium (M), and large (L) pore sizes (n = 3). The data were normalized to the mean value of the flat control. (C) Photos of transwell inserts attached with the nanofibrous membrane. (D) Permeability of 4kDa dextran across the epithelial cell layer on the nanofibrous membranes. *: $p < 0.05$ compared to the flat control. $^{\#}$: $p < 0.05$ between groups.

Moreover, the nanofibrous membranes were attached to the transwell insert and the permeability coefficient of dextran-commonly used to assess transport via the paracellular route through tight junctions-across the epithelial monolayers was assessed.[38] Similarly, the epithelium permeability on the nanofibrous membranes of medium and large sizes were significantly lower than that on the small pore membrane (Figure 2.10D).

The basement membrane of lung alveolar epithelium exhibits oval-shaped pores of 0.75 to 3.85 μm in size and the microporous membrane facilitates type II pneumocytes to form a monolayer, facilitates heterocellular crosstalk, and acts as a route for immune cells to move between the epithelium and interstitium.[39-41] PCL fibrous membrane has been shown to promote the barrier function of lung alveolar epithelium.[42] However, it

was unclear if the pore size of fibrous membranes influenced alveolar epithelium barrier function. In this study, PCL nanofibrous membranes with various pore sizes were fabricated and their promoting effects on the epithelium formation and their permeability were verified. Occludin is linked via zonula occludens protein complexes to tight junctions that seal neighboring epithelial cells and limit paracellular diffusion. The upregulated expression of occludin and ZO-1 proteins and decreased epithelial permeability on the medium and large pore membranes suggested that both nanofibrous membranes promoted the formation of tight alveolar epithelium. Although the large pore membrane showed a better promoting effect on tight epithelium, leakage occurred occasionally due to some large pores. Thus, the nanofibrous membrane of medium pores ($8.75 \pm 5.79\ \mu m^2$) was selected for the fabrication of lung alveolus chip.

2.4 Conclusion

Surface modification of implant materials is a common technique to improve cytocompatibility, blood compatibility, and minimize the risk of infection. We have fabricated surface nanostructures with various aspect ratios on CoCrMo alloys and investigated the effects of blood compatibility, antibacterial properties, and cytocompatibility. The results suggest that a medium and high AR nanostructure was favorable for promoting cell adhesion, spreading, proliferation, and osteogenic differentiation. The improved cytocompatibility and blood compatibility, as well as good antibacterial properties, made the nanostructured CoCrMo alloy a promising candidate for orthopedic implants. The PCL nanofibrous membrane with medium and large pore promoted the formation of tight alveolar epithelium, highlighted the importance of the *in vitro*- like ECM structure for the development of biomimetic lung alveolus chip.

2.5 References

[1] T. Xiang, J. Hou, H. Xie, X. Liu, T. Gong, S. Zhou, Biomimetic micro/nano structures for biomedical applications, Nano Today 35 (2020) 100980.

[2] S.A. Yavari, S.M. Ahmadi, R. Wauthle, B. Pouran, J. Schrooten, H. Weinans, A.A. Zadpoor, Relationship between unit cell type and porosity and the fatigue behavior of selective laser melted meta-biomaterials, Journal of the mechanical behavior of biomedical materials 43 (2015) 91-100.

[3] B.D. Ratner, A.S. Hoffman, F.J. Schoen, J.E. Lemons, Biomaterials science: an introduction to materials in medicine, San Diego, California (2004) 162-4.

[4] I. Milošev, CoCrMo alloy for biomedical applications, Biomedical Applications, Springer2012, pp. 1-72.

[5] C.V. Vidal, A.I. Muñoz, Effect of thermal treatment and applied potential on the electrochemical behaviour of CoCrMo biomedical alloy, Electrochimica Acta 54(6) (2009) 1798-1809.

[6] A.I. Muñoz, L.C. Julián, Influence of electrochemical potential on the tribocorrosion behaviour of high carbon CoCrMo biomedical alloy in simulated body fluids by electrochemical impedance spectroscopy, Electrochimica Acta 55(19) (2010) 5428-5439.

[7] N. Logan, A. Sherif, A.J. Cross, S.N. Collins, A. Traynor, L. Bozec, I.P. Parkin, P. Brett, TiO2-coated CoCrMo: Improving the osteogenic differentiation and adhesion of mesenchymal stem cells in vitro, Journal of Biomedical Materials Research Part A 103(3) (2015) 1208-1217.

[8] A. Batal, R. Sammons, S. Dimov, Response of Saos-2 osteoblast-like cells to laser surface texturing, sandblasting and hydroxyapatite coating on CoCrMo alloy surfaces, Materials Science and Engineering: C 98 (2019) 1005-1013.

[9] F.A. España, V.K. Balla, S. Bose, A. Bandyopadhyay, Design and fabrication of CoCrMo alloy based novel structures for load bearing implants using laser engineered net shaping, Materials Science and Engineering: C 30(1) (2010) 50-57.

[10] Y.H. Ho, K. Man, S.S. Joshi, M.V. Pantawane, T.C. Wu, Y. Yang, N.B. Dahotre, In-vitro biomineralization and biocompatibility of friction stir additively manufactured AZ31B magnesium alloy-hydroxyapatite composites, Bioactive materials 5(4) (2020) 891-901.

[11] I. Fenoglio, B. Fubini, E.M. Ghibaudi, F. Turci, Multiple aspects of the interaction of biomacromolecules with inorganic surfaces, Advanced drug delivery reviews 63(13) (2011) 1186-1209.

[12] L. Nimb, K. Gotfredsen, J. Steen Jensen, Mechanical failure of hydroxyapatite-coated titanium and cobalt-chromium-molybdenum alloy implants. An animal study, Acta orthopaedica belgica 59 (1993) 333-333.

[13] M.J. Dalby, N. Gadegaard, R. Tare, A. Andar, M.O. Riehle, P. Herzyk, C.D. Wilkinson, R.O. Oreffo, The control of human mesenchymal cell differentiation using nanoscale symmetry and disorder, Nature materials 6(12) (2007) 997-1003.

[14] S. Oh, C. Daraio, L.H. Chen, T.R. Pisanic, R.R. Finones, S. Jin, Significantly accelerated osteoblast cell growth on aligned TiO2 nanotubes, Journal of Biomedical Materials Research Part A: An Official Journal of The Society for Biomaterials, The Japanese Society for Biomaterials, and The Australian Society for Biomaterials and the Korean Society for Biomaterials 78(1) (2006) 97-103.

[15] S. Mazumder, M.V. Pantawane, S.M. Patil, M. Radhakrishnan, S. Sharma, M. McKinstry, N.B. Dahotre, Thermokinetically Driven Microstructural Evolution in Laser-Based Directed Energy-Deposited CoCrMo Biomedical Alloy, Advanced Engineering Materials 24(11) (2022) 2200352.

[16] G. Janaki Ram, C. Esplin, B. Stucker, Microstructure and wear properties of LENS® deposited medical grade CoCrMo, Journal of Materials Science: Materials in Medicine 19 (2008) 2105-2111.

[17] S. Acharya, V. Gopal, S.K. Gupta, S. Nilawar, G. Manivasagam, S. Suwas, K. Chatterjee, Anisotropy of Additively Manufactured Co–28Cr–6Mo Influences Mechanical Properties and Biomedical Performance, ACS Applied Materials & Interfaces 14(19) (2022) 21906-21915.

[18] Y. Yang, K. Kulangara, J. Sia, L. Wang, K.W. Leong, Engineering of a microfluidic cell culture platform embedded with nanoscale features, Lab on a Chip 11(9) (2011) 1638-1646.

[19] A.J. García, P. Ducheyne, D. Boettiger, Quantification of cell adhesion using a spinning disc device and application to surface-reactive materials, Biomaterials 18(16) (1997) 1091-1098.

[20] W. Teughels, N. Van Assche, I. Sliepen, M. Quirynen, Effect of material characteristics and/or surface topography on biofilm development, Clinical oral implants research 17(S2) (2006) 68-81.

[21] M.R. Rasouli, C. Restrepo, M.G. Maltenfort, J.J. Purtill, J. Parvizi, Risk factors for surgical site infection following total joint arthroplasty, JBJS 96(18) (2014) e158.

[22] D.E. Reichman, J.A. Greenberg, Reducing surgical site infections: a review, Reviews in Obstetrics and Gynecology 2(4) (2009) 212.

[23] G. Mi, D. Shi, M. Wang, T.J. Webster, Reducing bacterial infections and biofilm formation using nanoparticles and nanostructured antibacterial surfaces, Advanced Healthcare Materials 7(13) (2018) 1800103.

[24] N.D. Gallant, K.E. Michael, A.J. García, Cell adhesion strengthening: contributions of adhesive area, integrin binding, and focal adhesion assembly, Molecular biology of the cell 16(9) (2005) 4329-4340.

[25] S. Lavenus, J.-C. Ricquier, G. Louarn, P. Layrolle, Cell interaction with nanopatterned surface of implants, Nanomedicine 5(6) (2010) 937-947.

[26] S.B. Goodman, J. Gallo, Periprosthetic osteolysis: mechanisms, prevention and treatment, Journal of Clinical Medicine 8(12) (2019) 2091.

[27] A.I.M. Greer, V. Goriainov, J. Kanczler, C.R.M. Black, L.-A. Turner, R.M.D. Meek, K. Burgess, I. MacLaren, M.J. Dalby, R.O.C. Oreffo, Nanopatterned titanium implants accelerate bone formation in vivo, ACS applied materials & interfaces 12(30) (2020) 33541-33549.

[28] M. Ermis, E. Antmen, V. Hasirci, Micro and Nanofabrication methods to control cell-substrate interactions and cell behavior: A review from the tissue engineering perspective, Bioactive materials 3(3) (2018) 355-369.

[29] L.L. Dunlop, B.K. Hall, Relationships between cellular condensation, preosteoblast formation and epithelial-mesenchymal interactions in initiation of osteogenesis, International Journal of Developmental Biology 39(2) (2002) 357-371.

[30] J. Chen, F. Long, mTORC1 signaling promotes osteoblast differentiation from preosteoblasts, PloS one 10(6) (2015) e0130627.

[31] N. Wang, J.D. Tytell, D.E. Ingber, Mechanotransduction at a distance: mechanically coupling the extracellular matrix with the nucleus, Nature reviews Molecular cell biology 10(1) (2009) 75-82.

[32] D.S. Widyaratih, P.L. Hagedoorn, L.G. Otten, M. Ganjian, N. Tümer, I. Apachitei, C.W. Hagen, L.E. Fratila-Apachitei, A.A. Zadpoor, Towards osteogenic and bactericidal nanopatterns?, Nanotechnology 30(20) (2019) 20LT01.

[33] Y. Yang, K. Wang, X. Gu, K.W. Leong, Biophysical regulation of cell behavior—cross talk between substrate stiffness and nanotopography, Engineering 3(1) (2017) 36-54.

[34] S. Dobbenga, L.E. Fratila-Apachitei, A.A. Zadpoor, Nanopattern-induced osteogenic differentiation of stem cells–A systematic review, Acta biomaterialia 46 (2016) 3-14.

[35] Y. Zhang, H. Gong, Y. Sun, Y. Huang, Y. Fan, Enhanced osteogenic differentiation of MC3T3-E1 cells on grid-topographic surface and evidence for involvement of YAP mediator, Journal of Biomedical Materials Research Part A 104(5) (2016) 1143-1152

[36] H. Nikukar, S. Reid, P.M. Tsimbouri, M.O. Riehle, A.S.G. Curtis, M.J. Dalby, Osteogenesis of mesenchymal stem cells by nanoscale mechanotransduction, ACS nano 7(3) (2013) 2758-2767.

[37] J. Yang, L.E. McNamara, N. Gadegaard, E.V. Alakpa, K.V. Burgess, R.M.D. Meek, M.J. Dalby, Nanotopographical induction of osteogenesis through adhesion, bone morphogenic protein cosignaling, and regulation of microRNAs, ACS nano 8(10) (2014) 9941-9953.

[38] T.S. Frost, L. Jiang, R.M. Lynch, Y. Zohar, Permeability of Epithelial/Endothelial Barriers in Transwells and Microfluidic Bilayer Devices, Micromachines 10(8) (2019) 533.

[39] Z. Liu, H. Wu, K. Jiang, Y. Wang, W. Zhang, Q. Chu, J. Li, H. Huang, T. Cai, H. Ji, MAPK-mediated YAP activation controls mechanical-tension-induced pulmonary alveolar regeneration, Cell reports 16(7) (2016) 1810-1819.

[40] J.S. Lwebuga-Mukasa, G. Thulin, J.A. Madri, C. Barrett, J.B. Warshaw, An acellular human amnionic membrane model for in vitro culture of type II pneumocytes: the role of the basement membrane in cell morphology and function, Journal of Cellular Physiology 121(1) (1984) 215-225.

[41] X. Yang, K. Li, X. Zhang, C. Liu, B. Guo, W. Wen, X. Gao, Nanofiber membrane supported lung-on-a-chip microdevice for anti-cancer drug testing, Lab on a Chip 18(3) (2018) 486-495.

[42] N. Higuita-Castro, M.T. Nelson, V. Shukla, P.A. Agudelo-Garcia, W. Zhang, S.M. Duarte-Sanmiguel, J.A. Englert, J.J. Lannutti, D.J. Hansford, S.N. Ghadiali, Using a novel microfabricated model of the alveolar-capillary barrier to investigate the effect of matrix structure on atelectrauma, Scientific Reports 7(1) (2017) 1-13.

CHAPTER 3

MECHANICAL STRETCH MODULATION OF CELL BEHAVIOR*

3.1 Introduction

In vivo, cells undergo mechanical forces under normal physiological conditions. For example, cardiac myocytes are subject to high stress as the heart beats. Vascular endothelial cells undergo blood flow shear stress and blood pressure. The lung alveoli epithelial cells experience periodical mechanical stretch when the lung dilates and constricts.[1] Mechanical forces have profound influences on the formation, function, and homeostasis of cells, tissues, and organs.[2, 3] For example, it has been demonstrated that mechanical stretch enhances vascular network formation, vascular remodeling, and reactive oxygen species production.[4-7] Mechanical stretch also profoundly influences the cell-cell interactions and the barrier functions of the endothelium and epithelium, which constitute key functional components of most organs as selective barriers between different compartments.[8] The deviation in the mechanical forces is often associated with dysfunction of the organs and many diseases. For example, Chronic obstructive pulmonary disease (COPD) is a disease largely characterized by increasing breathlessness, in which the lung experience fast and shallow breaths, and destruction of lung epithelium and capillary endothelium.[9, 10]

To investigate the importance of the mechanical stretch, various cell culture platforms have been developed to subject cells to the mechanical stretch. These

---

* This chapter is partially reproduced from Man, Kun, Jiafeng Liu, Khang Minh Phan, Kai Wang, Jung Yeon Lee, Xiankai Sun, Michael Story, Debabrata Saha, Jun Liao, Hamid Sadat, and Yong Yang. "Dimensionality-Dependent Mechanical Stretch Regulation of Cell Behavior." ACS Applied Materials & Interfaces 14, no. 15 (2022): 17081-17092. DOI: 10.1021/acsami.2c01266. With permission from the American Chemical Society.

platforms usually utilize flexible membranes that can be stretched uniaxially in one dimension (1-D),[11-13] biaxially, circumferentially or radially in two dimensions (2-D),[14-16] or radially in three dimensions (3-D).[17, 18] Of note, the reported breathing human lung-on-a-chip systems with uniaxial mechanical stretch manifest the critical role of mechanical stretch in imitating lung function and diseases, and have been adapted to model several lung diseases and recapitulate therapeutic responses to clinically relevant drugs.[12, 19, 20] Although the impact of mechanical stretch on cell behavior has been acknowledged, most of these platforms do not closely imitate the physiologically relevant mechanical stretch and the effects of stretch dimensionality are often overlooked. Indeed, cells have exhibited distinct behavior under mechanical stretches of different dimensionalities. For example, it has been reported that uniaxial stretch promotes the differentiation of bone marrow mesenchymal stem cells (MSCs) to vascular smooth muscle cells (SMCs) while equiaxial stretch downregulates the expression of SMC markers α-smooth muscle actin (α-SMA) and smooth muscle protein 22-α (SM-22α).[21] Another study showed that, compared to 1-D stretch, 2-D biaxial stretch generates extensive and highly organized elastic fibers, produces more helical collagen fibers, and enhances suture retention strength that is critical for tissue engineered vessels.[22] However, it is still unclear whether cell behavior is dependent on the dimensionality of the mechanical stretch.

To explore the possible effects of mechanical stretch dimensionality on cell behaviors, we designed and engineered cell culture platforms that provided mechanical stretches of 1-D (uniaxial), 2-D (circumferential), and 3-D (radial) and investigated the cell morphology, cell-cell, and cell-substrate interactions of human alveolar basal epithelial

cells (A549) cultured on these platforms. This study revealed that the cells behaved differently in response to the mechanical stretches of different dimensionalities, which provided a foundation for developing lung alveolus chip.

3.2 Materials and Methods

3.2.1 Fabrication of the Mechanical Stretch Platforms

The mechanical stretch platforms comprised two layers sandwiching a thin membrane (Figure 3.1), all made of PDMS (Sylgard 184, Dow Corning, Midland, MI, USA). Both layers were fabricated by casting a PDMS mixture of the resin and curing agent at a weight ratio of 10:1.05 on the 3-D printed molds and curing them on a hot plate at 75 °C for 2 hours.[23] The 3-D molds were fabricated using a 3-D printer (Form 3, Formlabs, Somerville, MA, USA).

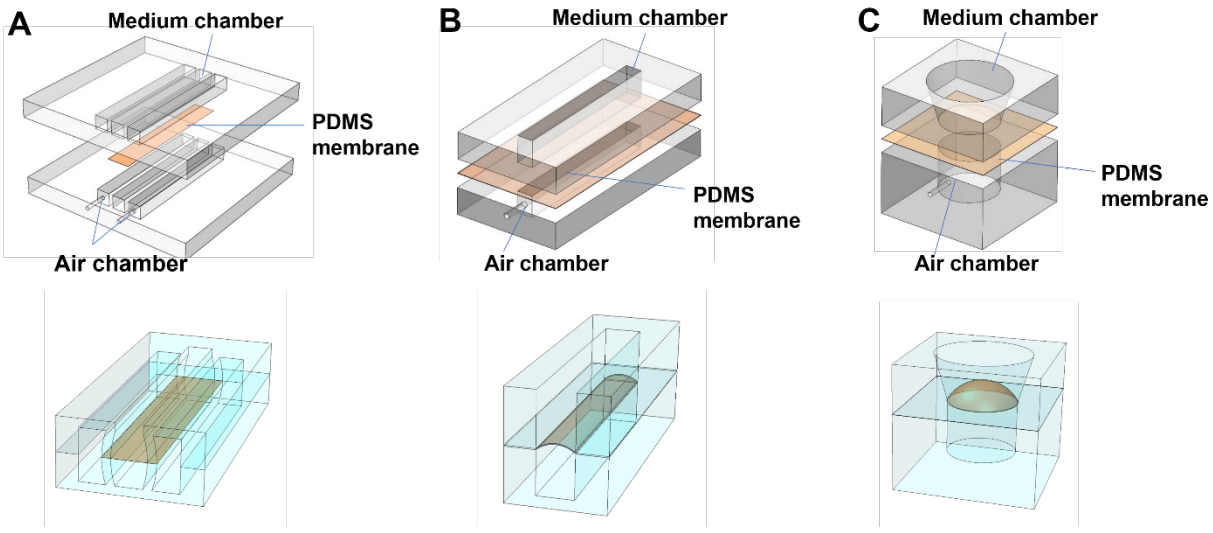

Figure 3.1: Design and fabrication of cell culture platforms with the defined (A) 1-D, (B) 2-D, and (C) 3-D mechanical stretch. The first row provided the exploded views of these platforms. The second row indicated the PDMS membrane deformation after stretching.

The PDMS membrane was prepared by spin-coating the PDMS mixture on a cleaned silicon wafer at 2500 rpm for 1 minute, followed by curing at 75 °C for 1 hour.

The PDMS membrane was then permanently bonded on the bottom layer using PDMS prepolymer adhesive as follows.[24] First, a PDMS mixture was spin-coated on a silicon wafer at 4000 rpm for 2 minutes to form a thin layer. Next, the bottom layer with the opening facing down was stamped on the thin layer for 30 seconds and then transferred onto the PDMS membrane, followed by curing on a hot plate at 75 °C for 1 hour under a compressive pressure of approximately 1 MPa. Lastly, the bottom layer with the membrane was gently peeled off from the silicon wafer, and the extra membrane outside the bottom layer was removed with a razor blade. The membrane suspended over the two side chambers in the 1-D stretch platform was also carefully removed.

Subsequently, the top layer was bonded reversibly on the bottom layer attached with the membrane using the microtransfer assembly technique that we developed previously.[24] First, a PDMS mixture was dissolved in hexane (Thermo Fisher, Waltham, MA, USA) at a ratio of 1:2 (v/v) and spin-coated on a cleaned silicon wafer at 4000 rpm for 2 minutes to form a thin adhesive film, followed by prebaking at 50 °C for 5 minutes. Next, the top layer was stamped on the adhesive film for 30 seconds and then transferred onto the bottom layer bonded with the PDMS membrane. A great attention was paid to aligning the chambers in the top and bottom layers. The resultant assembly was then placed in an oven and cured with a compressive pressure of 1 MPa at 75 °C for 1 hour. Lastly, the stainless-steel tubing was inserted into the pneumatic chamber and secured by applying PDMS mixture around the tubing, followed by curing in an oven at 75 °C for 1 hour. A programmable syringe pump (PHD 2000, Harvard Apparatus, Holliston, MA, USA) was connected to the platform via the stainless-steel tubing.

3.2.2 Characterization of Mechanical Stretches

The deformation (strain) of the PDMS membrane in these platforms was measured using a charge-coupled device (CCD) camera (Model DMK 31, The Imaging Source, Charlotte, NC, USA). For the 1-D stretch platform, several pairs of dots were marked on the PDMS membrane aligned along the stretching direction, and their displacements during the mechanical stretching were recorded using the CCD camera and analyzed to calculate the strain. For the 2-D and 3-D stretch platforms, the PDMS membrane bonded on the pneumatic chamber (with no cell culture chamber attached to obtain clear images) was aligned with the CCD camera and the membrane deformation was imaged. The captured images were adjusted using ImageJ (http://rsb.info.nih.gov/ij/index.html) to obtain the curvilinear profile of the stretched membrane. The curvilinear profiles were then digitalized using GetData Graph Digitalizer (http://www.getdata-graph-digitalizer.com) and analyzed using ImageJ.

For theoretical calculation of strain in the 3-D stretch platform, the ideal mechanical strain is calculated based on two hypotheses: 1) the shape of the stretching membrane is a spherical cap. 2) the gas infused into the pneumatic chamber is incompressible and thus the volume of the spherical cap is equal to volume of air infused in.

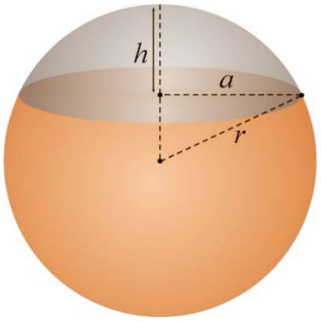

Therefore, the area of the membrane was calculated using Equation 1:

$$S = \pi(a^2 + h^2) \quad (1)$$

where S is the area of the spherical cap, a is the radius of the cap base, which is equal to the radius of the pneumatic chamber, h is the height of the cap as illustrated in the figure above.

The volume of the spherical cap, V, was calculated as

$$V = \left(\frac{\pi h}{6}\right)(3a^2 + h^2) \quad (2)$$

Because a is known and V is the processing parameter equals to volume of air infused in, *h* can be calculated using Equation 2. As such, the ideal area of the stretched membrane can be calculated using Equation 1. By comparing the area of the spherical cap to the original area of the membrane in static state, the strain was calculated.

3.2.3 Cell Culture

Human alveolar basal epithelial cells (A549; Cat#: CCL-185, ATCC, Manassas, VA, USA) were cultured in Dulbecco's Modified Eagle Medium (DMEM) with L-glutamine (Life Technologies, Carlsbad, CA, USA) supplemented with 10% fetal bovine serum (FBS; Sigma-Aldrich, St Louis, MO, USA), 100 U/ml penicillin and 100 µg/ml streptomycin (Life Technologies).

The stretch platforms were oxygen plasma treated at the medium power setting for 20 seconds in a plasma cleaner (Model PDC-001, Harrick Plasma, Ithaca, NY, USA). The PDMS membrane was then coated with 50 µg/ml fibronectin (Corning, Corning, NY, USA) overnight in the incubator. Cells were seeded at a density of 2 x 10^5 cells/cm^2 (unless otherwise specified) and cultured in an incubator of 37 °C and 5% CO_2. Non-adherent cells were removed one day after seeding. The medium was refreshed every 48 hours. The cells were cultured in the platforms under the static condition for 3 days, and then subjected to the mechanical stretch continuously for 7 days. The cells were then

fixed for immunofluorescence staining or collected for the western blot or real-time quantitative reverse transcription-polymerase chain reaction (qRT-PCR) analysis.

3.2.4 Immunofluorescence Staining

The cells were fixed with 1:1 (v/v) of methanol: acetone at -20 °C for 10 minutes, and blocked in tris buffered saline (TBS; KD Medical, Columbia, MD, USA) containing 10% (v/v) FBS, 10% (v/v) goat serum (Sigma-Aldrich), and 1% bovine serum albumin (BSA; Akron Biotech, Boca Raton, FL, USA) at room temperature for 30 minutes. After the cell fixation, the top layer of the platform was removed to facilitate the antibody incubation. The samples were incubated with the primary antibody at 4 °C overnight followed by secondary antibody incubation at room temperature for 1 hour. The information regarding antibodies used for immunostaining and western blot were listed in Table 3.1. F-actin was stained using Alexa Fluor 488 phalloidin (Life Technologies, 1:200 in phosphate buffered saline (PBS)). Upon completion of the antibody incubation, the samples were mounted on the glass slides with ProLong™ Gold Antifade Mountant with DAPI (Life Technologies) and examined using a Nikon Ti eclipse fluorescence microscope (Nikon, Melville, NY, USA).

Table 3.1: Antibodies and dilution information

Antibodies	Vendor	Catalog #	Dilution
F-actin	Life Technologies	MA180729	1:500 (IF)
ZO-3	Life Technologies	364000	1:200 (IF) 1:200 (WB)
Occludin	Life Technologies	331594	1:200 (IF) 1:1000 (WB)
E-cadherin	Life Technologies	131700	1:1000 (IF) 1:1000 (WB)

(table continues)

Antibodies	Vendor	Catalog #	Dilution
ZO-1	Life Technologies	339100	1:100 (IF) 1:500 (WB)
Paxillin	Abcam	ab32084	1:200 (IF) 1:5000 (WB)
YAP	Santa Cruz	sc-101199	1:200 (IF)
Piezo1	Proteintech	15939-1-AP	1:200 (IF)
β-actin	Life Technologies	AM4302	1:1000 (WB)
α-tubulin	Sigma-Aldrich	T9026	1:500 (WB)

3.2.5 Image Analysis

The elongation and orientation of the nuclei were analyzed using ImageJ. The nucleus images were extracted by adjusting threshold of color to achieve best-fitted ellipses, from which the major and minor axis were determined. The elongation was defined by the ratio of nuclear major axis to minor axis. For the 1-D and 2-D stretches, the orientation angle was defined as the angle between the nuclear major axis and the stretch direction. For the 3-D radial stretch, the orientation angle was defined as the angle between a radius and the major axis of the nucleus that was located within 50 μm from the radius (Figure 3.2).

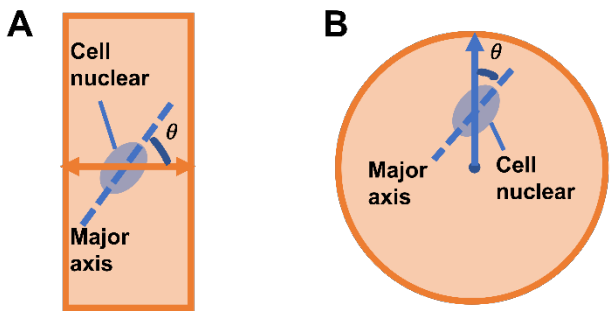

Figure 3.2: Definition of nuclear orientation angle *θ*. The dash lines indicate the nuclear major axis, and the arrows indicate the stretch direction in (A) 1-D and 2-D stretches or (B) the radius of the PDMS membrane in 3-D stretch.

The fluorescence intensity was analyzed using ImageJ. The relative intensity per

cell was calculated by subtracting the background intensity from total intensity and dividing it by cell number in a defined region. The YAP nucleus-to-cytoplasm intensity ratio (N/C) was also analyzed using ImageJ according to the previous report.[23] Briefly, the nuclear areas were outlined using “analyze particle” tool. The YAP fluorescence intensities in the whole cell and the nuclear area were analyzed separately and thus the N/C was calculated.

3.2.6 Western Blotting

The cells on the platforms were rinsed with PBS and lysed using radioimmune precipitation assay (RIPA) buffer (Santa Cruz Biotechnology, Santa Cruz, CA, USA) that contained protease inhibitor for 30 minutes on ice. The cell lysates were then collected and centrifuged at 4 °C and 12000 rpm for 5 minutes. Proteins were quantified using Micro BCA protein assay kit (Thermo Fisher Scientific) following the manufacturer’s protocol. The obtained proteins were mixed with 6×SDS Protein Loading Buffer (Morganville Scientific, Morganville, NJ, USA). The mixture was loaded on 7.5% SDS-PAGE gel and transferred onto polyvinylidene fluoride (PVDF) membrane (Thermo Fisher Scientific). The PVDF membranes were then blocked in 5% nonfat milk (RPI International, Mount Prospect, IL, USA) dissolved in TBS with 0.1% Tween-20 (Thermo Fisher Scientific) at room temperature for 1 hour. Subsequently, the membrane was incubated with primary antibody at 4 °C on a shaker overnight, and then incubated with secondary antibodies for 1 hour at room temperature. The PVDF membrane were visualized by using ECL detection kit (EMD Millipore, Burlington, MA, USA) and the images were acquired by using ChemiDoc MP image system (Bio-Rad, Hercules, CA, USA). The densitometry of protein bands was quantified using ImageJ by measuring the color density of the band

and normalized to the amount of β-actin or α-tubulin in each experiment.

3.2.7 Real-Time qRT-PCR Assay

The total RNA was extracted using Aurum Total RNA Mini Kit (Bio-Rad) following the product protocol and the cDNA was synthesized from total RNA using iScript RT Supermix (Bio-Rad). The synthesis was performed by CFX96 (Bio-Rad) according to the manufacturer's protocol. The concentration of total RNA and cDNA was determined with a NanoDrop ND-1000 (NanoDrop Technologies, Wilmington, Delaware, USA). The qRT-PCR assay samples were prepared according to the protocol of the SsoAdvanced Univ SYBR Grn Suprmix (Bio-Rad). Primer sequences used in qRT-PCR assay were designed according to human piezo1 mRNA sequence (KC602455.1): forward primer, 5'-TTCCCCAAGTACATCCGTGC-3' and reverse primer, 5'-AGGTAGTCGGCCTCCTCATT-3'. qRT-PCR reaction was performed under the following conditions: 40 cycles of 95 °C for 15 seconds, 60 °C for 30 seconds, followed by a melt curve of 65-95 °C at 0.5 °C increments qt 2-5 seconds/step. The results were normalized to α-tubulin expression.

3.2.8 Computational Simulation of 2-D and 3-D Mechanical Stretches

The strain and stress in the PDMS membrane were simulated by using an in-house fluid solver CFDFOAM that we developed previously,[24] coupled with the solid solver Calculix (http://www.calculix.de). The CFDFOAM has been built around OpenFOAM that employs a cell-centered finite volume and conventional body-fitted methods as well as immersed boundary methods for moving/morphing boundaries. Calculix was an open-source finite-element-based solid solver. Fluid flow was computed by solving the Navier–Stokes equation for laminar flows. The second-order numerical schemes were chosen for

the convection and diffusion terms. Euler's method was used for time discretization. The fluid domain was discretized with 112,500 and 68,600 hexahedra dominant elements for 2-D and 3-D cases, respectively. A no-slip boundary condition was applied on all chamber walls. At the inlet of the air chamber, the oscillating velocity mimicking the experimental setup was applied as a Dirichlet boundary condition. In Calculix, the membrane was modeled as a flexible wall that was free to deform, while the sides were fixed. The thin PDMS membrane was decomposed into the 2250 incompatible mode eight-node brick element (C3D8I) for the 2-D case and 2483 C3D8I for the 3-D case. The incomprehensible linear elastic model was used to describe material properties of the membrane.

The open-source coupling library preCICE (https://precice.org) was used as the interface between the two solvers to transfer forces and displacements between them. The serial–implicit coupling scheme was employed. The Inverse Quasi-Newton Broyden (IQN-IMVJ) acceleration method was used to improve the convergence rate. The radial function basic mapping method was employed to map data from one mesh to the other.

3.2.9 Statistical Analysis

Statistical analysis was performed using GraphPad Prism software (GraphPad software, San Diego, CA, USA). *P* values between groups were calculated using unpaired Wilcoxon-Mann-Whitney-Test. $p < 0.05$ was considered statistically significant.

3.3 Results and Discussion

3.3.1 Design and Fabrication of Cell Culture Platforms with Defined Mechanical Stretch

The cell culture platforms were designed to provide defined 1-D, 2-D, or 3-D mechanical stretch to the cells via a flexible PDMS membrane (15 μm in thickness), which

was sandwiched between two PDMS layers (Figure 3.1, Material and Methods Section). The mechanical stretch of distinct dimensionality was executed with different mechanisms. The 1-D stretch platform was adopted from the breathing lung chip.[12] It consisted of two side pneumatic chambers (PCs) and a middle chamber, which was divided by the PDMS membrane to an upper cell culture chamber and a lower chamber. When air was withdrawn from and infused to the two side PCs repeatedly, cyclic uniaxial stretch was generated in the PDMS membrane and the adherent cells. Differently, the 2-D and 3-D stretch platforms contained an upper cell culture chamber and a lower PC separated by the PDMS membrane. When air was pumped in and out of the PC, the PDMS membrane moved up and down, which resulted in a 2-D or 3-D stretch, depending on the geometry of the PDMS membrane. Because of the large aspect ratio (length/width = 10) of the rectangular PDMS membrane in the 2-D platform (Table 3.2), the resultant stretch was 2-D circumferential. The 3-D stretch platform generated 3-D radial stretch due to the circular shape of the PDMS membrane.

Table 3.2: Dimensions of cell culture platforms

	Cell Culture Chamber (mm)	Pneumatic Chamber (mm)
1-D	30 × 3 × 5 (L × W × H)	30 × 3 × 8 (L × W × H)
2-D	30 × 3 × 5 (L × W × H)	30 × 3 × 4 (L × W × H)
3-D	Bottom Radius: 5 Top Radius: 7.5 Height: 5	Radius: 5 Height: 4

These cell culture platforms provided 1-D uniaxial, 2-D circumferential, and 3-D radial mechanical stretches, which imitated three major types of mechanical stretches observed *in vivo*, for instance, the 1-D tensile stretch of skin and skeletal muscles, the 2-D circumferential stretch of blood vessels and intestinal tract, and the 3-D contraction and

expansion of heart and lungs. In addition, these platforms were easy to manufacture, and could readily be scaled up for downstream biological and chemical analyses.

3.3.2 Characterization of the Mechanical Stretches in the Platforms

The strains of the PDMS membrane undergoing a series of deformation levels in the 2-D and 3-D stretch platforms were measured and compared with the theoretical calculation. Take the 3-D mechanical stretch as an example. The images of the PDMS membrane undergoing a series of strains were captured (Figure 3.3A) and processed using ImageJ (Figure 3.3B) to obtain the deformation (black) profiles, which were compared with the theoretical (blue) profiles (Figure 3.3C). The theoretical strains were calculated based on the assumption that the air pumped in/out the PC was incompressible. In the 3-D stretch, the profile of the stretched membrane was treated as an ideal spherical cap, whose base radius (radius of the PC) and volume (gas infused) were known. The linear strain was then calculated from the area of the surface cap (without base). As shown in Figure 3.3D, the deflection between the measured and the calculated strains was less than < 5% when the theoretical linear strain was less than 20% but became evident when the linear strain further increased. The experimental and theoretical strain comparison on the 2-D stretch also showed a similar trend-no significant deflection for a strain less than 20% (not shown). For the 1-D stretch platform, the strain of the PDMS membrane was analyzed based on the displacements of marked dots, which showed that the PDMS membrane deformed uniformly.

Human lung alveolar epithelial cells experience 5-15% linear strain at a frequency of 0.2-0.3 Hz under normal conditions, which approximately corresponds to 10-30% surface area change. It has been reported that about 37% change in the surface area

perturbed the expression of tight junction protein occludin.[14, 25-27] Thus, a maximum of 15% linear strain at a frequency of 0.2 Hz was applied to the epithelial cells cultured on these platforms.

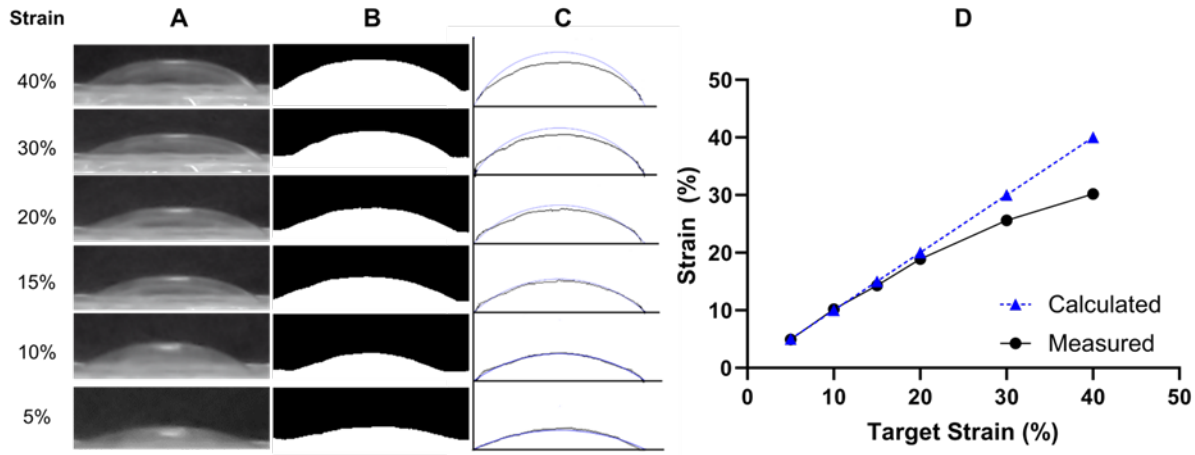

Figure 3.3: Characterization of 3-D stretch platform. (A) Original CCD images of the PDMS membranes experiencing a series of theoretical strains ranging from 5% to 40%. (B) The profiles of the deformed PDMS membranes processed by Image J. (C) The deformed PDMS membrane profiles (black) from ImageJ processing and the theoretical profiles (blue). (D) Comparison of the experimental and theoretical strains.

3.3.3 Mechanical Stretch Dimensionality Dependent Cell Morphology

The A549 cells showed orientation perpendicular to the 1-D and 2-D stretch directions and exhibited a random orientation under the static and 3-D stretch conditions (Figure 3.4A). We further quantified nuclear orientation under the mechanical stretches of different dimensionalities. The A549 cell nuclei oriented randomly under the static and 3-D radial stretch conditions, yet 41% and 39% of the nuclei oriented in a 30^{o} angle (the angular sector of 60-90^{o}) perpendicular to the 1-D and 2-D stretch directions, respectively (Figure 3.4B).

These observations were consistent with the previous report that A549 cells had a slight change in orientation in response to a cyclic 3-D stretch.[28] Note that *in vivo* lung alveolar epithelial cells displayed flattened or cuboidal morphology without

directionality.[29] Our observations showed that the 3-D stretch platform was beneficial for maintaining normal epithelial cell morphology while providing the breathing-like movement. Taken together, our findings suggested that the mechanical stretch of an appropriate dimensionality was important to resemble the normal cell morphology *in vitro*.

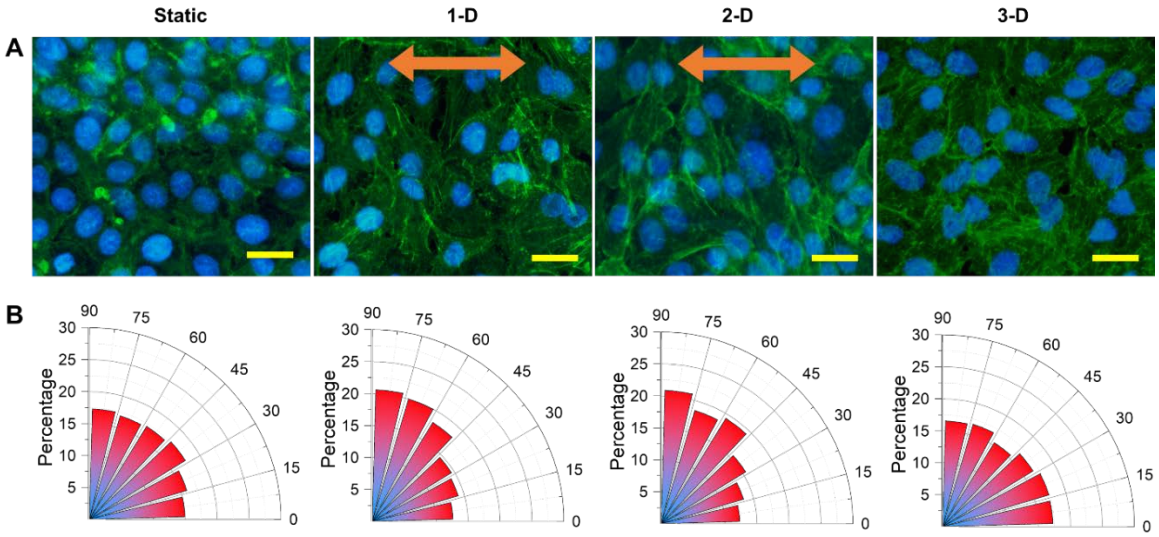

Figure 3.4: Mechanical stretch dimensionality-dependent cell morphology. (A) Representative immunofluorescent images of A549 under static condition and different mechanical stretches. Green, F-actin; blue, nuclei. The arrows indicate the stretch direction. Scale bars: 20 μm. (B) Rose plots of A549 nuclear orientation. A total of 900–1600 cells were analyzed.

3.3.4 Mechanical Stretch Dimensionality Dependent Cell-cell Interactions

Cell-cell interactions are critical for the barrier function of epithelia. We thus examined the effects of mechanical stretch dimensionality on the expression of hallmark tight junction proteins such as zonula occludens (ZO) proteins and occludin, as well as adherens junction protein E-cadherin. After subjected to the mechanical stretches for seven days, the immunofluorescence observations indicated the formation of the epithelial monolayer connected by the E-cadherin and the epithelial cells exhibited the upregulated expression of ZO-3 and occludin compared to the static control (Figure 3.5A). The western blot analysis confirmed that the mechanical stretches significantly increased

the expression of ZO-3 and occludin in comparison with the static control (Figure 3.5B, C). Surprisingly, the expression of ZO-3 and occludin in A549 cells undergoing the 3-D radial stretch was generally higher than those exposed to the 1-D and 2-D stretches.

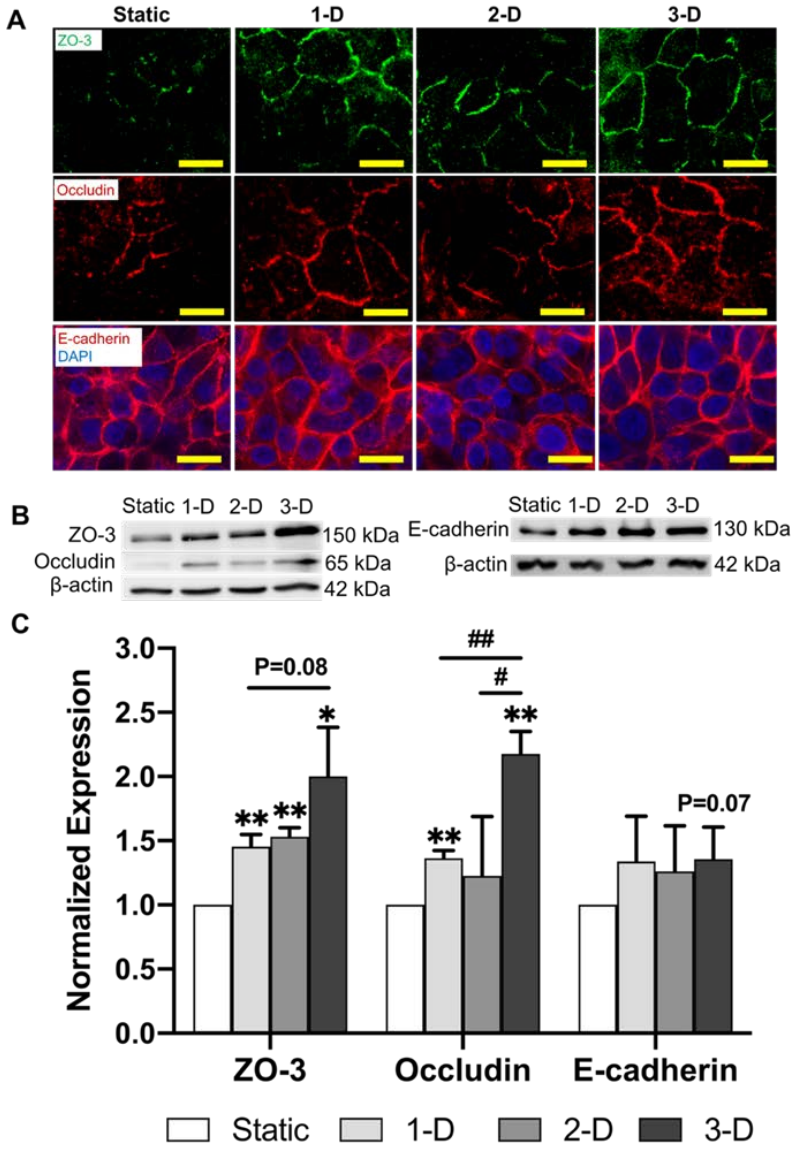

Figure 3.5: Mechanical stretch dimensionality dependent epithelial cell-cell interactions. (A) Representative immunofluorescence images of A549 cells under static and various stretch conditions. Scale bars: 20 um. (B) Western blotting of ZO-3, occludin, and E-cadherin in A549 under the static and various stretch conditions. (C) Densitometric analysis of ZO-3, occludin and E-cadherin expressions from the western blotting (n=3). All the data were normalized to the mean value of the static control. *: $p < 0.05$, **: $p < 0.01$ compared to the static controls. $^{\#}$: $p < 0.05$, $^{\#\#}$: $p < 0.01$ between groups.

Among the ZO proteins, ZO-1 and ZO-2 were expressed in various cell types, including all epithelial and endothelial cells, and ZO-3 was concentrated at the epithelium junctions.[30] As such, we examined and noticed the differences in ZO-3 for the epithelial cells under various mechanical stretches compared to the static condition. We also examined ZO-1 for the epithelial cells but did not observe significant difference in ZO-1 expression among these groups (data not shown). Cell-cell adhesion can be mediated by cadherin-based adherens junctions, and ZO proteins can interact directly with transmembrane protein occludin.[31] Therefore, our results indicated that the mechanical stretch generally enhanced the cell-cell interactions, and more importantly, the effects of mechanical stretch on the cell-cell interactions were dimensionality dependent.

3.3.5 Mechanical Stretch Dimensionality Dependent Mechanosensing

To understand the effects of mechanical stretch dimensionality on cell behavior, we further explored cell sensing the mechanical stretches from focal adhesions through cytoskeleton to nucleus. We first examined the mechanosensing at a low cell seeding density (6,000 cells/cm^2), which alleviated the influence of cell-cell interactions. A549 cells exhibited mature focal adhesion protein paxillin under static condition (indicated by the arrows in Figure 3.6A). In contrast, fewer mature paxillin was observed in the cells experiencing the mechanical stretches and particularly the paxillin was diffuse under the 3-D stretch. In addition, the paxillin was redistributed in the peri-nuclear regions under the mechanical stretches. The fluorescence intensity analysis showed an upregulation of paxillin and F-actin in the A549 cells under the 1-D and 3-D stretches in comparison with the static control and the 2-D stretch (Figure 3.6D, E). Moreover, the nucleocytoplasmic localization analysis of yes-associated protein (YAP) showed lower YAP N/C ratios under

1-D and 3-D stretches compared with the static and 2-D stretch conditions (Figure 3.6B, C, F). Furthermore, we examined a major mechanosensing channel piezo1. Piezo1 exhibited the significantly higher expression under both the 1-D and 3-D stretches than those under the static and 2-D stretch conditions (Figure 3.6G). Next, we evaluated the effects of cell-cell interactions on mechanosensing by increasing the cell seeding density from 6,000 to 200,000 cells/cm^2. The higher cell density diminished the influence of the mechanical stretches on the expression of paxillin and F-actin (except the 3-D stretch) and YAP N/C ratio in the epithelial cells (Figure 3.7A-C). However, the mechanical stretches still profoundly increased the piezo1 expression, as shown in the *q*PCR analysis (Figure 3.7D). Of note, the dimensionality effect of the mechanical stretch on the piezo1 expression was still evident – the peizo1 expression reached the highest level in the epithelial cells undergoing the 3-D stretch.

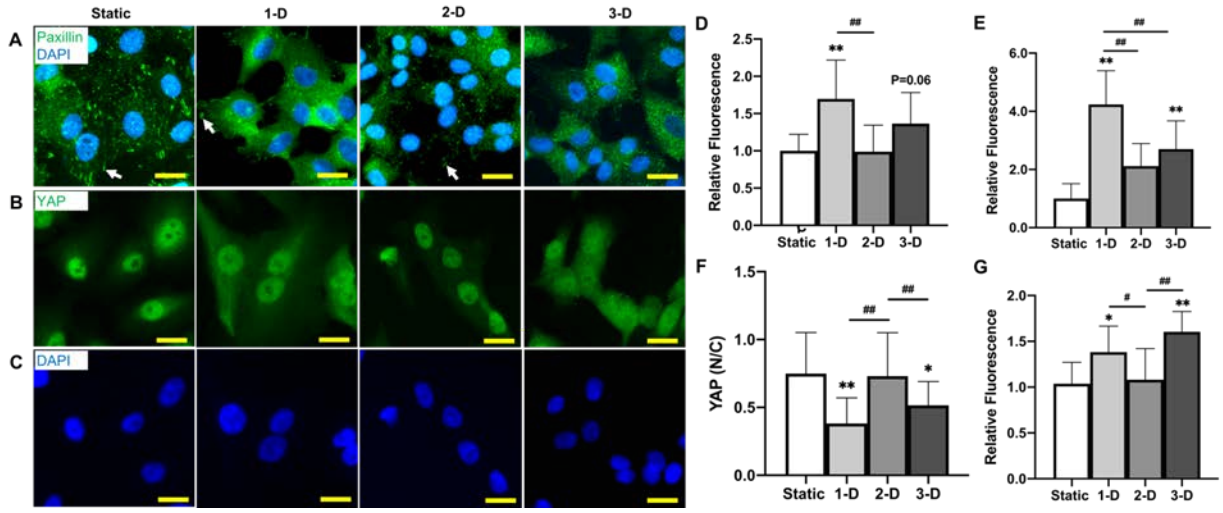

Figure 3.6: Mechanosensing of the epithelial cells at a low cell seeding density (6000 cells/cm^2). Representative immunofluorescence images of A549 cells stained with (A) paxillin and nuclei (DAPI), and (B) YAP with (C) DAPI-labeled nuclei. Scale bars: 20 μm. The white arrowheads in panel A indicate mature paxillin. The expressions of (D) paxillin (n = 100) and (E) F-actin (n = 100) based on fluorescence intensity analyses. (F) YAP N/C ratio analyzed over n > 300 cells. (G) Piezo1 (n = 1000) expression based on fluorescence intensity analyses. *: P < 0.05, **: P < 0.01 compared to the static controls. $^{\#}$: P < 0.05, $^{\#\#}$: P < 0.01 between groups.

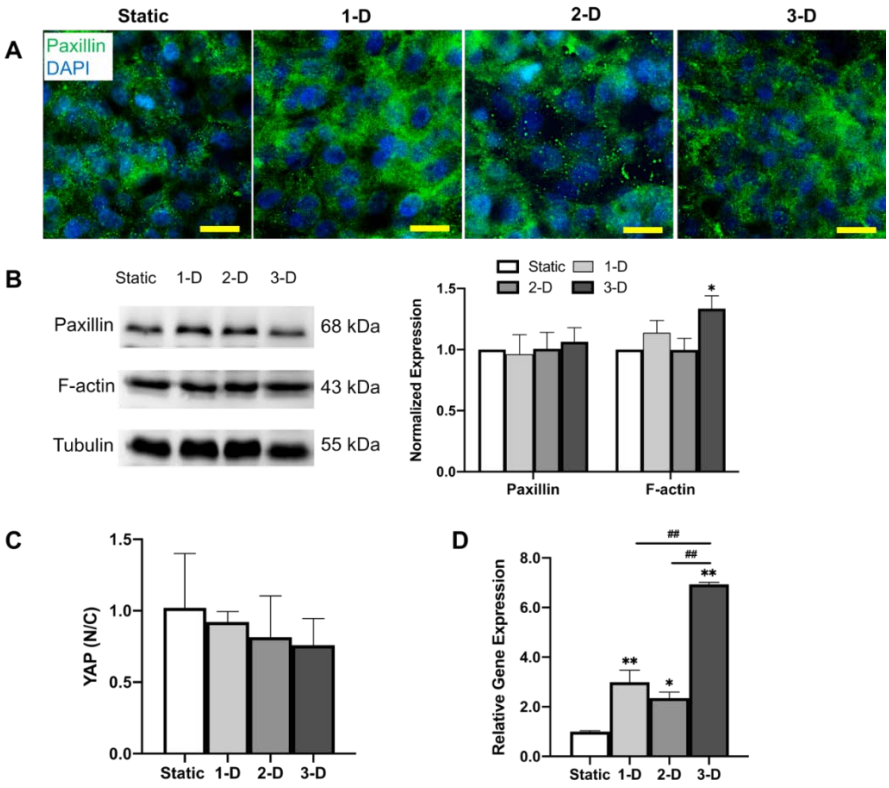

Figure 3.7: Mechanosensing of the epithelial cells at a high cell seeding density (200,000 cells/cm^2). (A) Representative immunofluorescence images of A549 cells stained with paxillin and DAPI. Scale bars: 20μm. (B) Western blotting of paxillin and F-actin in A549 cells under the static and various stretch conditions and densitometric analysis from the western blotting (n=3). (C) YAP N/C ratio analyzed over n > 300 cells. (D) Piezo1 expression analyzed using qRT-PCR (n=3). *: $p < 0.05$, **: $p < 0.01$ compared to the static controls. $^{\#}$: $p < 0.05$, $^{\#\#}$: $p < 0.01$ between groups.

Mechanical signals can be transduced through cell-matrix and cell-cell contacts to regulate cell behavior. Focal adhesions sense mechanical stretching and transmit the mechanical signal to actin cytoskeleton, which was required for the recruitment and retention of adherens junction and tight junction proteins and, subsequently the formation of junctional complex.[32-34] In our study, when subjected to mechanical stretches, the epithelial cells displayed the peri-nuclear distribution of paxillin, which was consistent with the previous report.[35] Particularly, the paxillin expression was significantly increased in A549 cells that were subjected to 1-D and 3-D stretches, which facilitated cell attachment to the membrane and the mechanical signal transmission to actin cytoskeleton. The

resultant upregulation of F-actin expression enhanced the tight junction formation as exhibited in the increased expression in tight junction protein ZO-3 and adherens junction protein E-cadherin. The formation of cell junctions plays an important role in the barrier permeability and integrity.[36] At the high seeding density, cell-cell interactions were further enhanced by accumulation of adherens junction and tight junction proteins in cell-cell contacts, which competed with and abated the cell adhesion on the membrane.

As a major downstream effector of the Hippo pathway, which was important in regulating actin cytoskeleton, YAP and TAZ (transcriptional co-activator with PDZ-binding motif) have been revealed as critical factors in stem cell fate decision and endothelial/epithelial barrier function and maintenance.[37-39] YAP/TAZ intracellular localization and activity are sensitive to substrate stiffness and nanotopography and mechanical strain.[40-43] YAP tends to be localized in nucleus during cell proliferation and in cytoplasm at a high cell density.[44] In our study, the YAP N/C ratio of A549 cells under 1-D and 3-D stretch was lower than other groups. This finding suggested that the mechanical stretch, particularly the physiological 3-D stretch benefited the maintenance of primary phenotype of A549 cells, which have been used as a model for primary human pulmonary alveolar type II (ATII) cells in respiratory research.[45] Nevertheless, at the higher seeding density, the increased cell-cell contacts undermined the stretching effects, and the YAP N/C ratio difference became insignificant among the groups.

As revealed in this study, the mechanical stretch can promote the formation of focal adhesions and the actin cytoskeleton and thus facilitate the recruitment and retention of adherens junction and tight junction proteins. Through the contractile actin cytoskeleton, the mechanical signal was transmitted to the nucleus to regulate the

transport of transcriptional regulators such as YAP. Note that cytoplasm YAP localization in epithelial cells was associated with cell extrusion and epithelium homeostasis. Moreover, in addition to sensing substrate stiffness and confinement and shear stress of the local cellular environment,[46-49] the mechanosensing channel piezo1 was sensitive to the physiological mechanical stretch. Our findings manifested that the epithelial cells were sensitive to the mechanical stretches, especially the physiologically relevant stretch, and the physiological mechanical stretch played an important role in the development, function, and homeostasis of epithelia.

3.3.6 Heterogeneity in Cell Behavior and Mechanical Stretch

While the cells exhibited a stretch dimensionality-dependent behavior, the variation in cell behavior across the PDMS membrane upon mechanical stretch was noticed. For example, from the center to the edge of the PDMS membrane, the epithelial cells showed different expressions of ZO-3 (Figure 3.8). Additionally, the nuclear orientation of the epithelial cells was not uniform across the membrane under the 1-D and 2-D stretch (Figure 3.9). Furthermore, the nuclear elongation of the epithelial cells was not substantially affected by the stretch dimensionality or the location across the membrane (Figure 3.10).

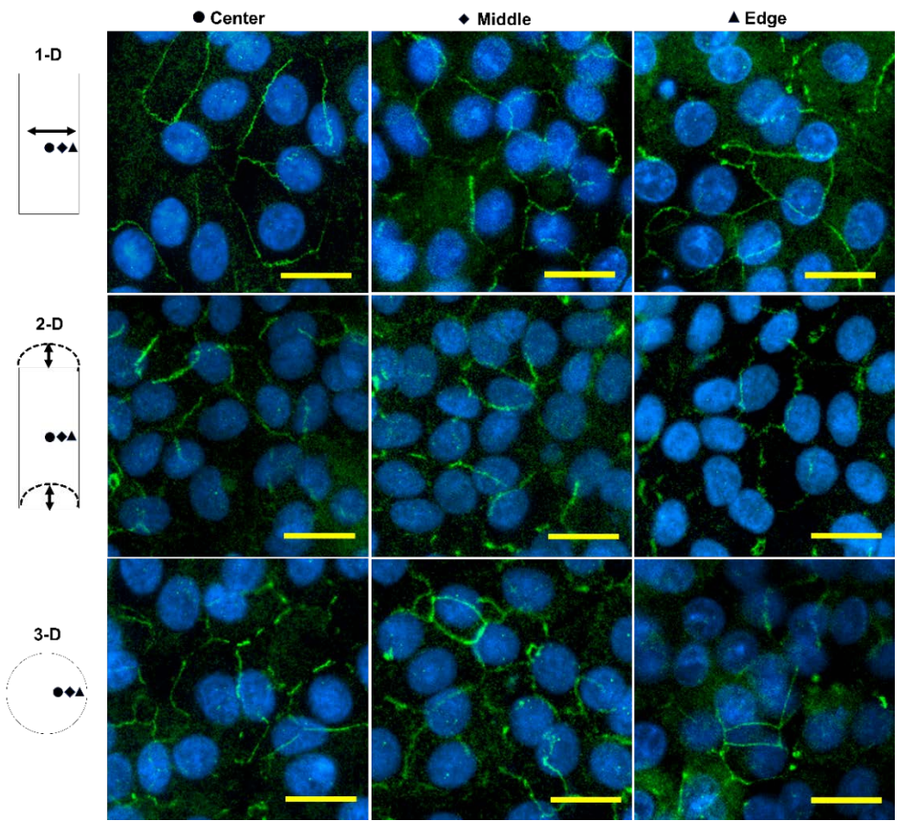

Figure 3.8: Representative immunofluorescence images of the A549 cells across the PDMS membrane subjected to 1-D (first row), 2-D (second row), and 3-D (third row) stretches. Green: ZO-3, Blue: nuclei. Scale bars: 20μm.

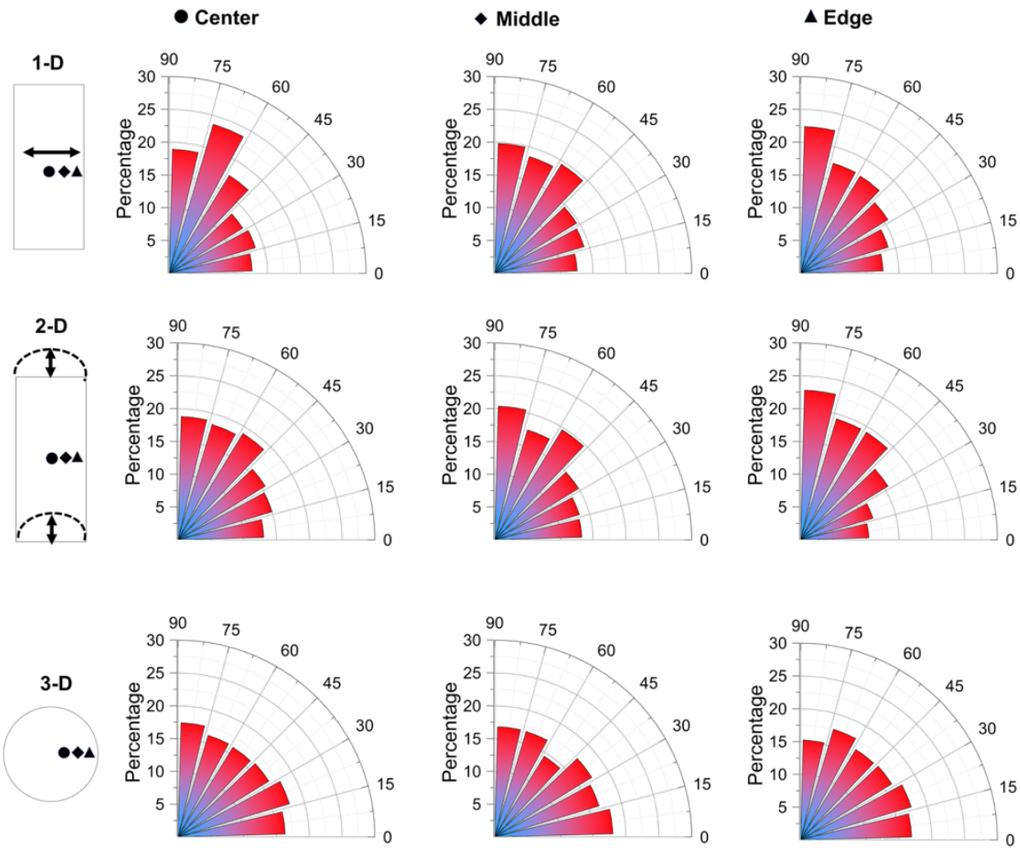

Figure 3.9: Rose plots of nuclear orientation of the A549 cells on the center, middle, and edge of the membrane subjected to the mechanical stretches. 800-1000 cells were analyzed for each plot.

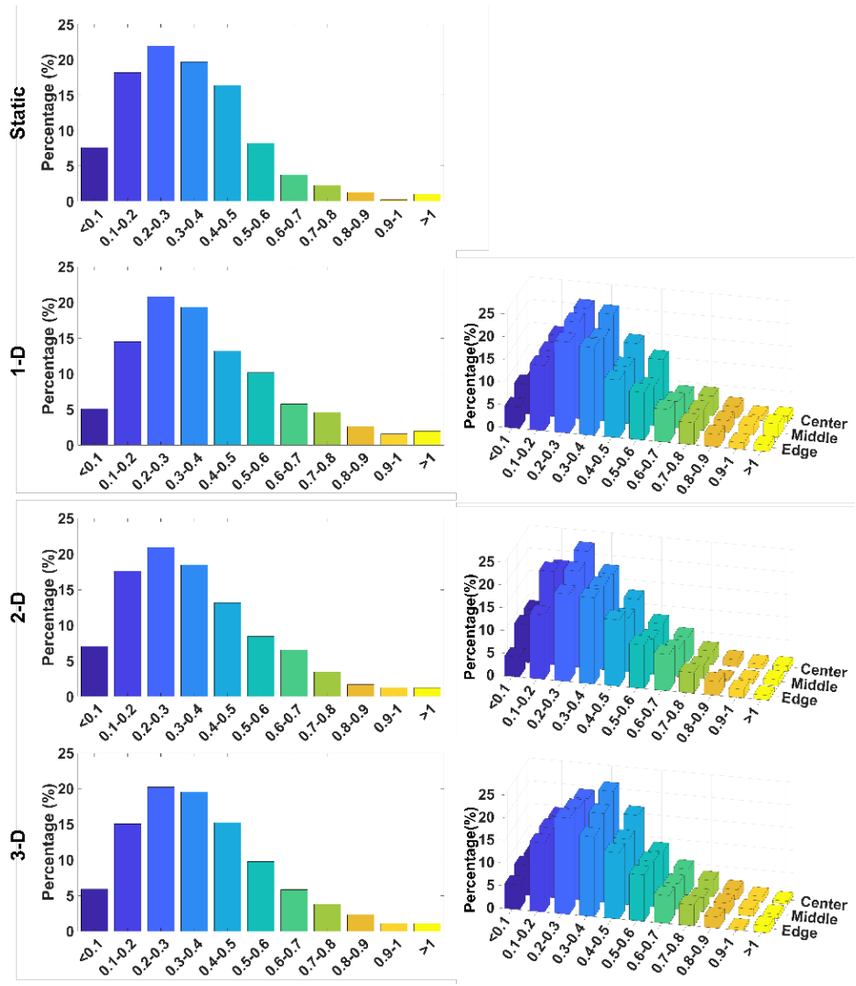

Figure 3.10: Nuclear elongation of epithelial cells under static and stretch conditions (first column) and their distributions on the center, middle, and edge of the PDMS membranes (second column). A total of 1000–1200 cells were analyzed in each plot.

To understand the heterogeneous cell behavior, we performed the computational simulation of the stress and strain in the PDMS membrane undergoing 2-D and 3-D stretches. It was shown that, upon the 3-D stretch, the stresses, and strains across the PDMS membrane displayed heterogeneous distributions (Figure 3.11). Moreover, although the linear strain on the membranes was 15%, the instantaneous strain and stress could be higher than the mean values, particularly at the membrane edge. These high strain/stress in the edge areas were likely larger than the physiological ranges and could decrease tight junction protein expression,[14, 50-52] as demonstrated in the discontinuous expressions of the epithelial ZO-3 at the edge areas under the 3-D stretch. The simulation of 2-D stretch also showed a similar trend. In addition, it was reported that when human dermal microvascular endothelial cells were subjected to cyclic 2-D biaxial and 3-D radial stretch the cells were compressed rather than stretched within 10% of the membrane edge for both 2-D and 3-D stretch.[28] It was speculated that this edge compression effect together with the heterogeneous strain and stress distributions contributed to the heterogeneous cell behavior. Mapping the cell tension across the membrane in connection with the strain/stress distribution in the membrane would further explain the heterogenous cell behavior. Regardless of the heterogeneity, the effects of the stretch dimensionality on the cells were significant.

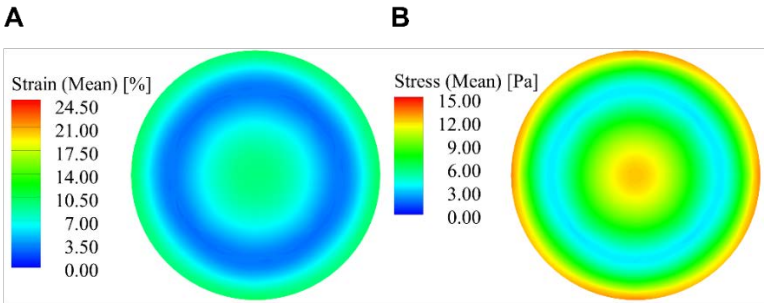

Figure 3.11: Computational analyses of the (A) strain and (B) stress distribution on the PDMS membrane experiencing 3-D stretch.

Although the cells experienced different levels of mechanical strain across the membrane, the computational simulation showed that the time-averaged mean strains were 7.0 and 5.6% for 2-D and 3-D stretches, respectively. In both cases, the strain within 80% of the central area was in the range of 5–15%, and therefore, these platforms provided physiologically relevant mechanical stretches. This study focused on the investigation of dimensionality effects of the mechanical stretches, and the cells were grown on the PDMS membrane. Yet, these platforms could be readily modified by placing a cell-laden 3-D matrix on the PDMS membrane to closely imitate *in vivo* scenarios.

3.4 Conclusion

This work reported the engineering of cell culture platforms with 1-D uniaxial, 2-D circumferential, or 3-D radial mechanical stretch and the investigation on the dimensionality effects of the mechanical stretches on the behavior of human alveolar epithelial cells. The cell behavior was sensitive to the mechanical stretch, which showed a profound influence on cell morphology, cell–cell and cell–substrate interactions. Intriguingly, the cells responded to the mechanical stretch in a stretch dimensionality-dependent manner. The cell–cell interactions in the epithelial layer were mostly enhanced by the *in-vivo*-like mechanical stretch, suggesting that the 3-D radial stretch favored the formation of the epithelium. This finding manifests the importance of faithfully resembling the physiologically relevant mechanical stretch in *in vitro* organ models.

3.5 References

[1] C. OpenStax, Anatomy and physiology, Rice University 2013.

[2] T. Mammoto, D.E. Ingber, Mechanical control of tissue and organ development, Development 137(9) (2010) 1407-20.

[3] A. Buchmann, M. Alber, J.J. Zartman, Sizing it up: the mechanical feedback hypotheswas of organ growth regulation, Semin Cell Dev Biol 35 (2014) 73-81.

[4] T.H. Cheng, N.L. Shih, S.Y. Chen, S.H. Loh, P.Y. Cheng, C.S. Tsai, S.H. Liu, D.L. Wang, J.J. Chen, Reactive oxygen species mediate cyclic strain-induced endothelin-1 gene expression via Ras/Raf/extracellular signal-regulated kinase pathway in endothelial cells, Journal of molecular and cellular cardiology 33(10) (2001) 1805-1814.

[5] W. Li, B.E. Sumpio, Strain-induced vascular endothelial cell proliferation requires PI3K-dependent mTOR-4E-BP1 signal pathway, American Journal of Physiology-Heart and Circulatory Physiology 288(4) (2005) H1591-H1597.

[6] I.S. Joung, M.N. Iwamoto, Y.-T. Shiu, C.T. Quam, Cyclic strain modulates tubulogeneswas of endothelial cells in a 3D tissue culture model, Microvascular research 71(1) (2006) 1-11.

[7] K.G. Birukov, Cyclic stretch, reactive oxygen species, and vascular remodeling, Antioxidants & redox signaling 11(7) (2009) 1651-1667.

[8] E. Rodriguez-Boulan, G. Kreitzer, A. Müsch, Organization of vesicular trafficking in epithelia, Nature reviews Molecular cell biology 6(3) (2005) 233-247.

[9] C.F. Vogelmeier, G.J. Criner, F.J. Martinez, A. Anzueto, P.J. Barnes, J. Bourbeau, B.R. Celli, R. Chen, M. Decramer, L.M. Fabbri, P. Frith, D.M. Halpin, M.V. Lopez Varela, M. Nishimura, N. Roche, R. Rodriguez-Roisin, D.D. Sin, D. Singh, R. Stockley, J. Vestbo, J.A. Wedzicha, A. Agusti, Global Strategy for the Diagnosis, Management, and Prevention of Chronic Obstructive Lung Disease 2017 Report. GOLD Executive Summary, Am J Respir Crit Care Med 195(5) (2017) 557-582.

[10] W. MacNee, Pathology, pathogenesis, and pathophysiology, Bmj 332(7551) (2006) 1202-1204.

[11] M. Moretti, A. Prina-Mello, A.J. Reid, V. Barron, P.J. Prendergast, Endothelial cell alignment on cyclically-stretched silicone surfaces, Journal of Materials Science: Materials in Medicine 15(10) (2004) 1159-1164.

[12] D. Huh, B.D. Matthews, A. Mammoto, M. Montoya-Zavala, H.Y. Hsin, D.E. Ingber, Reconstituting organ-level lung functions on a chip, Science 328(5986) (2010) 1662-1668.

[13] P. Liu, Y. Song, Y. Zhou, Y. Liu, T. Qiu, Q. An, J. Song, P. Li, Y. Shi, S. Li, Cyclic mechanical stretch induced smooth muscle cell changes in cerebral aneurysm progress by reducing collagen type IV and collagen type VI levels, Cellular Physiology and Biochemistry 45(3) (2018) 1051-1060.

[14] K.J. Cavanaugh, Jr., J. Oswari, S.S. Margulies, Role of stretch on tight junction structure in alveolar epithelial cells, Am J Respir Cell Mol Biol 25(5) (2001) 584-91.

[15] G.A. Giridharan, M.D. Nguyen, R. Estrada, V. Parichehreh, T. Hamid, M.A. Ismahil, S.D. Prabhu, P. Sethu, Microfluidic cardiac cell culture model (μCCCM), Analytical chemistry 82(18) (2010) 7581-7587.

[16] J. Zhou, L.E. Niklason, Microfluidic artificial “vessels” for dynamic mechanical stimulation of mesenchymal stem cells, Integrative Biology 4(12) (2012) 1487-1497.

[17] A.O. Stucki, J.D. Stucki, S.R. Hall, M. Felder, Y. Mermoud, R.A. Schmid, T. Geiser, O.T. Guenat, A lung-on-a-chip array with an integrated bio-inspired respiration mechanism, Lab Chip 15(5) (2015) 1302-10.

[18] Y. Mermoud, M. Felder, J.D. Stucki, A.O. Stucki, O.T. Guenat, Microimpedance tomography system to monitor cell activity and membrane movements in a breathing lung-on-chip, Sensors and Actuators B: Chemical 255 (2018) 3647-3653.

[19] D. Huh, D.C. Leslie, B.D. Matthews, J.P. Fraser, S. Jurek, G.A. Hamilton, K.S. Thorneloe, M.A. McAlexander, D.E. Ingber, A human disease model of drug toxicity-induced pulmonary edema in a lung-on-a-chip microdevice, Sci. Transl. Med. 4(159) (2012) 159ra147.

[20] K.H. Benam, R. Villenave, C. Lucchesi, A. Varone, C. Hubeau, H.-H. Lee, S.E. Alves, M. Salmon, T.C. Ferrante, J.C. Weaver, Small airway-on-a-chip enables analyswas of human lung inflammation and drug responses in vitro, Nature methods 13(2) (2016) 151-157.

[21] J.S. Park, J.S.F. Chu, C. Cheng, F. Chen, D. Chen, S. Li, Differential effects of equiaxial and uniaxial strain on mesenchymal stem cells, Biotechnology and bioengineering 88(3) (2004) 359-368.

[22] A.H. Huang, J.L. Balestrini, B.V. Udelsman, K.C. Zhou, L. Zhao, J. Ferruzzi, B.C. Starcher, M.J. Levene, J.D. Humphrey, L.E. Niklason, Biaxial stretch improves elastic fiber maturation, collagen arrangement, and mechanical properties in engineered arteries, Tissue Engineering Part C: Methods 22(6) (2016) 524-533.

[23] B.D. Cosgrove, K.L. Mui, T.P. Driscoll, S.R. Caliari, K.D. Mehta, R.K. Assoian, J.A. Burdick, R.L. Mauck, N-cadherin adhesive interactions modulate matrix mechanosensing and fate commitment of mesenchymal stem cells, Nature materials 15(12) (2016) 1297-1306.

[24] M. Heydari, H. Sadat-Hosseini, Analyswas of propeller wake field and vortical structures using k - omega SST Method, Ocean Eng 204 (2020).

[25] D.J. Tschumperlin, S.S. Margulies, Equibiaxial deformation-induced injury of alveolar epithelial cells in vitro, American Journal of Physiology-Lung Cellular and Molecular Physiology 275(6) (1998) L1173-L1183.

[26] E. Roan, C.M. Waters, What do we know about mechanical strain in lung alveoli?, American Journal of Physiology-Lung Cellular and Molecular Physiology 301(5) (2011) L625-L635.

[27] M.A. Russo, D.M. Santarelli, D. O'Rourke, The physiological effects of slow breathing in the healthy human, Breathe 13(4) (2017) 298-309.

[28] Y. Kamotani, T. Bersano-Begey, N. Kato, Y.C. Tung, D. Huh, J.W. Song, S. Takayama, Individually programmable cell stretching microwell arrays actuated by a Braille display, Biomaterials 29(17) (2008) 2646-2655.

[29] C.R. Rackley, B.R. Stripp, Building and maintaining the epithelium of the lung, The Journal of clinical investigation 122(8) (2012) 2724-2730.

[30] A. Inoko, M. Itoh, A. Tamura, M. Matsuda, M. Furuse, S. Tsukita, Expression and distribution of ZO-3, a tight junction MAGUK protein, in mouse tissues, Genes to Cells 8(11) (2003) 837-845.

[31] H.K. Campbell, J.L. Maiers, K.A. DeMali, Interplay between tight junctions & adherens junctions, Experimental cell research 358(1) (2017) 39-44.

[32] A.S. Fanning, T.Y. Ma, J.M. Anderson, Isolation and functional characterization of the actin-binding region in the tight junction protein ZO-1, The FASEB Journal 16(13) (2002) 1-23.

[33] A.I. Ivanov, D. Hunt, M. Utech, A. Nusrat, C.A. Parkos, Differential roles for actin polymerization and a myosin II motor in assembly of the epithelial apical junctional complex, Molecular biology of the cell 16(6) (2005) 2636-2650.

[34] C.M. Niessen, D. Leckband, A.S. Yap, Tissue organization by cadherin adhesion molecules: dynamic molecular and cellular mechanisms of morphogenetic regulation, Physiological reviews 91(2) (2011) 691-731.

[35] R.A. Thomas, J.C. Norman, T.T. Huynh, B. Williams, S.J. Bolton, A.J. Wardlaw, Mechanical stretch has contrasting effects on mediator release from bronchial epithelial cells, with a rho-kinase-dependent component to the mechanotransduction pathway, Resp Med 100(9) (2006) 1588-1597.

[36] E. Dejana, E. Tournier-Lasserve, B.M. Weinstein, The Control of Vascular Integrity by Endothelial Cell Junctions: Molecular Baswas and Pathological Implications, Dev. Cell 16(2) (2009) 209-221.

[37] C. Yang, M.W. Tibbitt, L. Basta, K.S. Anseth, Mechanical memory and dosing influence stem cell fate, Nat. Mater. 13(6) (2014) 645-52.

[38] H.J. Choi, H. Zhang, H. Park, K.S. Choi, H.W. Lee, V. Agrawal, Y.M. Kim, Y.G. Kwon, Yes-associated protein regulates endothelial cell contact-mediated expression of angiopoietin-2, Nature communications 6 (2015) 6943.

[39] J. Hicks-Berthet, B. Ning, A. Federico, A. Tilston-Lunel, A. Matschulat, X. Ai, M.E. Lenburg, J. Beane, S. Monti, X. Varelas, Yap/Taz inhibit goblet cell fate to maintain lung epithelial homeostasis, Cell Rep 36(2) (2021) 109347.

[40] S. Dupont, L. Morsut, M. Aragona, E. Enzo, S. Giulitti, M. Cordenonsi, F. Zanconato, J. Le Digabel, M. Forcato, S. Bicciato, N. Elvassore, S. Piccolo, Role of YAP/TAZ in mechanotransduction, Nature 474(7350) (2011) 179-83.

[41] D. Mosqueira, S. Pagliari, K. Uto, M. Ebara, S. Romanazzo, C. Escobedo-Lucea, J. Nakanishi, A. Taniguchi, O. Franzese, P. Di Nardo, M.J. Goumans, E. Traversa, O.P. Pinto-do, T. Aoyagi, G. Forte, Hippo pathway effectors control cardiac progenitor cell fate by acting as dynamic sensors of substrate mechanics and nanostructure, ACS Nano 8(3) (2014) 2033-47.

[42] G. Halder, S. Dupont, S. Piccolo, Transduction of mechanical and cytoskeletal cues by YAP and TAZ, Nat. Rev. Mol. Cell Biol. 13(9) (2012) 591-600.

[43] B.W. Benham-Pyle, B.L. Pruitt, W.J. Nelson, Mechanical strain induces E-cadherin–dependent Yap1 and β-catenin activation to drive cell cycle entry, Science 348(6238) (2015) 1024-1027.

[44] M. Cobbaut, S. Karagil, L. Bruno, M.D.C. Diaz de la Loza, F.E. Mackenzie, M. Stolinski, A. Elbediwy, Dysfunctional Mechanotransduction through the YAP/TAZ/Hippo Pathway as a Feature of Chronic Disease, Cells 9(1) (2020) 151.

[45] J.R. Cooper, M.B. Abdullatif, E.C. Burnett, K.E. Kempsell, F. Conforti, H. Tolley, J.E. Collins, D.E. Davies, Long Term Culture of the A549 Cancer Cell Line Promotes Multilamellar Body Formation and Differentiation towards an Alveolar Type II Pneumocyte Phenotype, PLoS One 11(10) (2016) e0164438.

[46] B. Coste, J. Mathur, M. Schmidt, T.J. Earley, S. Ranade, M.J. Petrus, A.E. Dubin, A. Patapoutian, Piezo1 and Piezo2 are essential components of distinct mechanically activated cation channels, Science 330(6000) (2010) 55-60.

[47] S.M. Cahalan, V. Lukacs, S.S. Ranade, S. Chien, M. Bandell, A. Patapoutian, Piezo1 links mechanical forces to red blood cell volume, Elife 4 (2015).

[48] M. Segel, B. Neumann, M.F.E. Hill, I.P. Weber, C. Viscomi, C. Zhao, A. Young, C.C. Agley, A.J. Thompson, G.A. Gonzalez, A. Sharma, S. Holmqvist, D.H. Rowitch, K. Franze, R.J.M. Franklin, K.J. Chalut, Niche stiffness underlies the ageing of central nervous system progenitor cells, Nature 573(7772) (2019) 130-134.

[49] J. Liu, Y. Yang, Y. Liu, Piezo1 plays a role in optic nerve head astrocyte reactivity, Experimental Eye Research 204 (2021) 108445.

[50] K.G. Birukov, J.R. Jacobson, A.A. Flores, S.Q. Ye, A.A. Birukova, A.D. Verin, J.G.N. Garcia, Magnitude-dependent regulation of pulmonary endothelial cell barrier function by cyclic stretch, American Journal of Physiology-Lung Cellular and Molecular Physiology 285(4) (2003) L785-L797.

[51] M.A. Anwar, J. Shalhoub, C.S. Lim, M.S. Gohel, A.H. Davies, The effect of pressure-induced mechanical stretch on vascular wall differential gene expression, Journal of vascular research 49(6) (2012) 463-478.

[52] Y. Yang, S. Kimura-Ohba, J.F. Thompson, V.M. Salayandia, M. Cosse, L. Raz, F.Y. Jalal, G.A. Rosenberg, Vascular tight junction disruption and angiogeneswas in spontaneously hypertensive rat with neuroinflammatory white matter injury, Neurobiology of disease 114 (2018) 95-110.

CHAPTER 4

MODULATION OF STEM CELL BEHAVIOR IN BIOENGINEERED STEM CELL NICHE

4.1 Introduction

Stem cells can provide unlimited cell sources and hold tremendous potential for cell-based therapies, disease modeling, and pharmaceutical applications.[1] Preclinical and clinical applications of stem cells demand large quantities of stem cells. For instance, 10^7–10^{10} or even more human pluripotent stem cells (hPSCs) are essential for their clinical use.[1] Conventionally, stem cells are cultured on two-dimensional (2D) tissue culture (TC) plastic such as flasks, and cell cultivation can be scaled up using multilayer cell factories. However, stem cells are likely to lose their regenerative capability quickly on 2D culture, which has proven difficult to scale up at the commercial scale.[2] Bioreactors have also been used to manufacture stem cells, yet high shear stress in bioreactors may be detrimental to cells. Because of the diminishment of the stemness and uncontrolled differentiation of stem cells in the process of *in vitro* cell expansion,[3] the effective, robust, and scalable bioprocess is critical to realizing stem cell potentials.

Various strategies have been developed to maintain the stemness and control the differentiation of stem cells cultured *in vitro*. In addition to biochemical factors (*e.g.*, combined use of multiple growth factors), physical (surface topography and matrix stiffness) and mechanical (stretch) cues of stem cell niche have been utilized to dictate stem cell fates *in vitro*. Shapes and dimensions of nanotopography has demonstrated the capability of regulating stem cell fates.[4-7] Nanofibrous membrane has also been reported to promote the self-renewal of mouse embryonic stem cells (ESCs).[7] In addition, soft substrate promoted ESCs self-renewal while substrate having a stiffness

similar to bone induced osteogenic differentiation of mesenchymal stem (MSCs).[8-10] Moreover, there is ample evidence that mechanical stretch plays important roles in stem cells regulation.[11, 12] For example, 10% equibiaxial strain with frequency of 10 cycles/min promoted self-renewal of human ESCs.[12] Although the impact of various factors on stem cell fates has been acknowledged, the effect of mechanical stretch is complex and influenced by many factors such as strain rate and frequency, stretching and relaxation time. Importantly, previous studies on mechanical stretch regulation of stem cells generally based on stretch of flat and stiff substrates, which are non-physiologically relevant and have been indicated to promote osteogenesis while suppress adipogenesis and cell renewal.

We have previously investigated nanotopography and mechanical stretch modulation of cell behaviors in chapters 2 and 3. Here, we combined soft substrate and porous nanofibrous membrane that mimic *in vivo* microenvironment of bone marrow to study the regulation of cyclic mechanical stretch on renewal and differentiation of hMSCs, which have a great potential in regenerative medicine due to their multipotency, ability to secrete a cascade of immunomodulatory trophic factors, and reparative effects in clinical models,[13, 14] and thus have been widely applied in more than 500 registered clinical trials.[15] To achieved their therapeutic effect, an effective dose is in the range of 1–10 million MSC per kilogram.[2, 16] Biomanufacturing MSCs is still a challenge due to the decrease of stemness in the process of cell culture.[17, 18]

4.2 Materials and Methods

4.2.1 Fabrication and Characterization of Nanofibrous Membrane

Nanofibrous membranes were fabricated by electrospinning a solution of PCL in

1,1,1,3,3,3-hexafluoro-2-propanol (HFIP, 10%, w/v). Briefly, the PCL solution was loaded in a syringe with a blunt-tipped needle as the spinneret and connected to a syringe pump. A 4" x 4" square glass plate was placed on a 3" x 3" aluminum-covered plate as a collector, which was placed 16 cm below the needle tip. The needle tip was connected to a 14 kV voltage and the aluminum-covered plate was grounded. The PCL solution was ejected at a flow rate of 0.5 ml/hour, and the nanofibers were deposited on the collector.

The formed nanofibrous membranes were sputter-coated with gold using Denton Vacuum Desk V sputter coater (Denton Vacuum, Moorestown, NJ, USA) and imaged using a scanning electron microscope (SEM; TM3030 Plus, Hitachi High-Technologies Co., Tokyo, Japan). The fiber diameter and membrane pore size were analyzed using ImageJ (http://rsb.info.nih.gov/ij/index.html). For the fiber diameter, a line was drawn across the fiber, and then the length was measured. For the pore size, the images were adjusted using the threshold command, and the area of each pore was analyzed using the Analyze Particles function. A histogram line graph was then generated to show the distribution of fiber diameters or pore sizes.

4.2.2 Fabrication of the Bioengineered Stem Cell Niche

This device consisted of a bottom pneumatic layer (with a pneumatic chamber connected with stainless-steel tubing) with a thin PDMS membrane bonded on the top, a middle matrix layer (with a matrix chamber) with a nanofibrous membrane on the top and a top layer (with a cell culture chamber). All the parts except the nanofibrous membrane were made of PDMS (Sylgard 184, Dow Corning, Midland, MI, USA). All three layers were fabricated by casting a PDMS mixture of the resin and curing agent (10:1.05, w/w) on 3D printed molds and curing them on a hot plate at 75 $^{\circ}$ C for 2 hours. The thin PDMS

membrane was fabricated by spin-coating the PDMS mixture on a silicon wafer at 2500 rpm for 1 minute and curing it at 75 °C for 1 hour. The PDMS membrane was then permanently bonded on the bottom layer using the method we reported previously.[19] Briefly, the bottom layer with the opening facing down was stamped on a thin PDMS layer spin-coated on a silicon wafer for 30 seconds and transferred onto the PDMS membrane, followed by curing on a hot plate at 75 °C for 1 hour under a compressive pressure of approximately 1 MPa. Then the bottom layer with the membrane was gently peeled off from the silicon wafer. The middle matrix layer was bonded reversibly on the bottom layer with the PDMS membrane using the microtransfer assembly technique we developed previously.[19] Briefly, a PDMS mixture was dissolved in hexane (Thermo Fisher, Waltham, MA, USA. 1:2, v/v) and spin-coated on a silicon wafer at 4000 rpm for 2 minutes and prebaked at 50 ℃ for 5 min to form a thin adhesive film. Then, the middle layer was stamped on the adhesive film for 30 seconds and then transferred onto the bottom layer with the PDMS membrane, followed by at 75 °C for 1 hour under a compressive pressure of approximately 1 MPa. The soft matrix was made of sylgard 527 by mixing equal weights of part A and part B and adding it to the matrix chamber and curing it at 75 °C for 2 hours before attaching the nanofibrous membrane. The day before cell culture, the nanofibrous membrane was reversibly bonded to the top layer and oxygen plasma treated at medium power setting for 1 minute in a plasma cleaner (Model PDC-001, Harrick Plasma, Ithaca, NY, USA) followed by reversibly bonded to the middle layer. Phosphate buffered saline (PBS) was added to the top chamber to keep the fibrous membrane hydrophilic and the whole device was kept at 45 °C overnight.

4.2.3 Characterization of Mechanical Strain

The mechanical strain (deformation) of the PDMS membrane on the pneumatic chamber or the fibrous membrane on the interstitium layer when air was injected to the pneumatic chamber was characterized using a method that we previously described.[20] Briefly, the deformation of the PDMS membrane or the nanofibrous membrane was imaged using a charge-coupled device (CCD) camera (Model DMK 31; The Imaging Source, Charlotte, NC, USA). The captured images were adjusted using ImageJ to get a curvilinear profile, which was then digitalized using GetData Graph Digitalizer (http://www.getdata-graph-digitalizer.com). The measured linear strain was compared with the theoretical calculation as previously described.[20]

4.2.4 Cell Culture

The hMSCs were provided by Dr. Darwin Prockop at Texas A&M and used at passages 2 to 4. The cells were cultured in complete culture media (CCM) comprising α-minimum essential medium (α-MEM, Gibco, Grand Island, NY, USA) supplemented with 16.5% (v/v) fetal bovine serum (FBS; Atlanta Biologicals, Inc., Flowery Branch, GA, USA), 2 mM L-glutamine (Gibco), 100 U/ml penicillin and 100 μg/ml streptomycin (Gibco). The devices were sterilized in 70% (v/v) ethanol for 30 minutes and rinsed with PBS. The nanofibrous membrane was then coated with 50 μg/ml type I collagen (rat tail, Corning, Corning, NY, USA) in an incubator. The cells were seeded onto the nanofibrous membrane at a density of 5,000 cells/cm^2 (unless otherwise specified) and cultured in the incubator of 37 °C and 5% CO_2. The cells were cultured under static condition for 1 day before being subjected to the mechanical stretch. The cells were cultured in a multiwell plate as tissue culture polystyrene (TCPS) control.

4.2.5 Real-time Quantitative Reverse Transcription-polymerase Chain Reaction (qRT-PCR) Assay

Total RNA was extracted using Aurum Total RNA Mini Kit (Bio-Rad, Hercules, CA, USA) and cDNA was synthesized using iScript RT Supermix (Bio-Rad) according to the manufacturer's protocol. The concentration of total RNA and cDNA was measured using NanoDrop ND-1000 (NanoDrop Technologies, Wilmington, Delaware, USA). The mRNA expression was analyzed by qRT-PCR using CFX96 Touch Real-Time PCR Detection System (Bio-Rad). Primer sequences used were shown in Table 4.1. The mRNA expressions were normalized to TBP expression.

Table 4.1: Primers for qRT-PCR

Gene	Primer Sequence
NANOG	Forward: CTCCAACATCCTGAACCTCAGC Reverse: CGTCACACCATTGCTATTCTTCG
Oct4	Forward: CCTGAAGCAGAAGAGGATCACC Reverse: AAAGCGGCAGATGGTCGTTTGG
SOX2	Forward: GCTACAGCATGATGCAGGACCA Reverse: TCTGCGAGCTGGTCATGGAGTT
CD106	Forward: GATTCTGTGCCCACAGTAAGGC Reverse: TGGTCACAGAGCCACCTTCTTG
CD146	Forward: ATCGCTGCTGAGTGAACCACAG Reverse: CTACTCTCTGCCTCACAGGTCA
CD271	Forward: CCTCATCCCTGTCTATTGCTCC Reverse: GTTGGCTCCTTGCTTGTTCTGC
RUNX2	Forward: CCCAGTATGAGAGTAGGTGTCC Reverse: GGGTAAGACTGGTCATAGGACC
PPARγ	Forward: AGCCTGCGAAAGCCTTTTGGTG Reverse: GGCTTCACATTCAGCAAACCTGG
TBP	Forward: TGTATCCACAGTGAATCTTGGTTG Reverse: GGTTCGTGGCTCTCTTATCCTC

4.2.6 Cell Proliferation

The cell proliferation was examined using MTT assay (Life Technologies, US).

After cultured for the predetermined day, culture medium was removed and then 200 µl of fresh medium and 20 µl of 12 mM MTT stock solution was added in each device. Meanwhile, 20 µl of the MTT stock solution was added to 200 µl of fresh medium alone as negative control. The devices were then incubated for 4 hours at 37 °C. Subsequently, the medium was removed and 100 µl of DMSO was added to each device and mixed thoroughly with the pipette. The devices were incubated at 37 °C for 10 minutes and the absorbance was measured at 540 nm in a Cytation 5 Cell Imaging Multi-Mode Reader (BioTek, Winooski, VT, US).

4.2.7 Staining of BCIP/NBT and Oil Red O

The cells were cultured in CCM for 24 hours and then cultured in either osteogenic differentiation media (CCM supplemented with 1 nM dexamethasone (Sigma Aldrich, St Louis, MO, USA), 10 mM β-glycerolphosphate (Sigma Aldrich) and 50 µM L-ascorbic acid 2-phosphate (Sigma Aldrich)) or adipogenic differentiation media (CCM supplemented with 0.5 µM dexamethasone, 0.5 µM isobutylmethylxanthine (Sigma Aldrich) and 50 µM indomethacin (Sigma Aldrich)) for 14 days and the medium was changed every 3 to 4 days. After 14 days, the cells were fixed with 4% paraformaldehyde (PFA; Sigma-Aldrich) for 1 hour and then stained with fast 5-bromo-4-chloro-3-indolyl phosphate and nitroblue tetrazolium (BCIP/NBT, VWR international, Radnor, USA) for ALP for osteogenic differentiation or Oil red O (Sigma-Aldrich) for adipogenic differentiation. The Oil red O was dissolved in isopropanol (0.5%, w/v) and then freshly diluted in PBS (60%, v/v) prior to each staining. Staining for 30 minutes at room temperature and then rinse with deionized water (for BCIP/NBT staining) or PBS (for Oil red O staining) until the

background is clear. Images were taken using a Keyence BZ-X810 fluorescence microscope (Keyence, Osaka, Japan).

4.2.8 Immunofluorescence Staining

After being cultured for predetermined day, the cells were fixed with 4% PFA solution for 20 minutes at room temperature and blocked in PBST solution (PBS supplemented with 0.2% (v/v) Triton X-100) containing 0.03 g/mL bovine serum albumin (BSA, Sigma-Aldrich) and 0.1% (v/v) goat serum (Sigma-Aldrich) for 1 hour at room temperature. The samples were then incubated with primary antibody at 4 °C overnight followed by incubated with secondary antibody at room temperature for 1 hour. The antibodies used were listed in Table 4.2. F-actin was stained using Alexa Fluor 488 phalloidin (Life Technologies, Carlsbad, CA, USA. 1:200 in PBS) for 2 hours at room temperature. After secondary antibody or phalloidin incubation, the samples were mounted with ProLong™ Gold Antifade Reagent with 4,6-diamidino-2-phenylindole (DAPI, Life Technologies), and images were obtained using a Nikon Ti eclipse fluorescence microscope (Nikon, Melville, NY, USA).

Table 4.2: Antibodies for immunofluorescence staining

Antibody	Vendor	Catalog #	Dilution
Paxillin	Abcam	ab32084	1:150
FAK	Santa Cruz	sc-932	1:200
pFAK	Santa Cruz	sc-81493	1:200
YAP	Santa Cruz	sc-101199	1:200

4.2.9 Image Analysis

Cell spreading area, nuclei area, paxillin size, fluorescence intensity and YAP nucleus-to-cytoplasm (N/C) intensity ratio were analyzed using ImageJ. The paxillin size

was quantified as previously described.[21] The YAP N/C ratio was analyzed according to the previous report.[22] Briefly, the cell nuclei were outlined using “analyze particle” tool. The overall fluorescence intensity of the cell, and the intensity of nuclear area were analyzed separately and thus the N/C ratio was calculated.

4.2.10 Statistical Analysis

The data were presented as mean ± standard error of the mean (S.E.M.). The statistical differences were analyzed using two-tailed *t* test using Prism 8 (GraphPad software, San Diego, CA, USA). Statistically significant differences were considered at a level of $p < 0.05$.

4.3 Results and Discussion

4.3.1 Fabrication and Characterization of Nanofibrous Membrane

The SEM image of the nanofibrous membrane was displayed in Figure 4.1**.** The nanofibrous membrane had an average pore size of 21 ± 4 μm^2 and the average diameter of the nanofibers was 792 ± 187 nm.

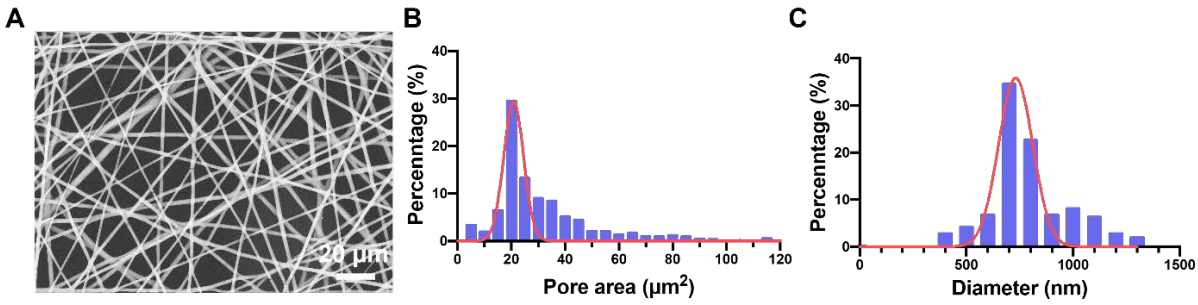

Figure 4.1: Characterization of the nanofibrous membrane. (A) SEM image of the nanofibrous membrane. (B) Pore size and (C) Diameter of the nanofibrous membrane.

4.3.2 Fabrication and Characterization of the Bioengineered Stem Cell Niche

From bottom to top, this device has a pneumatic chamber, thin PDMS membrane,

cell culture matrix with soft substrate and nanofibrous membrane, and a chamber for cell culture medium (Figure 4.2). When air was infused in and withdrawn from the pneumatic chamber, the PDMS membrane moved up and down and this deformation was transmitted to the soft matrix and the top nanofibrous membrane, which resulted in a stretch to the adherent cells. When air was infused into the pneumatic chamber, there was no significant difference between the strain of the nanofibrous membrane and that of the PDMS membrane (Figure 4.2C), which indicated that the mechanical stretch was transmitted through the soft matrix to the nanofibrous membrane.

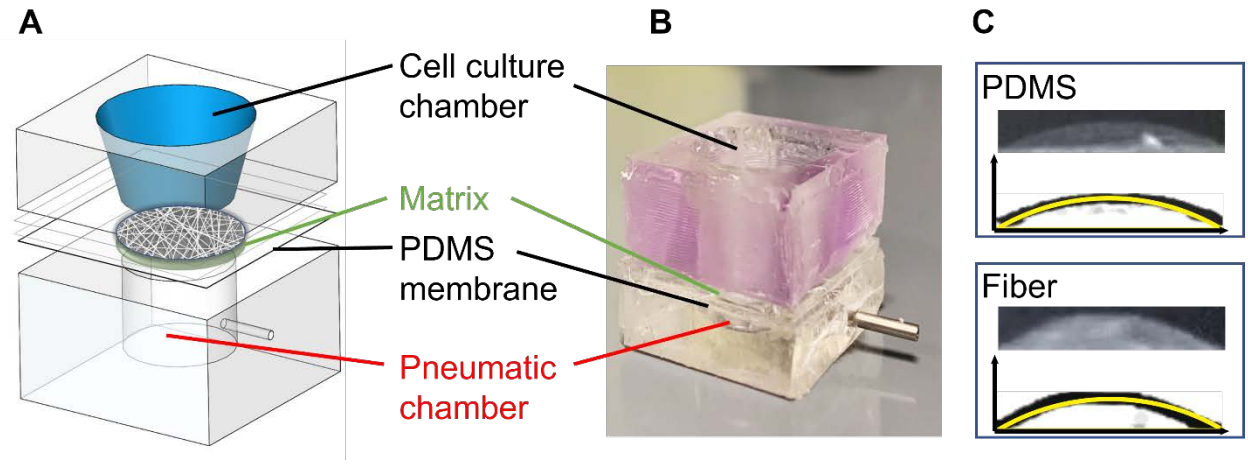

Figure 4.2: Characterization of the bioengineered stem cell niche. (A) Design and (B) Photo of the device. (C) Characterization of the mechanical strain. Original CCD images and the profiles (black curve) of the deformed PDMS membrane or nanofibrous membrane under a theoretical strain of 5% (yellow curve).

Although there are still inconsistencies, reports shown that mechanical stretch can promote cell proliferation and relatively higher magnitude and frequency stretch tend to initiate and promote stem cell osteogenic differentiation.[11, 23, 24] The mechanical stretch effects are also time-dependent. For example, a decrease of proliferation occurs after long-term exposure to mechanical stretch following the initial increase.[25, 26] Incorporation of rest periods has been reported to be an effective way to avoid the long-

term decline in stretch effect, which can extend it from hours to 7 days.[27, 28] In this study, to help hMSC expansion for long-term culture, relatively low magnitude and frequency mechanical stretch was applied at 5% linear strain and a frequency of 0.1 Hz, and a relaxation of 50 seconds for every 50 seconds stretch was applied in the mechanical stretch device. In addition to mechanical stretch, tissue stiffness plays a critical role in the maintenance of the normal function of cells, tissues and organs and it has been reported that the MSC fate can be tuned by substrate stiffness.[9, 29] To mimic the stiffness of bone marrow *in vivo*, which was reported from 0.25–24.7 kPa, Sylgard 527 (1.5 kPa) was filled in the matrix chamber beneath the nanofibrous membrane.[30, 31]

4.3.3 Regulation of Cell Renewal and Stemness by Mechanical Stretch

After being cultured for 7 days, the expression levels of stemness-related genes NANOG, SOX2, CD106 of hMSCs cultured under mechanical stretch were higher than that of the cells cultured under static condition and TCPS control, and Oct 4 expression increased under mechanical stretch compared to TCPS, although the cell viability was higher under TCPS control (Figure 4.3A, B). Moreover, the gene expressions of cells before seeding into the stem cells niche or TCPS control (day 0) were also detected as indicated with the dash line in Figure 4.3B. The expression of these genes under mechanical stretch were higher or equal to that of day 0, indicating that the engineered stem cell niche can help maintain stemness of hMSCs. After 14 days, the cells showed higher viability under mechanical stretch and the expression of NANOG was still significantly higher under stretch compared to static control (Figure 4.3C, D). The increased cell viability and stemness-related gene expressions of cells cultured under

mechanical stretch indicated that the mechanical stretch in the bioengineered stem cell niche promoted self-renewal while preserving the stemness of hMSCs. Of note, the cells exhibited 3-fold increase of viability while keeping the higher NANOG expression after cultured for 2 weeks under mechanical stretch, indicating the potential application of the device for long-term and large-scale expansion of stem cells *in vitro*.

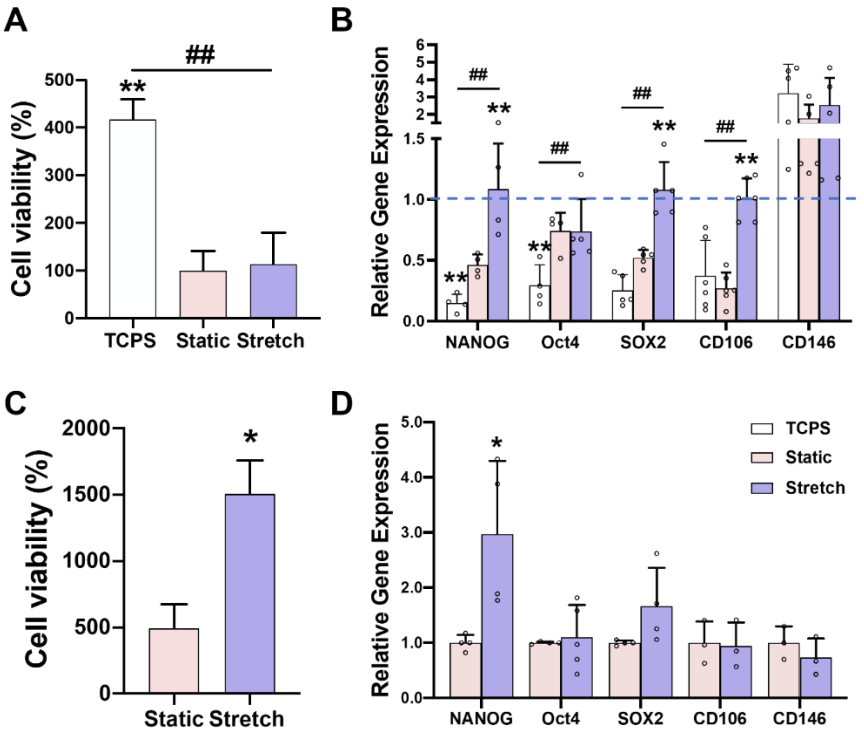

Figure 4.3: Regulation of cell renewal by mechanical stretch. Cell viability of hMSCs cultured for (A) 7 days and (C) 14 days. The expression levels of stemness-related genes of hMSCs cultured for (B) 7 days and (D) 14 days. The dash line indicated the gene expression level of cells at day 0. *p < 0.05, **: p < 0.01 compared to static control. $^{\#}$: p < 0.05, $^{\#\#}$: p < 0.01 between groups.

4.3.4 Regulation of Cell Differentiation by Mechanical Stretch

The quantification of gene expression levels of peroxisome proliferator-activated receptor gamma (PPARγ) and runt-related transcription factor 2 (RUNX2) were determined using qRT-PCR. The upregulation of PPARγ and downregulation of RUNX2 under mechanical stretch (Figure 4.4A, B) indicated that the mechanical stretch promoted

adipogenic differentiation while inhibiting osteogenic differentiation of hMSCs. The detection of lipid droplets by Oil Red O staining showed that the adipogenic differentiation was increased by mechanical stretch, while the ALP staining showed that after being cultured in osteogenic differentiation media for 14 days under mechanical stretch, the osteogenic differentiation of hMSCs was decreased compared to static condition (Figure 4.4C). Besides maintaining stem cell renewal and stemness, another aim of *in vitro* stem cell culture is to direct the differentiation into a specific cell lineage. Different from previous reports that mechanical stretch typically promotes osteogenic differentiation, the combination of controlled mechanical stretch, soft matrix, and nanofibrous structure in our device can promote adipogenic differentiation while inhibiting osteogenic differentiation of hMSCs.[23, 26]

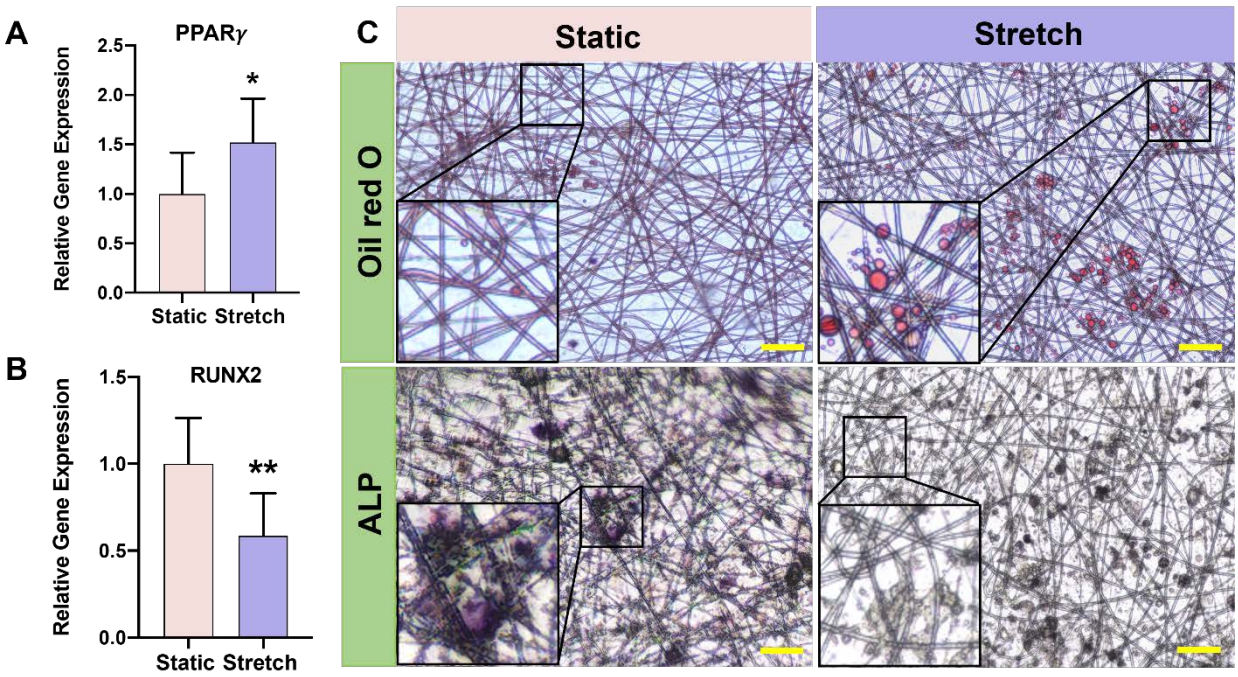

Figure 4.4: Regulation of cell differentiation by mechanical stretch. (A) PPARγ expression of hMSCs cultured in adipogenic differentiation media for 14 days. (B) RUNX2 expression of hMSCs cultured in osteogenic differentiation media for 14 days. (C) Oil red O staining of hMSCs cultured in adipogenic differentiation media or ALP staining of hMSCs cultured in osteogenic differentiation media for 14 days. Enlarged images shown in the lower left corners. Scale bars: 50 μm. (C) *p < 0.05, **: p < 0.01 compared to static control.

4.3.5 Regulation of Cell Spreading by Mechanical Stretch

The immunofluorescence staining showed the morphology of hMSCs cultured in the device with or without application of mechanical stretch (Figure 4.5A). The hMSCs under static condition appeared polarization morphology, and the orientation of filopodia was random, which was in accord with the randomly aligned electrospun PCL nanofibers.

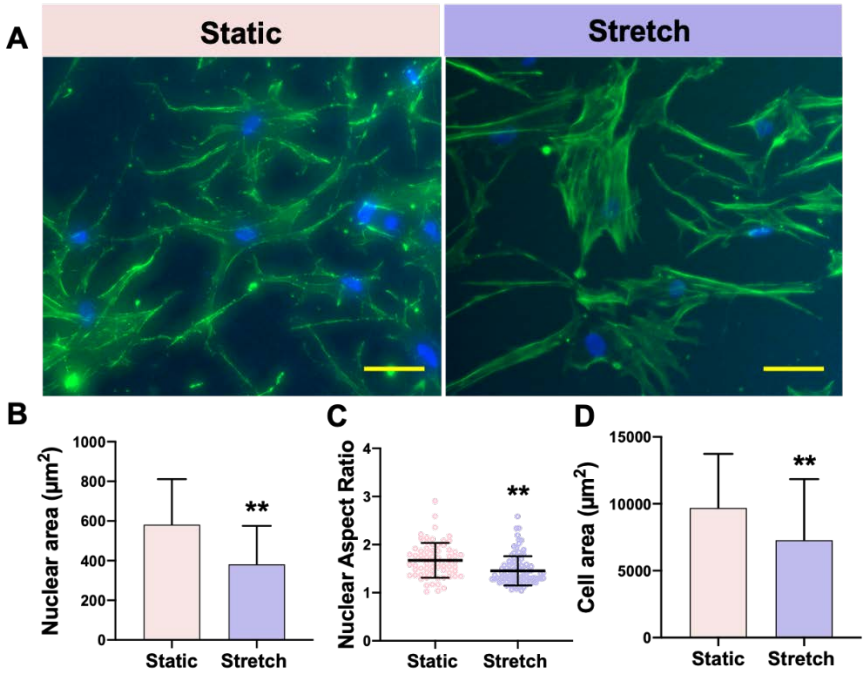

Figure 4.5: Regulation of cell spreading by mechanical stretch. (A) Representative immunofluorescent images of hMSCs cultured for 7 days under static condition or mechanical stretch. Green, F-actin; blue, nuclei. Scale bars: 100 μm. (B) Cell nuclear area. (C) Nuclear aspect ratio. (D) Cell area. n=70-100.

Conversely, under mechanical stretch, the cells were nonpolarized and cell edges were relatively smooth as those cultured on TCPS. Moreover, the cell nuclear area (Figure 4.5B), cell nuclear aspect ratio (Figure 4.5C), and cell area (Figure 4.5D) showed a significant decrease under mechanical stretch. The hMSCs were preferentially spreading along the orientation of random electrospun PCL nanofibers, thus resulting in the appearance of cell polarization and filopodia, which confine the proliferation of hMSCs compared to cells on flat substrate. It has been reported that force isotropy helps maintain

pluripotency of stem cell, induce stem cell renewal, and affect cell morphology.[32] Here, the mechanical stretch was isotropic, which increased the cell number of hMSCs while maintaining stemness, and decreased the osteogenic differentiation potential.

4.3.6 Regulation of Mechanical Sensing by Mechanical Stretch

To understand the mechanism of how mechanical stretch maintains cell stemness and controls differentiation of hMSCs. We further explored mechanosensing and mechanotransduction of cells in the devices. The mechanical properties of the substrate can be sensed by focal adhesions and the mechanical signals are transmitted through the actin cytoskeleton and induce intracellular biochemical signals.[33] Thus, we investigated the expression of focal adhesion protein paxillin, cytoskeleton F-actin, nuclear F-actin, relative gene expression of mechanosensitive ion channel protein piezo1, and localization of Yes-associated protein (YAP).

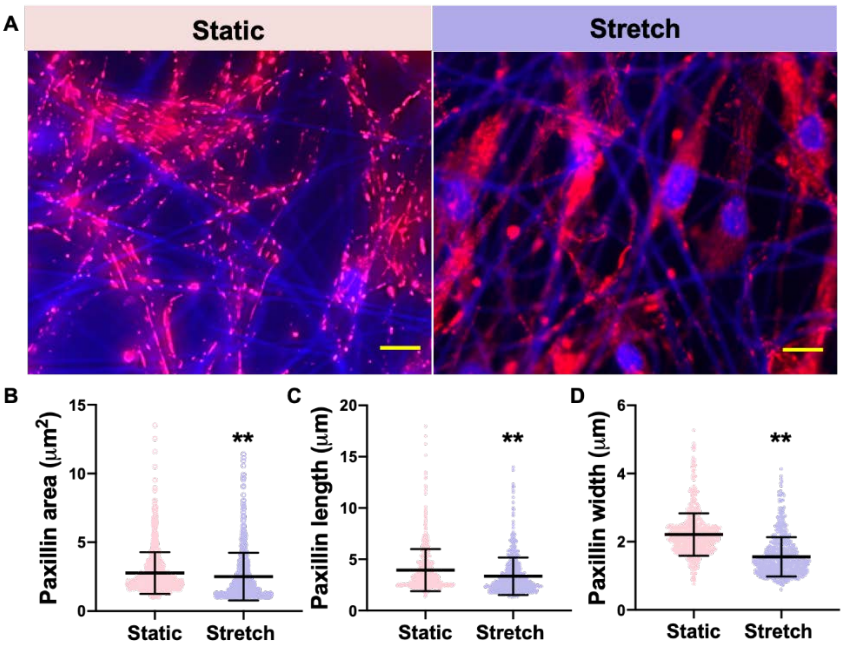

Figure 4.6: Regulation of cell adhesion by mechanical stretch. (A) Representative immunofluorescent images of hMSCs cultured for 7 days under static condition or mechanical stretch. Red, paxillin; blue, nuclei. Scale bars: 50 μm. (B) Paxillin area. (C) Paxillin length. (D) Paxillin width. n=100-200.

Mature focal adhesion protein paxillin was observed along the nanofibers under static condition. In contrast, less mature paxillin was observed under mechanical stretch and paxillin was diffused and localized in the peri-nuclear regions (Figure 4.6A). Although there was no significant difference in the fluorescence intensity, the paxillin area, length, and width were decreased under mechanical stretch (Figure 4.6B, C, D).

In this study, the *in vivo* like nanofibrous structure supported cell adhesion and the mature paxillin anchored the cells to the nanofibers to maintain cell tension.[34] While under mechanical stretch, immature paxillin diffused in the peri-nuclear area, indicated the decrease of cell tension, which can help maintain the stemness, prefer adipogenic differentiation and inhibit osteogenic differentiation of MSCs.[35]

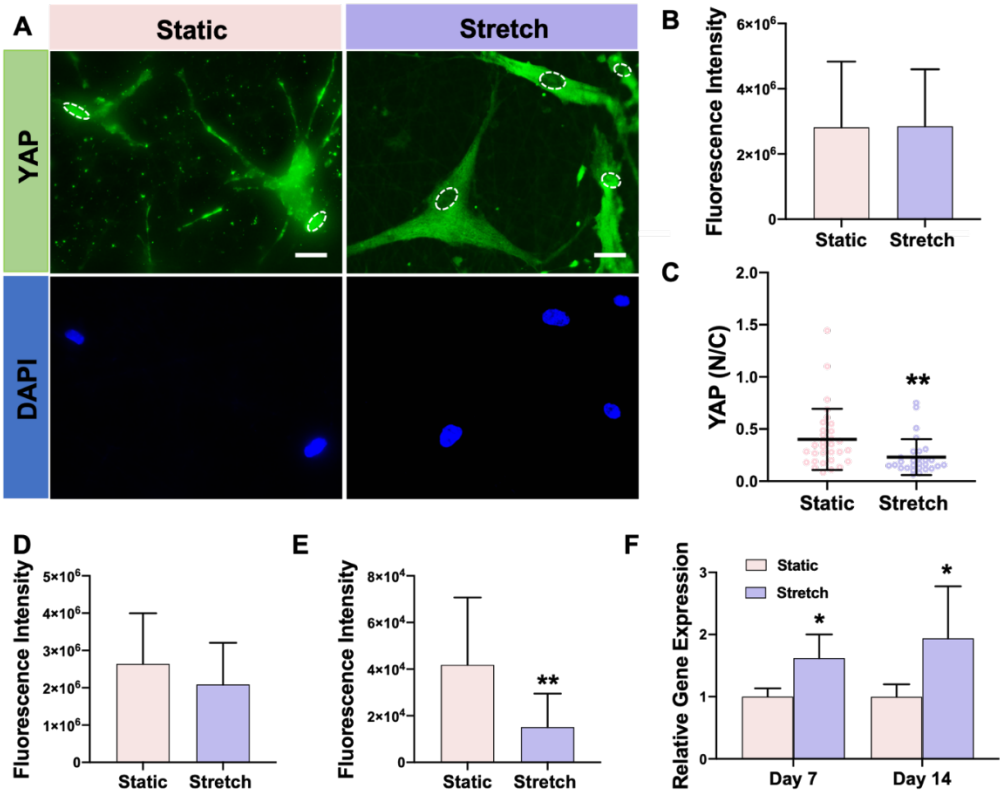

Figure 4.7: Regulation of cell mechanical sensing by mechanical stretch. (A) Representative immunofluorescent images of YAP (green) with DAPI labeled nuclei (blue) of hMSCs cultured for 7 days. Scale bars: 50μm. (B) Fluorescence intensity and (C) N/C ratio of YAP. n=30-40. Fluorescence intensity of (D) F-actin and (E) nuclear F-actin. (F) Relative gene expression of Piezo1.

The cytoplasmic localization of Yes-associated protein (YAP) was increased under mechanical stretch, although the total expression was not changed. Although there was no difference for F-actin expression, the F-actin in nucleus region was decreased under mechanical stretch. The gene expression of mechanosensitive ion channel protein piezo1 was increased under mechanical stretch (Figure 4.7).

The mechanical stimuli can be transduced from focal adhesion zones in the plasma membrane through filamentous actin network to the Linker of Nucleoskeleton and Cytoskeleton (LINC) complexes in the nuclear membrane and induce intracellular biochemical signals. Meanwhile, piezo1 can sense mechanical stretch and be activated by tension in lipid bilayer and cytoskeletal tension, converting mechanical signals into biochemical signals and regulating transcriptional activities such as YAP activity.[36, 37] Meanwhile, Forces transmitted from the cell surface to the nucleus by the cytoskeleton and the stretching of the nuclear pores influence YAP localization. The enlarged nuclear pores allow the transport of the mechano-transducers YAP and other transcription factors between the cell nucleus and cytoplasm.[38, 39] In this study, the increase of adipogenic differentiation and decrease of osteogenic differentiation of MSCs under mechanical stretch may resulted from the decrease of cell adhesion and cell tension, which are consistent with reports that tension force generated by cell spreading can promote osteogenic differentiation, whereas the decreased cell tension enhance adipogenic differentiation.[40, 41] Interestingly, the F-actin in nucleus region was decreased under mechanical stretch, which may be the mechanism responsible for the increased cell renewal, which was consistent with previous report that low nuclear actin levels promote cell stemness.[42]

4.4 Conclusion

The bioengineered stem cell niche combined soft substrate and porous nanofibrous membrane that mimics *in vivo* microenvironment of bone marrow. The cyclic mechanical stretch applied to this platform promoted cell renewal and regulated differentiation of hMSCs. This offered insights that mechanical stretch is a strategy for promoting renewal and controlling differentiation of hMSCs for clinical applications. This study combined with our previous studies provided guidelines and implications for developing complex *in vitro* biomimetic cell culture models such as lung alveolus chips.

4.5 References

[1] K.G. Chen, B.S. Mallon, R.D.G. McKay, P.G. Robey, Human Pluripotent Stem Cell Culture: Considerations for Maintenance, Expansion, and Therapeutics, Cell Stem Cell 14(1) (2014) 13-26.

[2] A. Aijaz, M. Li, D. Smith, D. Khong, C. LeBlon, O.S. Fenton, R.M. Olabisi, S. Libutti, J. Tischfield, M.V. Maus, R. Deans, R.N. Barcia, D.G. Anderson, J. Ritz, R. Preti, B. Parekkadan, Biomanufacturing for clinically advanced cell therapies, Nat Biomed Eng 2(6) (2018) 362-376.

[3] R.E. Hynds, A. Giangreco, Concise review: the relevance of human stem cell-derived organoid models for epithelial translational medicine, Stem cells 31(3) (2013) 417-422.

[4] M.J. Dalby, N. Gadegaard, R.O.C. Oreffo, Harnessing nanotopography and integrin–matrix interactions to influence stem cell fate, Nature materials 13(6) (2014) 558-569.

[5] S. Ankam, M. Suryana, L.Y. Chan, A.A.K. Moe, B.K.K. Teo, J.B.K. Law, M.P. Sheetz, H.Y. Low, E.K.F. Yim, Substrate topography and size determine the fate of human embryonic stem cells to neuronal or glial lineage, Acta biomaterialia 9(1) (2013) 4535-4545.

[6] Y. Yang, K. Wang, X. Gu, K.W. Leong, Biophysical regulation of cell behavior—cross talk between substrate stiffness and nanotopography, Engineering 3(1) (2017) 36-54.

[7] X.Z. Yan, J.J. Van Den Beucken, S.K. Both, P.S. Yang, J.A. Jansen, F. Yang, Biomaterial strategies for stem cell maintenance during in vitro expansion, Tissue Engineering Part B: Reviews 20(4) (2014) 340-354.

[8] F. Chowdhury, Y. Li, Y.C. Poh, T. Yokohama-Tamaki, N. Wang, T.S. Tanaka, Soft substrates promote homogeneous self-renewal of embryonic stem cells via downregulating cell-matrix tractions, PloS one 5(12) (2010) e15655.

[9] Y.K. Wang, C.S. Chen, Cell adhesion and mechanical stimulation in the regulation of mesenchymal stem cell differentiation, Journal of cellular and molecular medicine 17(7) (2013) 823-832.

[10] J.S. Park, J.S. Chu, A.D. Tsou, R. Diop, Z. Tang, A. Wang, S. Li, The effect of matrix stiffness on the differentiation of mesenchymal stem cells in response to TGF-β, Biomaterials 32(16) (2011) 3921-3930.

[11] S. Ghazanfari, M. Tafazzoli-Shadpour, M.A. Shokrgozar, Effects of cyclic stretch on proliferation of mesenchymal stem cells and their differentiation to smooth muscle cells, Biochemical and biophysical research communications 388(3) (2009) 601-605.

[12] S. Saha, L. Ji, J.J. de Pablo, S.P. Palecek, Inhibition of human embryonic stem cell differentiation by mechanical strain, Journal of cellular physiology 206(1) (2006) 126-137.

[13] A.A. Abdeen, K. Saha, Manufacturing Cell Therapies Using Engineered Biomaterials, Trends Biotechnol 35(10) (2017) 971-982.

[14] A. Trounson, C. McDonald, Stem Cell Therapies in Clinical Trials: Progress and Challenges, Cell Stem Cell 17(1) (2015) 11-22.

[15] B. Varitsara, W. Haoyu, Z. Shufang, O. Hongwei, From “Bench to Bedside”: Current Advancement on Large-Scale Production of Mesenchymal Stem Cells, Stem Cells Dev 26(22) (2017) 1662-1673.

[16] N.J. Dwarshuis, K. Parratt, A. Santiago-Miranda, K. Roy, Cells as advanced therapeutics: State-of-the-art, challenges, and opportunities in large scale biomanufacturing of high-quality cells for adoptive immunotherapies, Adv Drug Deliver Rev 114 (2017) 222-239.

[17] J.S. Heo, Y. Choi, H.-S. Kim, H.O. Kim, Comparison of molecular profiles of human mesenchymal stem cells derived from bone marrow, umbilical cord blood, placenta and adipose tissue, International journal of molecular medicine 37(1) (2016) 115-125.

[18] C. Zhao, K. Lin, X. Wang, Maintenance and modulation of stem cells stemness based on biomaterial designing via chemical and physical signals, Applied Materials Today 19 (2020) 100614.

[19] Y. Yang, K. Kulangara, J. Sia, L. Wang, K.W. Leong, Engineering of a microfluidic cell culture platform embedded with nanoscale features, Lab on a Chip 11(9) (2011) 1638-1646.

[20] K. Man, J. Liu, K.M. Phan, K. Wang, J.Y. Lee, X. Sun, M. Story, D. Saha, J. Liao, H. Sadat, Dimensionality-Dependent Mechanical Stretch Regulation of Cell Behavior, ACS Applied Materials & Interfaces 14(15) (2022) 17081-17092.

[21] U. Horzum, B. Ozdil, D. Pesen-Okvur, Step-by-step quantitative analysis of focal adhesions, MethodsX 1 (2014) 56-59.

[22] B.D. Cosgrove, K.L. Mui, T.P. Driscoll, S.R. Caliari, K.D. Mehta, R.K. Assoian, J.A. Burdick, R.L. Mauck, N-cadherin adhesive interactions modulate matrix mechanosensing and fate commitment of mesenchymal stem cells, Nature materials 15(12) (2016) 1297-1306.

[23] X. Chen, J. Yan, F. He, D. Zhong, H. Yang, M. Pei, Z.P. Luo, Mechanical stretch induces antioxidant responses and osteogenic differentiation in human mesenchymal stem cells through activation of the AMPK-SIRT1 signaling pathway, Free Radical Biology and Medicine 126 (2018) 187-201.

[24] J.-M. Lee, M.-G. Kim, J.-H. Byun, G.-C. Kim, J.-H. Ro, D.-S. Hwang, B.-B. Choi, G.-C. Park, U.-K. Kim, The effect of biomechanical stimulation on osteoblast differentiation of human jaw periosteum-derived stem cells, Maxillofacial plastic and reconstructive surgery 39(1) (2017) 1-9.

[25] G. Song, Y. Ju, H. Soyama, T. Ohashi, M. Sato, Regulation of cyclic longitudinal mechanical stretch on proliferation of human bone marrow mesenchymal stem cells, Molecular and Cellular Biomechanics 4(4) (2007) 201.

[26] C.H. Huang, M.H. Chen, T.H. Young, J.H. Jeng, Y.J. Chen, Interactive effects of mechanical stretching and extracellular matrix proteins on initiating osteogenic differentiation of human mesenchymal stem cells, Journal of cellular biochemistry 108(6) (2009) 1263-1273.

[27] B.D. Riehl, J.H. Park, I.K. Kwon, J.Y. Lim, Mechanical stretching for tissue engineering: two-dimensional and three-dimensional constructs, Tissue Engineering Part B: Reviews 18(4) (2012) 288-300.

[28] Y. Wu, X. Zhang, P. Zhang, B. Fang, L. Jiang, Intermittent traction stretch promotes the osteoblastic differentiation of bone mesenchymal stem cells by the ERK1/2-activated Cbfa1 pathway, Connective tissue research 53(6) (2012) 451-459.

[29] W. Wan, B. Cheng, C. Zhang, Y. Ma, A. Li, F. Xu, M. Lin, Synergistic effect of matrix stiffness and inflammatory factors on osteogenic differentiation of MSC, Biophysical journal 117(1) (2019) 129-142.

[30] L.E. Jansen, N.P. Birch, J.D. Schiffman, A.J. Crosby, S.R. Peyton, Mechanics of intact bone marrow, Journal of the mechanical behavior of biomedical materials 50 (2015) 299-307.

[31] C. Moraes, J.M. Labuz, Y. Shao, J. Fu, S. Takayama, Supersoft lithography: candy-based fabrication of soft silicone microstructures, Lab on a Chip 15(18) (2015) 3760-3765.

[32] M.M. Nava, M.T. Raimondi, R. Pietrabissa, Controlling self-renewal and differentiation of stem cells via mechanical cues, Journal of Biomedicine and Biotechnology 2012 (2012).

[33] Y. Hou, W. Xie, L. Yu, L.C. Camacho, C. Nie, M. Zhang, R. Haag, Q. Wei, Surface roughness gradients reveal topography-specific mechanosensitive responses in human mesenchymal stem cells, Small 16(10) (2020) 1905422.

[34] S.R. Coyer, A. Singh, D.W. Dumbauld, D.A. Calderwood, S.W. Craig, E. Delamarche, A.J. García, Nanopatterning reveals an ECM area threshold for focal adhesion assembly and force transmission that is regulated by integrin activation and cytoskeleton tension, Journal of cell science 125(21) (2012) 5110-5123.

[35] Y. Hou, L. Yu, W. Xie, L.C. Camacho, M. Zhang, Z. Chu, Q. Wei, R. Haag, Surface roughness and substrate stiffness synergize to drive cellular mechanoresponse, Nano letters 20(1) (2019) 748-757.

[36] L. He, G. Si, J. Huang, A.D. Samuel, N. Perrimon, Mechanical regulation of stem-cell differentiation by the stretch-activated Piezo channel, Nature 555(7694) (2018) 103-106.

[37] J.L. Nourse, M.M. Pathak, How cells channel their stress: Interplay between Piezo1 and the cytoskeleton, Seminars in cell & developmental biology, Elsevier, 2017, pp. 3-12.

[38] A. Tajik, Y. Zhang, F. Wei, J. Sun, Q. Jia, W. Zhou, R. Singh, N. Khanna, A.S. Belmont, N. Wang, Transcription upregulation via force-induced direct stretching of chromatin, Nature materials 15(12) (2016) 1287-1296.

[39] A. Remuzzi, B. Bonandrini, M. Tironi, L. Longaretti, M. Figliuzzi, S. Conti, T. Zandrini, R. Osellame, G. Cerullo, M.T. Raimondi, Effect of the 3D artificial nichoid on the morphology and mechanobiological response of mesenchymal stem cells cultured in vitro, Cells 9(8) (2020) 1873.

[40] Y.A. Miroshnikova, S.A. Wickström, Mechanical forces in nuclear organization, Cold Spring Harbor Perspectives in Biology 14(1) (2022) a039685.

[41] Y.L. Fan, H.C. Zhao, B. Li, Z.L. Zhao, X.Q. Feng, Mechanical roles of F-actin in the differentiation of stem cells: a review, ACS Biomaterials Science & Engineering 5(8) (2019) 3788-3801.

[42] G. Brusatin, T. Panciera, A. Gandin, A. Citron, S. Piccolo, Biomaterials and engineered microenvironments to control YAP/TAZ-dependent cell behaviour, Nature materials 17(12) (2018) 1063-1075.

CHAPTER 5

BIOENGINEERING OF HUMAN LUNG INTERSTITIUM CHIP*

5.1 Introduction

Being responsible for the exchange of oxygen and carbon dioxide, the alveoli, tiny air sacs in human lungs, also serve as the entry gateway for airborne particles such as engineered nanomaterials, air pollutants, and pathogens to enter the human body, while providing a route for pulmonary drug delivery. In particular, engineered nanomaterials, especially when in their aerosolized form, can be inhaled into lungs causing significant public health problems.[1] It has been shown that inhaled carbon nanotubes (CNTs), a major class of engineered nanomaterials,[2] cross the alveolar epithelial barrier and enter the interstitium, inducing progressive interstitial lung fibrosis in mice in weeks.[3] In addition to negative health implications, researchers seek to leverage the large alveolar surface area for inhalation-based delivery of drug-loaded nanoparticles, a cutting-edge technology for lung cancer therapy.[4] Thus, pathophysiologically relevant preclinical alveolus models are critical for understanding and treatment of lung diseases and toxicity assessment of engineered nanomaterials.

Current preclinical models (*e.g.*, animal models, conventional 2D models, and lung organoids) have limitations. Differences in the anatomy, physiology, and genomics between animals and humans make conventional animal models inconsistent and inaccurate, limiting their translation to clinical studies.[5] In 2D models, human primary cells or cell lines are cultured on flat plastic surfaces, which leads to different behavior

* This entire chapter is reproduced from Man, Kun, Jiafeng Liu, Cindy Liang, Christopher Corona, Michael D. Story, Brian Meckes, and Yong Yang. "Biomimetic human lung alveolar interstitium chip with extended longevity." *bioRxiv* (2022): 2022-12. DOI: 10.1101/2022.12.23.521822. Originally published under CC-BY license; authors retain copyright.

compared to their *in vivo* counterparts and replication of *in vivo* phenotypes or functions observed in native tissues.[6] Lung organoids replicate complex 3D structures and functions of the lung but cannot model some key *in vivo* lung microenvironment features like the air-liquid interface (ALI).[7, 8] Moreover, all these models lack physiologically relevant mechanical characteristics, such as interstitial flow and/or lung breathing movement. Organ-on-a-chip systems can replicate organismal level function and have recently attracted great attention.[9, 10] Particularly, the human lung chips model the ALI and alveolus-capillary interface, mimic breath movement,[9] and have been adapted to model several diseases and test therapeutic drugs.[11, 12] Several human lung fibrosis chips have also been developed to replicate stromal-vascular and stromal-epithelial interfaces.[13, 14] However, these chips do not mimic the basement membrane, interstitium stiffness, or breathing movement critical for lung functions and disease.[15, 16] Due to the missing key alveolar microenvironmental features, the epithelial barrier function is not sustained and these chips are usually only viable for several week;[9, 11, 17, 18] therefore, they are not suitable for investigation of chronic diseases.

We previously investigated the nanotopography and mechanical stretch modulation of cell behaviors in chapter 2 and chapter 3, and the results revealed that porous nanofibrous structure and mechanical stretch dimensionality (*i.e.*, 3D stretch similar to native alveoli) is critical to epithelium formation and homeostasis.[19] Moreover, we cultured hMSC in a bioengineered stem cell niche combined soft substrate, porous nanofibrous membrane and 3D mechanical stretch (chapter 4). After cultured for 14 days, the hMSC proliferation increased while pluripotency was still maintained. This study using

hMSCs as the model cells further implied that these physical and mechanical cues could facilitate epithelium homeostasis synergistically.

In this study, we developed a human alveolar interstitium chip that consists of an electrospun nanofibrous membrane for co-culture of alveolar epithelial cells and lung fibroblasts encapsulated in 3D collagenous hydrogels. The pore size of the nanofibrous membrane was optimized to promote the epithelium formation. The chip also provided interstitial flow and 3D mechanical stretch of physiological relevance to the cells. The interstitium chip exhibited enhanced epithelium barrier function and extended longevity beyond eight weeks. Furthermore, the penetration of multi-walled CNTs (MWCNTs) across the epithelium on the chips showed results consistent with *in vivo* study.

5.2 Materials and Methods

5.2.1 Cell Culture

Human alveolar epithelial cells (A549; Cat#: CCL-185, ATCC, Manassas, VA, USA) were cultured in Dulbecco's Modified Eagle Medium (DMEM) with L-glutamine (Life Technologies, Carlsbad, CA, USA) supplemented with 10% fetal bovine serum (FBS; Sigma-Aldrich, St Louis, MO, USA), 100 U/ml penicillin and 100 μg/ml streptomycin (Life Technologies). Normal human lung fibroblasts (NHLFs; Cat#: CC-2512, Lonza, Walkersville, MD, USA) were cultured in fibroblast basal medium (Lonza) supplemented with FGM-2 SingleQuots supplements (Lonza), 100 U/ml penicillin, and 100 μg/ml streptomycin.

5.2.2 Fabrication of Lung Interstitium Chip

The chip consisted of an upper air chamber, a middle interstitium chamber, and a lower pneumatic chamber (Figure 5.1), which had a concentric circle of 10 mm in diameter

and different heights of 10, 2, and 5 mm, respectively. All the chambers were prepared by casting a mixture of polydimethylsiloxane (PDMS) resin and curing agent at a w/w ratio of 10:1.05 (Sylgard 184, Ellsworth Adhesives, Germantown, WA, USA) on their corresponding 3D printed mold and curing them at 75 °C for 2 hours. To obtain the interstitium chamber with an open structure, the PDMS mixture was sandwiched between the 3D mold and a transparency film with a glass slide under a compressive pressure of approximately 1 MPa (illustrated in the red box in Figure 5.1D). The pneumatic chamber was permanently bonded with a thin PDMS membrane via a microtransfer assembly (μTA) technique that we developed previously.[20] Briefly, the thin PDMS membrane was prepared by spin-coating a PDMS mixture on a silicon wafer at 2500 rpm for 1 minute and curing it at 75 °C for 1 hour. The pneumatic chamber with the opening facing down was then stamped on a thin PDMS layer, which was spin-coated on a silicon wafer at 4000 rpm for 30 seconds, and transferred onto the thin PDMS membrane, followed by curing at 75 °C for 1 hour under a compressive pressure of approximately 1 MPa. Subsequently, the pneumatic chamber with the PDMS membrane was gently peeled off from the silicon wafer and was bonded with the middle interstitium chamber reversibly by applying the μTA technique again. For the reversible bonding, first, a 33% solution of PDMS mixture in hexane (Thermo Fisher Scientific, Waltham, MA, USA) was spin-coated on a silicon wafer at 4000 rpm for 2 minutes to form a thin adhesive layer, followed by prebaking at 50 °C for 5 minutes. Secondly, the interstitium chamber was stamped on the adhesive layer for 30 seconds and then transferred onto the pneumatic chamber, followed by curing at 75 °C for 1 hour under a compressive pressure of approximately 1 MPa. Next, the nanofibrous membrane (with medium pores as described in chapter 2) was reversibly

bonded between the interstitium and air chambers following the aforementioned bonding process. One hole was punched in the pneumatic chamber and connected via the stainless-steel tubing to a programmable syringe pump (PHD 2000, Harvard Apparatus, Holliston, MA, USA), which provided cyclic mechanical stretch. Two holes were made in the air chamber as basal in and out ports for the culture medium perfusion through the interstitium chamber.

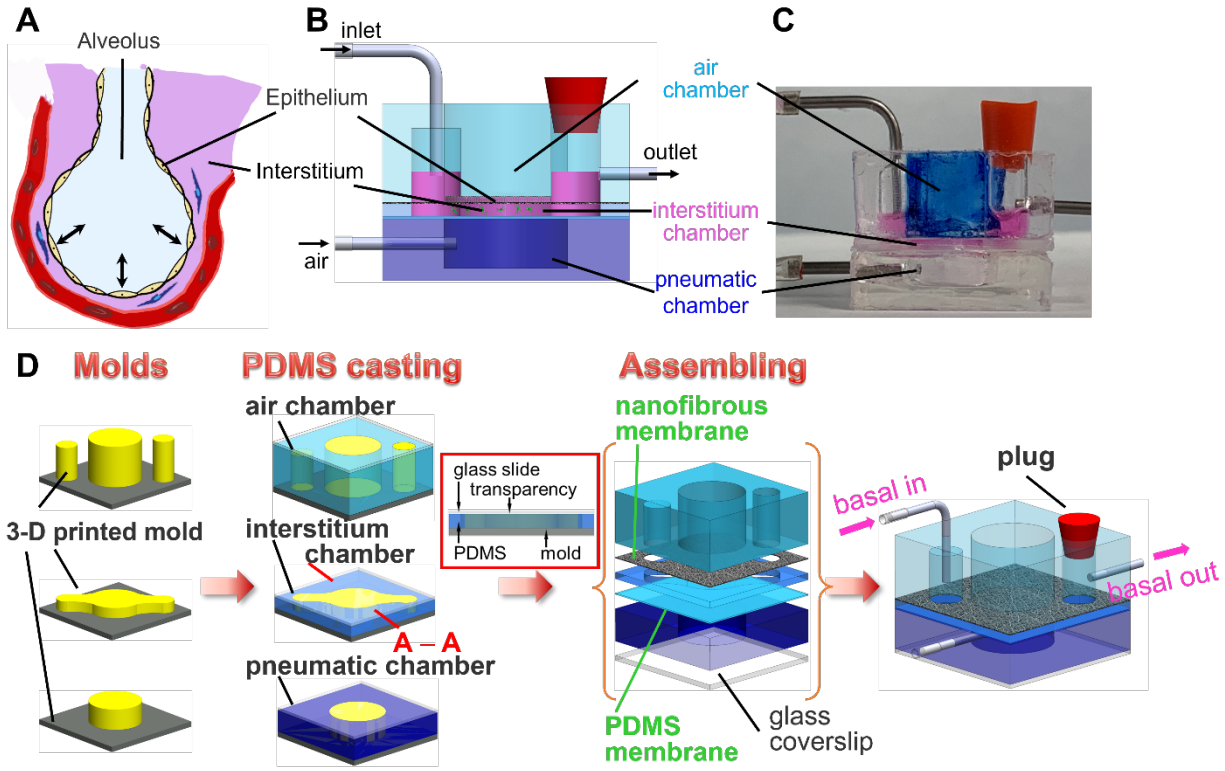

Figure 5.1: Design and fabrication of human lung alveolar interstitium chip. (A) Schematic illustration of human lung alveolus. (B) design, (C) photo, and (D) fabrication of the chip. The red box in (D) is the cross-sectional view of A-A of the interstitium chamber fabrication.

5.2.3 Computational Simulation of Interstitial Velocity and Shear Stress

The design of the interstitium chamber and computational fluid dynamics simulation of the interstitial velocity and shear stress were performed using SOLIDWORKS 2021 (Dassault Systems SOLIDWORKS Co., Waltham, MA, USA). The

chamber design and dimensions were shown in Figure 5.2. For an interstitial perfusion volume flow rate (*i.e.*, 20 μl/hour in this study), the fluidic velocity and shear stress were simulated and exported using the built-in Flow Simulation module. For the simulation, the porous media function was applied to the chamber to mimic the collagen matrix. The porosity, pore size setting and other parameter inputs are given in the table below. In the Simulation module, a 95% porosity was used to estimate the porous structure of collagen, and thus the simulation results were the approximation. For comparison, additional setting where the chamber was filled with water was also simulated.

Input Settings	Value
Porosity of collagen	95%
Pore size	10um
Gravity	9.81m/s^2
Temperature	310.2K
Density of Water	998.1kg/m^3
Dynamic viscosity	0.00066238Pa*s

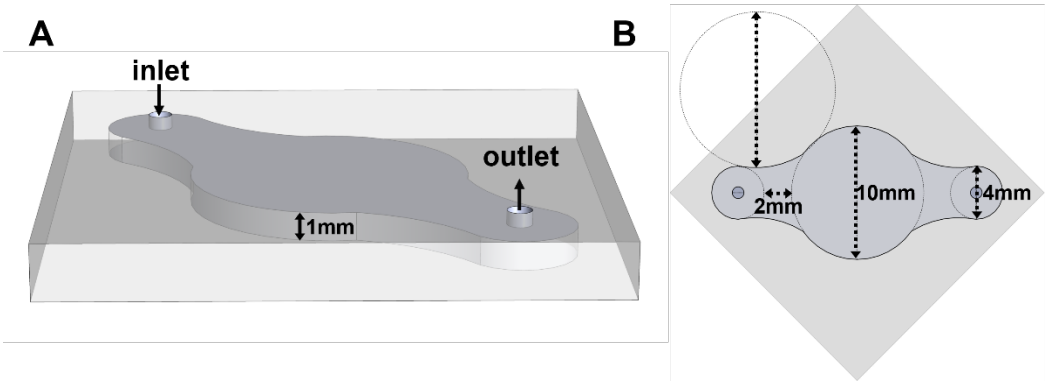

Figure 5.2: (A) Perspective and (B) top views of the interstitium chamber for Solidworks simulation.

5.2.4 Characterization of Mechanical Stretch

The mechanical strain (deformation) of the PDMS membrane on the pneumatic chamber with and without the interstitium layer was characterized using a method that we

previously described.[19] Briefly, the deformation of the membrane or the membrane with interstitium layer was imaged using a charge-coupled device (CCD) camera (Model DMK 31; The Imaging Source, Charlotte, NC, USA). The captured images were adjusted using ImageJ to get a curvilinear profile, which was then digitalized using GetData Graph Digitalizer (http://www.getdata-graph-digitalizer.com). The measured linear strain was compared with the theoretical calculation as previously described.[19]

5.2.5 Transwell Culture Models

Transwell co-culture models were prepared as the control for the interstitium chip studies in 12-well transwell plate. NHLF at a seeding density of 2×10^5 cells/cm^2 were seeded onto the basal side of the transwell insert membrane (0.6 μm; Sterlitech, Auburn, WA, USA) and incubated for 1 hour. The insert was then inverted and A549 cells at 2×10^5 cells/cm^2 were placed in the upper compartment. For the ALI culture, the epithelial cell culture medium was removed after one week from the insert and the mixed epithelial and fibroblast culture media (1:1; v/v) was added to the low compartment and changed every three days.

5.2.6 Cell Culture on Lung Interstitium Chips

The chip was first oxygen plasma treated at the medium power for 1 minute in a plasma cleaner (Model PDC-001; Harrick Plasma, Ithaca, NY, USA) and sterilized with 70% ethanol for 1 hour, followed by rinsing with phosphate buffered saline (PBS; Sigma-Aldrich). Then, 500 μl of 50 μg/ml Col I solution (rat tail; Corning, Corning, NY, USA) was added to the cell culture chamber and interstitium chamber and incubated overnight in an incubator for the surface coating. The interstitium layer was prepared with Col I or Col I-fibrin blend hydrogel. In the case of Col I gels, Col I solution was prepared by mixing Col

I, 10 × PBS, 1 N sodium hydroxide, and culture medium following the manufacturer's protocol to obtain a final Col I concentration of 3 mg/ml. In the case of Col I-fibrin blend gels, fibrin solution was prepared by mixing solution A (a mixture of bovine fibrinogen (Sigma-Aldrich) and ε-aminocaproic acid (EACA, Sigma-Aldrich)) and solution B (a mixture of bovine thrombin (Sigma-Aldrich) and calcium chloride ($CaCl_2$, Sigma-Aldrich)), with a final concentration of 5 mg/ml fibrinogen, 2 U/ml thrombin, and 5 mM $CaCl_2$, and 2 mg/ml EACA. Subsequently, the fibrin solution was mixed with Col I solution (3 mg/ml) and human lung fibroblasts (at a seeding density of 2.0×10^5 cells/mL), and the mixture was injected into the interstitium chamber and incubated at 37°C for 4 hours to form the cell-laden hydrogel matrix. The A549 cells at a density of 2.0×10^5 cells/cm^2 were then added into the air chamber and cultured under static condition for three days before the interstitial flow and cyclic mechanical stretch were applied. After cultured for one week under the mechanical stretch, the epithelial cell culture medium was aspirated from the air chamber and a mixed epithelial and fibroblast culture media (1:1, v/v) supplemented with EACA (2 mg/ml) was perfused through the interstitium chamber.

5.2.7 Permeability Assay

In the transwell models, 500 μl of 4 kDa (100 μg/ml) or 70 kDa (500 μg/ml) fluorescein isothiocyanate (FITC)-dextran (Sigma-Aldrich) was added to the insert and 1 ml of cell culture medium was added to the low compartment. The fluorescence intensity of the medium from the insert and the low compartment was measured after incubation for 2 hours. On the chip, the interstitium perfusion was halted and 200 μl of FITC-dextran was added into the air chamber. The chip was incubated for 2 hours in an incubator and

the gel and medium in the interstitium were collected after the chip was dissembled for fluorescence intensity measurement.

The concentration of FITC-dextran was determined by the fluorescence intensity referring to a calibration curve of FITC-dextran concentration vs fluorescence intensity. The apparent permeability P_{app} was calculated as $P_{app} = \frac{C_b V_b}{tA\Delta C}$, where C_b and V_b are the dextran concentration and solution volume in the low compartment of transwell or interstitium chamber of the chip, respectively, t is the diffusion time, A is the total area of diffusion, ΔC is the concentration change across the barrier.[21] The permeability coefficient of the epithelial barrier, P_{epi}, was determined from the P_{app} and the background permeability coefficient P_0 (measured in a transwell plate or chip without epithelium) as follows: $\frac{1}{P_{epi}} = \frac{1}{P_{app}} - \frac{1}{P_o}$ (s/cm).

5.2.8 SEM Observation

The epithelial cells were fixed *in situ* with 4% paraformaldehyde (PFA; Sigma-Aldrich) and 2% glutaraldehyde solution (Fisher Chemical, Fairlawn, NJ, USA) at room temperature for 4 hours and then dehydrated with gradient ethanol (30%, 50%, 70%, 80%, 90%, 95%, and 100%) and then hexamethyldisilazane (HMDS), each step for 10 minutes. The epithelial cell layer on the nanofibrous membrane or the transwell membrane was taken off, sputter-coated with gold using Denton Vacuum Desk V sputter coater (Denton Vacuum, Moorestown, NJ, USA) and imaged using a scanning electron microscope (SEM; TM3030 Plus, Hitachi High-Technologies Co., Tokyo, Japan).

5.2.9 CNT Penetration Assay

MWCNTs (XNRI MWNT-7; Mitsui & Company, NY, USA) were dispersed in PBS containing 5 mg/ml of bovine serum albumin (BSA) and diluted in culture medium to a concentration of 5 μg/ml as previously reported.[22] The MWCNT suspension was added to the transwell insert or the chip air chamber, similar to the permeability assay in 5.2.7, with the MWCNT suspension replacing the FITC-dextran. After incubation at 37 °C for 24 hours, the medium in transwell low compartment was collected for optical density (OD) measurement. On the chip the gel and medium in the interstitium chamber were collected and digested with 4 mg/ml collagenase in PBS at 37 °C before the OD measurement. The OD 640 value of the solution was measured and MWCNTs concentration was calculated by normalizing the OD value with the value obtained from the standard curve and thus the relative transport across the barrier was calculated.

5.2.10 Real-time Quantitative Reverse Transcription-polymerase Chain Reaction (qRT-PCR) Assay

After MWCNT treatment, the pro-inflammatory cytokines IL-4, 6, 8 expressions of the NHLFs from the chip and transwell culture were analyzed using qRT-PCR assay. The NHLF in the interstitium on the chip was collected by incubating with 4 mg/ml collagenase at 37 °C and centrifuged for 5 minutes at 400 g at 4 °C. The total RNA was extracted using Aurum Total RNA Mini Kit (Bio-Rad) and the cDNA was synthesized using iScript RT Supermix (Bio-Rad). The qRT-PCR samples were prepared using SsoAdvanced Univ SYBR Grn Suprmix (Bio-Rad). The reaction was performed using CFX96 Touch Real-Time PCR Detection System (Bio-Rad) under the following conditions: 40 cycles of 95 °C for 15 seconds, 60 °C for 30 seconds, followed by a melt curve of 65-95 °C at 0.5 °C increments qt 2-5 seconds/step. The primer sequences used were shown in Table 5.1.

The mRNA expressions were normalized to α-tubulin expression.

Table 5.1: Primers for qRT-PCR

Gene	Primer Sequence
IL-4	Forward: TCTTTGCTGCCTCCAAGAACA Reverse: GTAGAACTGCCGGAGCACAG
IL-6	Forward: TCCGGGAACGAAAGAGAAGC Reverse: GAGAAGGCAACTGGACCGAA
IL-8	Forward: ACACTGCGCCAACACAGAAA Reverse: CAACCCTCTGCACCCAGTTT
TUBA1A	Forward: CGGGCAGTGTTTGTAGACTTGG Reverse: CTCCTTGCCAATGGTGTAGTGC

5.2.11 Statistical Analysis

The data were presented as mean ± standard error of the mean (S.E.M.). The statistical differences were analyzed using two-tailed *t* test using Prism 8 (GraphPad software, San Diego, CA, USA). Statistically significant differences were considered at a level of $p < 0.05$.

5.3 Results and Discussion

5.3.1 Design and Fabrication of Human Alveolar Interstitium Chip

The functions of lung alveoli are profoundly affected by alveolar anatomical and physiological characteristics. Anatomically, the alveolar wall is a thin epithelium that faces the alveolar lumen and covered with a thin fluid layer to form an ALI. Supported by a microporous basement membrane, the epithelium forms a barrier due to the presence of tight junction and adherens junction,[23] which prevents access of nanomaterials to the subepithelium.[24] The interstitium surrounding the epithelium displays an interrelated framework of extracellular matrix (ECM) proteins such as collagen and elastin and is rich with interstitial fluids.[25] *In vivo* studies suggest that the penetration of nanomaterials

into the lung interstitium and interaction with local fibroblasts may be a critical step in nanomaterial induced fibrogenesis.[26] A key cellular mechanism of fibrogenesis is fibroblast activation and subsequent induction of ECM (in particular, collagen) production and accumulation leading to fibrosis.[27, 28] Lung fibroblasts exhibit the stiffness-dependent fibrogenic responses to MWCNTs.[22] In addition, the interstitial fluid flow could alter cytoskeletal organization, influence cell proliferation, and remodel interstitial matrix.[29, 30] Moreover, the breathing movements expose the epithelium and interstitium to cyclic 3D stretching and relaxation. The mechanical stretch is known to have profound influences on the formation and function of cells, tissues, and organs.[31]

To establish primary functions of lung alveoli, we developed a dynamic human lung alveolar interstitium-on-a-chip (interstitium chip) system, which closely replicates the key anatomical (nanofibrous membrane to imitate the basement membrane) and physiological (interstitial matrix stiffness, interstitial flow, and cyclic 3D breathing-like mechanical stretch) characteristics of human lung alveoli (Figure 5.1).

The chip consisted of a co-culture part and a pneumatic part, both made of PDMS. The co-culture part was comprised of an air (apical) chamber and an interstitium (basal) chamber, between which an electrospun nanofibrous membrane (~10 μm thick, 8.75 ± 5.79 μm^2 pore size) was sandwiched. Human lung alveolar epithelial cells formed a tight epithelium on the nanofibrous membrane at the ALI in the air chamber. Human lung fibroblasts were embedded in a 3D collagenous matrix in the interstitium chamber. The pneumatic part was formed by permanently bonding a PDMS membrane (15 μm thick) on the pneumatic chamber.

The stiffness of the interstitial matrix was primarily determined by a type I collagen

(Col I) gel. The stiffness of Col I gel can be controlled, with values ranging between 1 kPa and 100 kPa, by adjusting the concentration of Col I solution between 3 and 60 mg/mL, respectively.[32] These stiffnesses cover human normal (1-5 kPa) and fibrotic (20-100 kPa) lung tissues.[33-35] A syringe pump was be used to perfuse culture media continuously into the interstitium chamber to generate an interstitial flow of physiological relevance,[36-39] as demonstrated in our computational simulation (Figure 5.3).

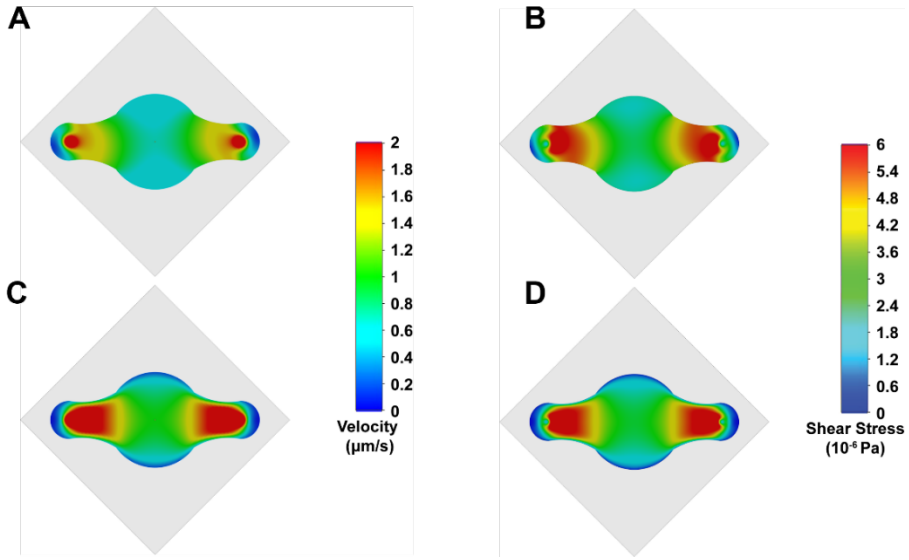

Figure 5.3: Solidworks simulation of the interstitial fluidic flow. (A, C) interstitial fluidic velocity and (B, D) shear stress profiles of interstitium chamber filled (A, B) with the collagen gel or (C, D) water at a constant interstitial volumetric flow rate of 20 μl/hour.

Our previous study revealed that physiologically relevant cyclic 3D mechanical stretch significantly upregulated the expression of tight and adhesions junction proteins compared to 1D and 2D stretches and the static controls.[19] A circular PDMS membrane was thus designed for the pneumatic chamber to provide 3D stretch. When air was pumped in and withdrawn from the pneumatic chamber, the PDMS membrane, the interstitium, and the nanofibrous membrane moved up and down, generating 3D radial stretch to mimic breathing movements. There was no significant difference between the

experimental observation and the theoretical strain (Figure 5.4). Thus, the mechanical stretch was transmitted through the interstitium to the nanofibrous membrane, which exposed the fibroblasts in the interstitium and the epithelial cells on the nanofibrous membrane to the designated strain. The level of applied strain ranges from 5% to 15% at a frequency of 0.2 - 0.3 Hz (12-20 times/minute) to match normal levels of strain observed in alveoli within the whole human lung *in vivo*.[40]

Figure 5.4: Characterization of mechanical stretches. Original CCD images (left) and the profiles (black curve in the right) of the deformed (A) PDMS membrane bonded on the pneumatic chamber and (B) nanofibrous membrane on the interstitial layer bonded on the pneumatic chamber under a theoretical strain of 15% (yellow curve).

These anatomical (nanofibrous membrane) and physiological (interstitium matrix stiffness, interstitial flow, and cyclic 3D stretch) characteristics of the interstitium chip could be adjusted and optimized to promote and sustain the chip function. In addition, the air chamber, nanofibrous membrane, and interstitium chamber were assembled into the co-culture part by applying the μTA technique that we previously developed based on microcontact printing with PDMS prepolymer thin film as the adhesive.[20] This technique allowed us to adjust adhesive strength between the chip parts by controlling the extent of partial curing of the PDMS thin film and thus separate the parts selectively for the downstream analysis.

5.3.2 Epithelium Formation in the Lung Interstitium Chip

We constructed the interstitium chip with the identified nanofibrous membrane and other key physiological parameters, namely, the interstitium matrix stiffness, interstitial

fluid, and cyclic 3D mechanical strain. Collagen is most abundant protein in the interstitium matrix and thus Col I gel was used as the interstitial matrix for 3D culture of normal NHLFs on the chip. Our previous study highlighted the significance of matrix stiffness in the fibrogenic responses of lung fibroblasts to MWCNTs.[22] On the chip the concentration of Col I was adjusted to 3 mg/mL to form a gel of 1 kPa in stiffness to resemble the stiffness of normal lung tissue.[34, 41] The interstitial medium perfusion rate was set as 20 μl/hour, which generated an average interstitial fluidic velocity of 0.6 – 1.4 μm/s (also see Figure 5.3), whining the physiological range, *i.e.*, 0.1 – 4.0 μm/s.[38, 39] To replicate the cyclic strain that lung alveoli experience during breath movement, which is 5 – 15% linear strain at a frequency of 0.2 – 0.3 Hz in normal conditions, a theoretical maximum 15% linear strain was applied at a frequency of 0.2 Hz. For comparison, the conventional transwell model was built as the controls. In the transwell model, the epithelial and fibroblast cells were grown on the apical and basal side of the insert membrane, respectively.

After one-week culture, the epithelial cells formed a dense epithelial layer on the chip; however, the gaps between the epithelial cells were evident in the transwell model (Figure 5.5A, B). The epithelium permeability was evaluated using dextrans of 4 kDa and 70 kPa in molecular weight, which represent the intermediate and large-size agents transported through tight junctions.[42, 43] As shown in Figure 5.5C, the permeability of both dextrans through cells grown on the chip was about 3~4 folds lower than that the transwell model, *i.e.*, $2.16\pm0.51 \times 10^{-5}$ vs. $6.12\pm2.58 \times 10^{-5}$ cm/s for 4 kDa dextran, and $7.79\pm1.75 \times 10^{-6}$ vs. $2.97\pm1.21 \times 10^{-5}$ cm/s for 70 kDa dextran. Note that the epithelium permeability of 4 kDa dextran on the chip was also improved by 2-fold compared to the

monoculture on the nanofibrous membrane (Table 5.2, also see Figure 2.10 in chapter 2), *i.e.*, 2.16 ± 0.51 × 10^{-5} vs. 5.73±2.70 × 10^{-5}.

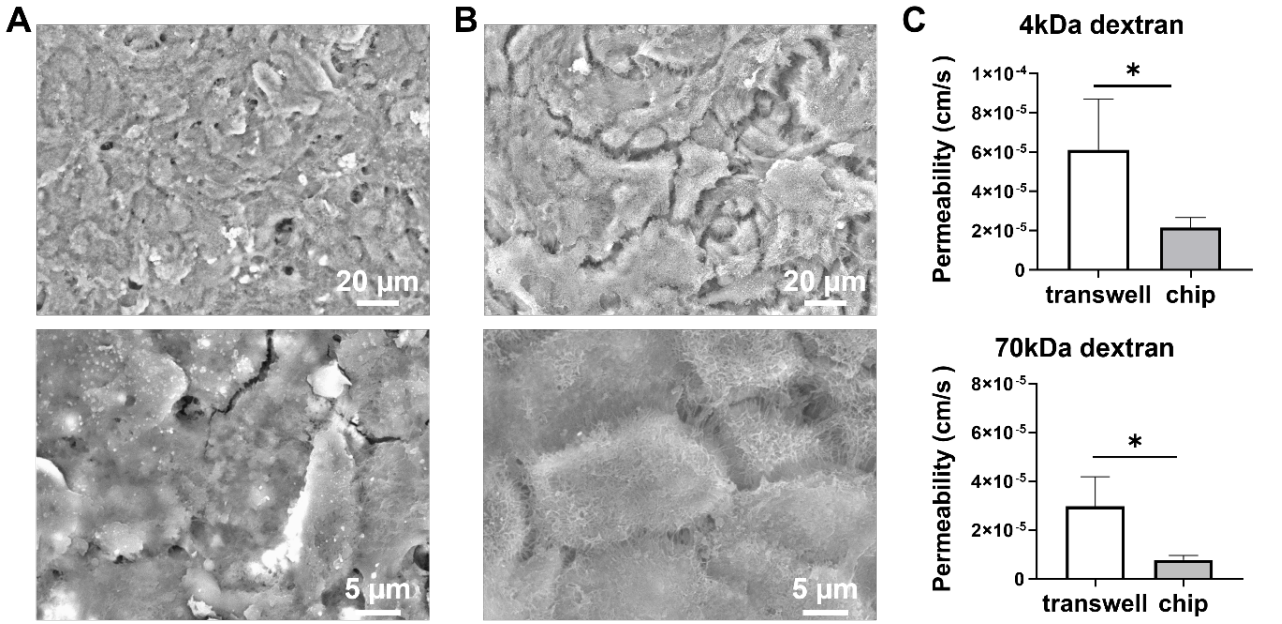

Figure 5.5: Epithelial barrier function in the interstitium chip. Low and high magnification SEM images of the epithelial monolayer (A) on the chip and (B) in the transwell model. (C) Comparison of dextran permeability on the chip and the transwell model after 1-week of culture. *: p < 0.05 compared to transwell model.

Table 5.2: Permeability summary

Model	Duration	Permeability (cm/s)	
		4 kDa dextran	70 kDa dextran
Interstitium chip	4 weeks	7.08±1.24 × 10^{-6}	9.77±0.84×10^{-8}
	1 week	2.16±0.51 × 10^{-5}	7.79±1.75 ×10^{-6}
Transwell co-culture	4 weeks	4.96±3.39 ×10^{-5}	1.73±0.40×10^{-6}
	1 week	6.12±2.58 × 10^{-5}	2.97±1.21 × 10^{-5}
Nanofibrous membrane only	1 week	5.73±2.73 × 10^{-5}	-
Literature reports[42, 44, 45]		10^{-6} - 10^{-5}	10^{-7}- 10^{-6}

In brief, the biomimetic interstitium chip demonstrated enhanced epithelial barrier function compared to a conventional transwell model and monoculture on the nanofibrous membrane. This enhancement was likely attributed to the synergy of the nanofibrous

membrane, co-culture of the epithelial and fibroblast cells in a 3D gel, and physiologically relevant interstitium matrix stiffness, interstitial flow, and cyclic 3-D stretch.

5.3.3 Maintenance of the Lung Interstitium Chip

After two weeks culture, interstitial matrix degradation and remodeling were observed on the chip. It is known that collagenous gels degrade relatively fast, and fibroblasts caused collagen gel contraction.[46] To alleviate the interstitium deterioration, fibrin was utilized to reinforce the collagen gel because fibrin gels have been reported to be stable for at least 12 months.[47] The degradation of fibrin gels, a process called fibrinolysis, can be controlled by inhibiters such as EACA.[48] Additionally, fibrin gels can facilitate cell adhesion and promote fibroblasts to synthesize more collagen and other ECM proteins compared to collagen gels.[49, 50] Compared with pure collagen and fibrin gels, the Col I-fibrin blend gels exhibit intermediate properties.[51] Therefore, we prepared Col I-fibrin blend gels by mixing Col I solution and fibrin solution at volume ratios from 1:0.1 to 1:1 for 3D culture of the lung fibroblasts. After cultured under static conditions for two weeks, no evident gel deformation was observed, and the fibroblasts spread, and cell elongation increased with an increase in the fibrin concentration (Figure 5.6). The observation indicated that adding fibrin improved the interstitium integrity and hence the chip longevity could be extended. To maintain the matrix stability while maximize the collagen content, the Col I-fibrin gel with a ratio of 1:0.3 was used for long term culture of the chip.

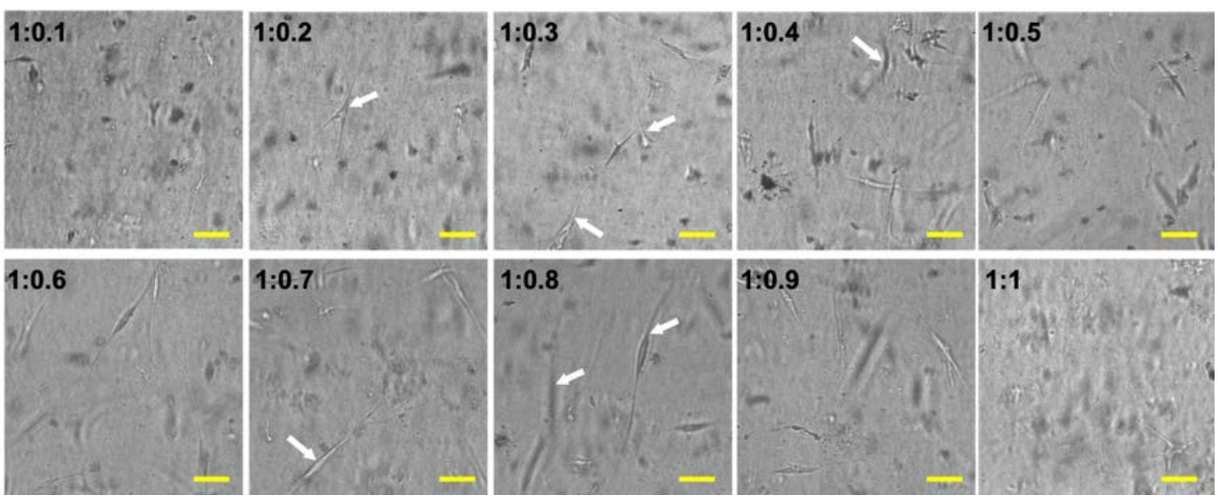

Figure 5.6: NHLF cultured in Col I-fibrin blend gels for 14 days with Col I: fibrin ratio ranging from 1:0.1 to 1:1. Scale bars: 100 μm. The white arrows indicated the cells.

On the chip with Col I-fibrin gel as interstitial matrix, the epithelial cells formed a monolayer after one-week culture. The epithelial growth medium was then aspirated from

the air chamber to form an ALI and a mixed epithelial and fibroblast culture media (1:1, v/v) was perfused into the interstitium chamber. Three weeks later, a tight epithelium formed and the A549 cells displayed cuboidal shape and presented apical microvilli – the typical ultrastructural feature of human alveolar epithelial type II (ATII) cells (Figure 5.7). The layered structure of epithelium, secreted ECM, and electrospun nanofibrous membrane was evident in Figure 5.7C. Importantly, the epithelium permeability was further enhanced. For example, for 4 kDa dextran, the permeability decreased by 3-fold from 2.16±0.51 × 10^{-5} cm/s (1 week) to 7.08±1.24 × 10^{-6} cm/s (4 weeks), significantly lower than 4.96±3.39 × 10^{-5} cm/s of the transwell model. For 70 kDa dextran, the permeability decreased by about 80-fold, from 7.79±1.75 × 10^{-6} cm/s (1 week) to 9.77±0.84 × 10^{-8} cm/s (4 weeks) compared to 1.73±0.40 × 10^{-6} cm/s of the transwell model (Table 5.2, Figure 5.7D). The enhanced epithelium permeability values were comparable or lower than literature reports using transwell models and microfluidic devices.[42, 44, 45]

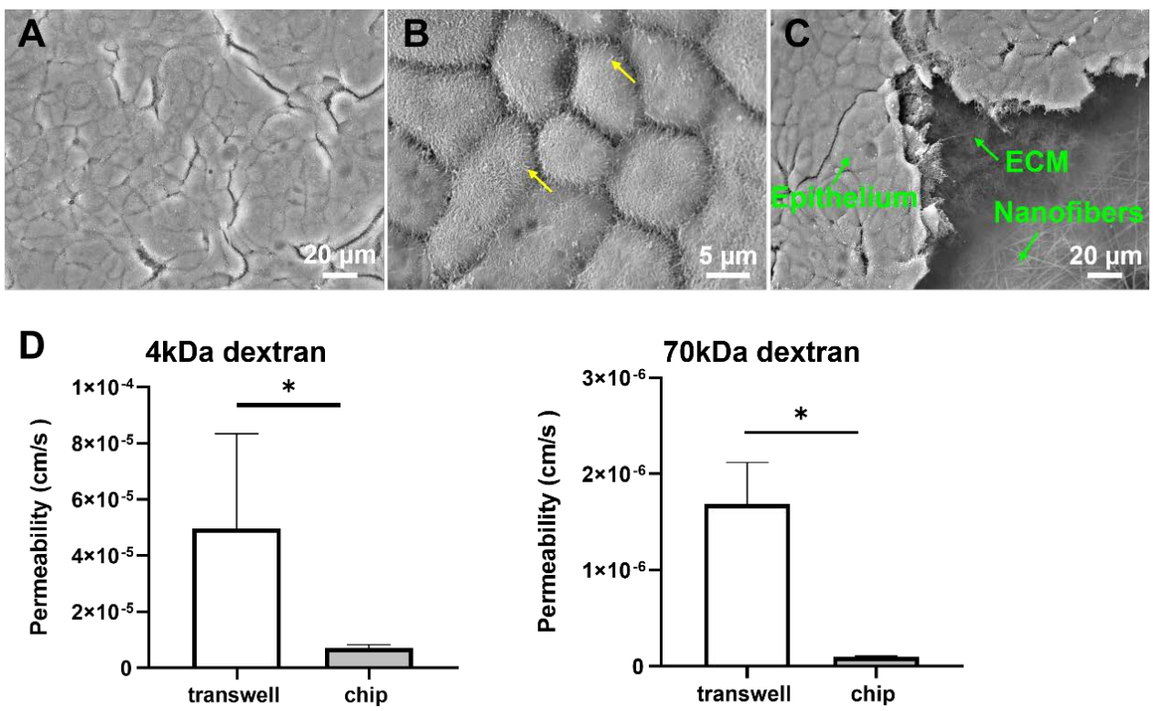

Figure 5.7: Maintenance of the lung interstitium chip. (A) Low and (B) high magnification SEM images of the epithelium on the chip. The yellow arrows in (B) point to the apical microvilli. (C) SEM image of the layered structure of the epithelium on the chip. (D) Dextran permeability of the epithelium after 4-week culture in the chip. *: $p < 0.05$ compared to the transwell models.

The A549 cells feature some of the ATII cell properties and are often used in *in vitro* lung alveolar models.[44] It was reported that ATII cells cocultured in transwell with lung fibroblasts embedded in 3D matrix maintained their distinct phenotype for 7 days;

conversely, the cells lost their phenotype within 3-5 days on conventional 2D models.[52, 53] On this interstitium chip, the A549 cells formed a tight epithelium in one week and displayed distinct ATII cell structural features like cuboidal shape and apical microvilli. Moreover, the epithelium permeability was significantly lower than the transwell models. Of note, no evident deterioration of the chip was observed in 8-week culture; conversely, individual epithelial cells instead of continuous cell monolayer was observed in the transwell model (Figure 5.8).

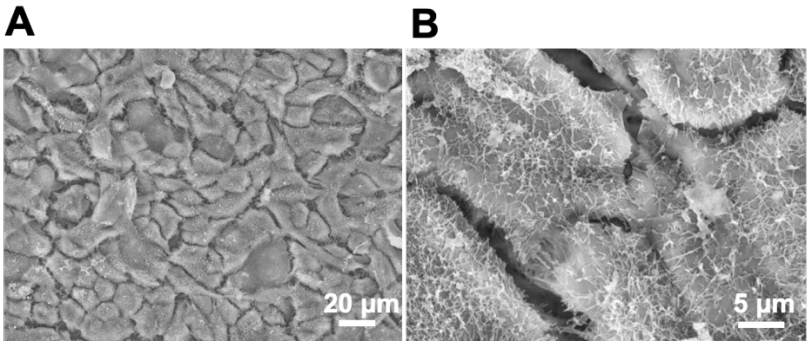

Figure 5.8 SEM images of epithelial cell layer in the transwell model with (A) low and (B) high magnification after 8-week culture.

The biomimetic interstitium chip demonstrated enhanced epithelial barrier function with extended longevity. Fibrin is known to be formed by enzymatic cleavage and reorganization of fibrinogen and thrombin,[54] and thus the gel degradation can be adjusted by tuning the concentration and administration of the inhibitor EACA, which blocks the binding of plasmin or plasminogen to fibrin,[48] to sustain the interstitium integrity. Moreover, the A549 cell line provides a reliable and straightforward cell source for the chip development, the cells are from a lung tumor, are likely genetically unstable, and might not fully recapitulate the epithelial barrier function *in vivo*. The use of primary human alveolar epithelial cells or epithelial basal stem cells will facilitate the

establishment of a more *in vivo* like model.[55] Human macrophages can also be co-cultured with the epithelial cells at the ALI to facilitate the maintenance of lung homeostasis.[56] Taken together, the key alveolar microenvironmental factors can be fine-tuned to further improve the chip longevity and performance.

5.3.4 CNT Toxicity Study Using the Biomimetic Interstitium Chip

We explored the potential application of this lung interstitium chip for nanotoxicity study. Of interest were MWCNTs because MWCNTs have been extensively assessed both *in vivo* and *in vitro*,[57-59] which provided the benchmark for the chip validation.

After the epithelium was exposed to MWCNTs (5 μg/ml) for 24 hours, the transport of MWCNTs through the epithelium and lung inflammatory response to the MWCNTs were examined. The percentage of MWCNTs that penetrated across the epithelium into the interstitium on the chip was 2.24±1.80 %, significantly lower than 7.61±2.85 % in the transwell model (Figure 5.9A), being consistent with *in vivo* observations.[57] The culture medium was also collected from the interstitium chamber and multiple inflammatory chemokines were measured. Although the expression of interleukin-4 (IL-4) and IL-6 was too weak to be detected, the IL-8 expression of the fibroblasts was lower on the chip than the transwell model (Figure 5.9B). Inhaled nanoparticles have been shown to pass through the epithelium barrier to the subepithelium and induce lung diseases by stimulating profibrotic responses and proinflammatory cytokine and chemokine secretion [60, 61] The interstitium chip exhibited enhanced epithelial barrier function compared to the transwell models. As such, the penetration of MWCNTs across the epithelium was substantially reduced, and subsequently, the inflammatory responses of the fibroblasts to MWCNTs were alleviated, being in line with previously reports.[57, 62, 63]

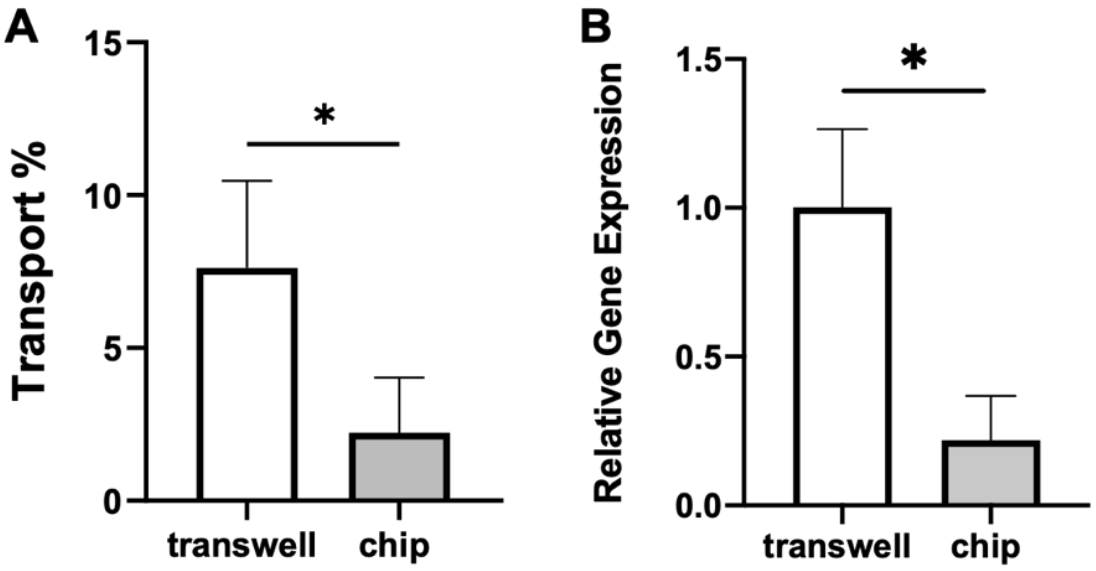

Figure 5.9: Toxicity assessment of MWCNTs on the chip and transwell model. (A) Percentage of MWCNTs penetrated across the epithelium. (B) Expression of IL-8 of the fibroblasts after the epithelium exposed to MWCNTs for 24 hours, *: $p < 0.05$ compared to the transwell model.

5.4 Conclusion

The developed lung alveolar interstitium chip closely imitated the key anatomical (epithelial cells co-cultured with fibroblasts encapsulated in 3D collagenous interstitial matrix via nanofibrous membrane) and physiological (interstitium matrix stiffness, interstitial flow, and 3D breathing-like mechanical stretch) characteristics of human lung alveolus. The biomimetic interstitium chip demonstrated enhanced epithelial barrier function and extended longevity beyond 8 weeks with Col I-fibrin blend gels as the interstitium matrix. The key alveolar microenvironmental factors such as nanofibrous membrane and interstitial matrix can be fine-tuned to maintain the homeostasis of the epithelium and interstitium and thus extend the chip longevity. Importantly, the toxicity assessment of MWCNTs on the chip verified that the biomimetic interstitium chip represented a useful *in vitro* model for human lung alveolar interstitium.

5.5 References

[1] A.M. Schrand, L. Dai, J.J. Schlager, S.M. Hussain, Toxicity testing of nanomaterials., Advances in Experimental Medicine and Biology 745 (2012) 58-75.

[2] A. Helland, P. Wick, A. Koehler, K. Schmid, C. Som, Reviewing the environmental and human health knowledge base of carbon nanotubes, Environmental health perspectives 115(8) (2007) 1125-31.

[3] J.P. Ryman-Rasmussen, M.F. Cesta, A.R. Brody, J.K. Shipley-Phillips, J.I. Everitt, E.W. Tewksbury, O.R. Moss, B.A. Wong, D.E. Dodd, M.E. Andersen, J.C. Bonner, Inhaled carbon nanotubes reach the subpleural tissue in mice., Nature Nanotechnology 4(11) (2009) 747-51.

[4] M. Beck-Broichsitter, O.M. Merkel, T. Kissel, Controlled Pulmonary Drug and Gene Delivery Using Polymeric Nano-carriers, J Control Release 161(2) (2012) 214-224.

[5] J.J. Pippin, Animal Research in Medical Sciences: Seeking a Convergence of Science, Medicine, and Animal Law, South Texas Law Review 54 (2013) 469-511.

[6] S. De Minicis, E. Seki, H. Uchinami, J. Kluwe, Y. Zhang, D.A. Brenner, R.F. Schwabe, Gene Expression Profiles during Hepatic Stellate Cell Activation in Culture and in vivo, Gastroenterology 132(5) (2007) 1937-46.

[7] C.E. Barkauskas, M.I. Chung, B. Fioret, X. Gao, H. Katsura, B.L.M. Hogan, Lung organoids: current uses and future promise, Development 144(6) (2017) 986-997.

[8] J. Kong, S. Wen, W. Cao, P. Yue, X. Xu, Y. Zhang, L. Luo, T. Chen, L. Li, F. Wang, Lung organoids, useful tools for investigating epithelial repair after lung injury, Stem Cell Research & Therapy 12(1) (2021) 1-13.

[9] D. Huh, B.D. Matthews, A. Mammoto, M. Montoya-Zavala, H.Y. Hsin, D.E. Ingber, Reconstituting Organ-level Lung Functions on a Chip, Science 328(5986) (2010) 1662-8.

[10] K. Ronaldson-Bouchard, G. Vunjak-Novakovic, Organs-on-a-Chip: A Fast Track for Engineered Human Tissues in Drug Development, Cell Stem Cell 22(3) (2018) 310-324.

[11] D. Huh, D.C. Leslie, B.D. Matthews, J.P. Fraser, S. Jurek, G.A. Hamilton, K.S. Thorneloe, M.A. McAlexander, D.E. Ingber, A human disease model of drug toxicity-induced pulmonary edema in a lung-on-a-chip microdevice, Science Translational Medicine 4(159) (2012) 159ra147.

[12] K.H. Benam, R. Villenave, C. Lucchesi, A. Varone, C. Hubeau, H.H. Lee, S.E. Alves, M. Salmon, T.C. Ferrante, J.C. Weaver, A. Bahinski, G.A. Hamilton, D.E. Ingber, Small Airway-on-a-chip Enables Analysis of Human Lung Inflammation and Drug Responses in vitro, Nature Methods 13(2) (2016) 151-7.

[13] A. Sundarakrishnan, H. Zukas, J. Coburn, B.T. Bertini, Z.Y. Liu, I. Georgakoudi, L. Baugh, Q. Dasgupta, L.D. Black, D.L. Kaplan, Bioengineered in Vitro Tissue Model of Fibroblast Activation for Modeling Pulmonary Fibrosis, Acs Biomater Sci Eng 5(5) (2019) 2417-2429.

[14] J.C. Mejias, M.R. Nelson, O. Liseth, K. Roy, A 96-well Format Microvascularized Human Lung-on-a-chip Platform for Microphysiological Modeling of Fibrotic Diseases, Lab Chip 20(19) (2020) 3601-3611.

[15] C. Wang, J. Yang, Mechanical forces: the missing link between idiopathic pulmonary fibrosis and lung cancer, European Journal of Cell Biology (2022) 151234.

[16] D. Pankova, Y. Jiang, M. Chatzifrangkeskou, I. Vendrell, J. Buzzelli, A. Ryan, C. Brown, E. O'Neill, RASSF 1A controls tissue stiffness and cancer stem-like cells in lung adenocarcinoma, The EMBO journal 38(13) (2019) e100532.

[17] J.D. Stucki, N. Hobi, A. Galimov, A.O. Stucki, N. Schneider-Daum, C.M. Lehr, H. Huwer, M. Frick, M. Funke-Chambour, T. Geiser, O.T. Guenat, Medium throughput breathing human primary cell alveolus-on-chip model, Sci Rep 8(1) (2018) 14359.

[18] O.Y.F. Henry, R. Villenave, M.J. Cronce, W.D. Leineweber, M.A. Benz, D.E. Ingber, Organs-on-chips with Integrated Electrodes for Trans-epithelial Electrical Resistance (TEER) Measurements of Human Epithelial Barrier Function, Lab Chip 17(13) (2017) 2264-2271.

[19] K. Man, J. Liu, K.M. Phan, K. Wang, J.Y. Lee, X. Sun, M. Story, D. Saha, J. Liao, H. Sadat, Y. Yang, Dimensionality-Dependent Mechanical Stretch Regulation of Cell Behavior, ACS Applied Materials & Interfaces 14(15) (2022) 17081-17092.

[20] Y. Yang, K. Kulangara, J. Sia, L. Wang, K.W. Leong, Engineering of a microfluidic cell culture platform embedded with nanoscale features, Lab on a Chip 11(9) (2011) 1638-1646.

[21] Y. SY, R. RR, Chapter 3, Methods for Measuring Permeability, Regulation of Endothelial Barrier Function, Morgan & Claypool Life Sciences2010.

[22] K. Wang, L. Shi, W. Linthicum, K. Man, X. He, Q. Wen, L.W. Rojanasakul, Y. Rojanasakul, Y. Yang, Substrate stiffness-dependent carbon nanotube-induced lung fibrogenesis, Nano letters 19(8) (2019) 5443-5451.

[23] J.S. Lwebuga-Mukasa, G. Thulin, J.A. Madri, C. Barrett, J.B. Warshaw, An acellular human amnionic membrane model for in vitro culture of type II pneumocytes: the role of the basement membrane in cell morphology and function, Journal of Cellular Physiology 121(1) (1984) 215-225.

[24] K. Brune, J. Frank, A. Schwingshackl, J. Finigan, V.K. Sidhaye, Pulmonary epithelial barrier function: some new players and mechanisms, American Journal of Physiology-Lung Cellular and Molecular Physiology 308(8) (2015) L731-L745.

[25] C.A. Goncalves, M.H. Figueiredo, V.A. Bairos, Three-dimensional organization of the elastic fibres in the rat lung, Anat Rec 243(1) (1995) 63-70.

[26] R.R. Mercer, A.F. Hubbs, J.F. Scabilloni, L. Wang, L.A. Battelli, S. Friend, V. Castranova, D.W. Porter, Pulmonary fibrotic response to aspiration of multi-walled carbon nanotubes., Particle and Fibre Toxicology 8 (2011) 21.

[27] G. Raghu, Y.Y. Chen, V. Rusch, P.S. Rabinovitch, Differential proliferation of fibroblasts cultured from normal and fibrotic human lungs, The American Review of Respiratory Disease 138(3) (1988) 703-8.

[28] D.V. Pechkovsky, A. Prasse, F. Kollert, K.M. Engel, J. Dentler, W. Luttmann, K. Friedrich, J. Muller-Quernheim, G. Zissel, Alternatively activated alveolar macrophages in pulmonary fibrosis-mediator production and intracellular signal transduction, Clin Immunol 137(1) (2010) 89-101.

[29] E. Tzima, M. Irani-Tehrani, W.B. Kiosses, E. Dejana, D.A. Schultz, B. Engelhardt, G. Cao, H. DeLisser, M.A. Schwartz, A mechanosensory complex that mediates the endothelial cell response to fluid shear stress, Nature (London, United Kingdom) 437(7057) (2005) 426-431.

[30] C.P. Ng, M.A. Swartz, Fibroblast alignment under interstitial fluid flow using a novel 3-D tissue culture model, American Journal of Physiology-Heart and Circulatory Physiology 284(5) (2003) H1771-H1777.

[31] T. Mammoto, D.E. Ingber, Mechanical control of tissue and organ development, Development 137(9) (2010) 1407-1420.

[32] A. Tidu, D. Ghoubay-Benallaoua, B. Lynch, B. Haye, C. Illoul, J.M. Allain, V.M. Borderie, G. Mosser, Development of human corneal epithelium on organized fibrillated transparent collagen matrices synthesized at high concentration, Acta Biomaterialia 22 (2015) 50-58.

[33] S.J. Lai-Fook, R.E. Hyatt, Effects of Age on Elastic Moduli of Human Lungs, Journal of Applied Physiology 89(1) (2000) 163-8.

[34] D. Navajas, J. Alcaraz, R. Peslin, J. Roca, R. Farre, valuation of a Method for Assessing Respiratory Mechanics during Noninvasive Ventilation, European Respiratory Journal 16(4) (2000) 704-9.

[35] F. Liu, J.D. Mih, B.S. Shea, A.T. Kho, A.S. Sharif, A.M. Tager, D.J. Tschumperlin, Feedback amplification of fibrosis through matrix stiffening and COX-2 suppression, Journal of Cell Biology 190(4) (2010) 693-706.

[36] S. Wang, J.M. Tarbell, Effect of Fluid Flow on Smooth Muscle Cells in a 3-dimensional Collagen Gel Model Arteriosclerosis, Thrombosis, and Vascular Biology 20(10) (2000) 2220-5.

[37] C.P. Ng, B. Hinz, M.A. Swartz, Interstitial fluid flow induces myofibroblast differentiation and collagen alignment in vitro, Journal of cell science 118(20) (2005) 4731-4739.

[38] D. Wang, J. Tarbell, Modeling interstitial flow in an artery wall allows estimation of wall shear stress on smooth muscle cells, (1995).

[39] S.R. Chary, R.K. Jain, Direct measurement of interstitial convection and diffusion of albumin in normal and neoplastic tissues by fluorescence photobleaching, Proceedings of the National Academy of Sciences 86(14) (1989) 5385-5389.

[40] K.G. Birukov, J.R. Jacobson, A.A. Flores, S.Q. Ye, A.A. Birukova, A.D. Verin, J.G. Garcia, Magnitude-dependent Regulation of Pulmonary Endothelial Cell Barrier Function by Cyclic Stretch, The American Journal of Physiology-Lung Cellular and Molecular Physiology 285(4) (2003) L785-97.

[41] C.R.I. Lam, H.K. Wong, S. Nai, C.K. Chua, N.S. Tan, L.P. Tan, A 3D biomimetic model of tissue stiffness interface for cancer drug testing, Molecular pharmaceutics 11(7) (2014) 2016-2021.

[42] T.S. Frost, L. Jiang, R.M. Lynch, Y. Zohar, Permeability of Epithelial/Endothelial Barriers in Transwells and Microfluidic Bilayer Devices, Micromachines 10(8) (2019) 533.

[43] N. Kirschner, R. Rosenthal, M. Furuse, I. Moll, M. Fromm, J.M. Brandner, Contribution of tight junction proteins to ion, macromolecule, and water barrier in keratinocytes, Journal of Investigative Dermatology 133(5) (2013) 1161-1169.

[44] K.A. Foster, C.G. Oster, M.M. Mayer, M.L. Avery, K.L. Audus, Characterization of the A549 cell line as a type II pulmonary epithelial cell model for drug metabolism, Experimental cell research 243(2) (1998) 359-366.

[45] T.S. Frost, L. Jiang, Y. Zohar, Pharmacokinetic analysis of epithelial/endothelial cell barriers in microfluidic bilayer devices with an air–liquid interface, Micromachines 11(5) (2020) 536.

[46] Y. Zhu, C.M. Sköld, X. Liu, H. Wang, T. Kohyama, F.-Q. Wen, R.F. Ertl, S.I. Rennard, Fibroblasts and monocyte macrophages contract and degrade three-dimensional collagen gels in extended co-culture, Respiratory research 2(5) (2001) 1-7.

[47] D. Eyrich, F. Brandl, B. Appel, H. Wiese, G. Maier, M. Wenzel, R. Staudenmaier, A. Goepferich, T. Blunk, Long-term Stable Fibrin Gels for Cartilage Engineering, Biomaterials 28(1) (2007) 55-65.

[48] E.D. Grassl, T.R. Oegema, R.T. Tranquillo, Fibrin as an alternative biopolymer to type-I collagen for the fabrication of a media equivalent, J Biomed Mater Res 60(4) (2002) 607-612.

[49] T.L. Tuan, A. Song, S. Chang, S. Younai, M.E. Nimni, In vitro fibroplasia: matrix contraction, cell growth, and collagen production of fibroblasts cultured in fibrin gels, Exp Cell Res 223(1) (1996) 127-34.

[50] A.J. Gray, J.E. Bishop, J.T. Reeves, R.P. Mecham, G.J. Laurent, Partially degraded fibrin(ogen) stimulates fibroblast proliferation in vitro, Am J Respir Cell Mol Biol 12(6) (1995) 684-90.

[51] V.K. Lai, S.P. Lake, C.R. Frey, R.T. Tranquillo, V.H. Barocas, Mechanical behavior of collagen-fibrin co-gels reflects transition from series to parallel interactions with increasing collagen content, J Biomech Eng 134(1) (2012) 011004.

[52] J.M. Sucre, C.S. Jetter, H. Loomans, J. Williams, E.J. Plosa, J.T. Benjamin, L.R. Young, J.A. Kropski, C.L. Calvi, S. Kook, Successful establishment of primary type II alveolar epithelium with 3D organotypic coculture, American journal of respiratory cell and molecular biology 59(2) (2018) 158-166.

[53] H. Fehrenbach, Alveolar epithelial type II cell: defender of the alveolus revisited, Respiratory research 2(1) (2001) 1-20.

[54] H. Duong, B. Wu, B. Tawil, Modulation of 3D fibrin matrix stiffness by intrinsic fibrinogen-thrombin compositions and by extrinsic cellular activity, Tissue engineering. Part A 15(7) (2009) 1865-76.

[55] L. Si, H. Bai, M. Rodas, W. Cao, C.Y. Oh, A. Jiang, R. Moller, D. Hoagland, K. Oishi, S. Horiuchi, S. Uhl, D. Blanco-Melo, R.A. Albrecht, W.-C. Liu, T. Jordan, B.E. Nilsson-Payant, I. Golynker, J. Frere, J. Logue, R. Haupt, M. McGrath, S. Weston, T. Zhang, R. Plebani, M. Soong, A. Nurani, S.M. Kim, D.Y. Zhu, K.H. Benam, G. Goyal, S.E. Gilpin, R. Prantil-Baun, S.P. Gygi, R.K. Powers, K.E. Carlson, M. Frieman, B.R. tenOever, D.E. Ingber, A Human-airway-on-a-chip for the Rapid Identification of Candidate Antiviral Therapeutics and Prophylactics, Nature Biomedical Engineering (2021).

[56] E.Y. Bissonnette, J.F. Lauzon-Joset, J.S. Debley, S.F. Ziegler, Cross-Talk Between Alveolar Macrophages and Lung Epithelial Cells is Essential to Maintain Lung Homeostasis, Frontiers in Immunology 11 (2020).

[57] R.R. Mercer, J.F. Scabilloni, A.F. Hubbs, L.A. Battelli, W. McKinney, S. Friend, M.G. Wolfarth, M. Andrew, V. Castranova, D.W. Porter, Distribution and Fibrotic

Response Following Inhalation Exposure to Multi-walled Carbon Nanotubes, Particle and Fibre Toxicology 10 (2013) 33.

[58] S. Luanpitpong, L. Wang, A. Manke, K.H. Martin, A.G. Ammer, V. Castranova, Y. Yang, Y. Rojansakul, Induction of stemlike cells with fibrogenic properties by carbon nanotubes and its role in fibrogenesis, Nano Letters 14(6) (2014) 3110-6.

[59] K. Wang, X. He, W. Linthicum, R. Mezan, L. Wang, Y. Rojanasakul, Q. Wen, Y. Yang, Carbon Nanotubes Induced Fibrogenesis on Nanostructured Substrates, Environ Sci Nano 4(3) (2017) 689-699.

[60] G. Oberdörster, E. Oberdörster, J. Oberdörster, Nanotoxicology: an emerging discipline evolving from studies of ultrafine particles, Environmental health perspectives 113(7) (2005) 823-839.

[61] S. Hussain, S. Sangtian, S.M. Anderson, R.J. Snyder, J.D. Marshburn, A.B. Rice, J.C. Bonner, S. Garantziotis, Inflammasome activation in airway epithelial cells after multi-walled carbon nanotube exposure mediates a profibrotic response in lung fibroblasts, Particle and fibre toxicology 11(1) (2014) 1-16.

[62] D.W. Porter, A.F. Hubbs, R.R. Mercer, N. Wu, M.G. Wolfarth, K. Sriram, S. Leonard, L. Battelli, D. Schwegler-Berry, S. Friend, Mouse pulmonary dose-and time course-responses induced by exposure to multi-walled carbon nanotubes, Toxicology 269(2-3) (2010) 136-147.

[63] P. Ruenraroengsak, S. Chen, S. Hu, J. Melbourne, S. Sweeney, A.J. Thorley, J.N. Skepper, M.S.P. Shaffer, T.D. Tetley, A.E. Porter, Translocation of functionalized multi-walled carbon nanotubes across human pulmonary alveolar epithelium: dominant role of epithelial type 1 cells, ACS nano 10(5) (2016) 5070-5085.

CHAPTER 6

RECOMMENDATIONS

6.1 Refinement of the Lung Alveolus Chip

The lung is a complex organ performing various functions. The complexity presents challenges in creating accurate *in vitro* models, and many factors need to be considered for producing the models, such as the anatomy structure, ECM stiffness, topography, and mechanical stretch.

Anatomically, the lung alveoli are surrounded by the pulmonary capillary network, responsible for exchanging oxygen and nutrients with the lung tissues. Disruptions in the blood network can lead to various lung disorders, including lung cancer, pulmonary hypertension, and other diseases that impact the blood vessels in the lung. Instead of the interstitium, most current *in vitro* lung models focused on the co-culture of alveolar epithelium and capillary endothelium on the apical and basal sides of a membrane.[1-5]

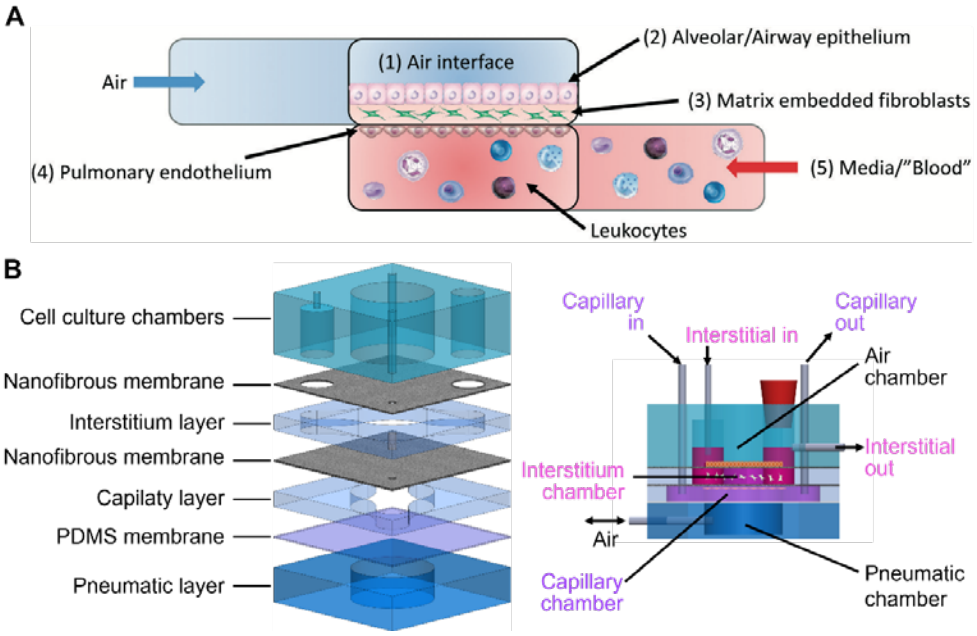

Figure 6.1: Illustrations of Lung Alveolus Chips. (A) Illustration of a desirable alveolar chip.[6] (B) Illustration of a more complex lung alveolus chip by incorporating capillary layer to the lung alveolar interstitium chip.

Considering the importance of these anatomy structures for lung integrity, function, and homeostasis, a desirable alveolar chip may consist of a co-culture of the alveolar epithelium, fibroblasts embedded in 3D matrix, and capillary endothelium, as shown in Figure 6.1A.[6] The alveolar epithelium can be exposed to an air-liquid interface with desired airflow. The cell culture medium can be perfused through the capillary channel to provide nutrition and desired shear stress. A more complex and physiological relevant lung alveolus chip can be produced by incorporating the capillary endothelium and the capillary channel to the alveolar interstitium chip. Moreover, the chip also provides interstitial flow and 3D mechanical stretch of physiological relevance (Figure 6.1B).

The ECM microenvironment may vary in different physiological and pathological environments. the alterations in alveolar epithelial permeability may impact ECM homeostasis and fibroblast function, which were found in many lung diseases. For example, the increased stiffness of the ECM is one of the important characteristics of lung fibrosis and lung cancer, in which the Young's modulus could be up to 20-100 kPa and 20-30 kPa, respectively compared to 1-5 kPa in normal lung tissues.[7, 8] It has been suggested that the development of lung fibrosis results from the interaction between fibroblasts and the ECM.[9] Immune cells, including macrophages and neutrophils, and activated myofibroblasts contribute to epithelial cell apoptosis and ECM stiffening. The increased stiffness in turn induces fibroblast activation and epithelial cell apoptosis.[10] By modifying the stiffness of the interstitium and/or inducing macrophage and neutrophils, this chip has the potential to study fibrosis and lung cancer mechanism and treatment.

6.2 High-throughput Lung Alveolus Chip

The development of organ-on-chip technology enables the *in vitro* studies of

human biology and disease and the testing of potential drugs and treatments more quickly and accurately than traditional cell culture models and animal models. However, current organ-on-chip models are often developed at the expense of throughput and compatibility with standard data collection methods and industry workflow. This significantly limited the clinical and industrial application of organ-on-chip technology, and thus efforts have been made to incorporate organ-on-chip into high-throughput platforms.[11-14] For example, 96 single organ-on-chips have been incorporated into a 384 well plate. As shown in Figure 6.2, each chip contains a permeable membrane sandwiched between two microfluidic channels, allowing the co-culture of two different types of cells. The inlets and outlets of the top and bottom channels are connected to four neighboring wells of the 384-well plate, which act as the media reservoir for each chip. Four electrodes are also incorporated in the four wells for real-time electrical resistance measurement, and this 96-chip layout allows high content screening.[14]

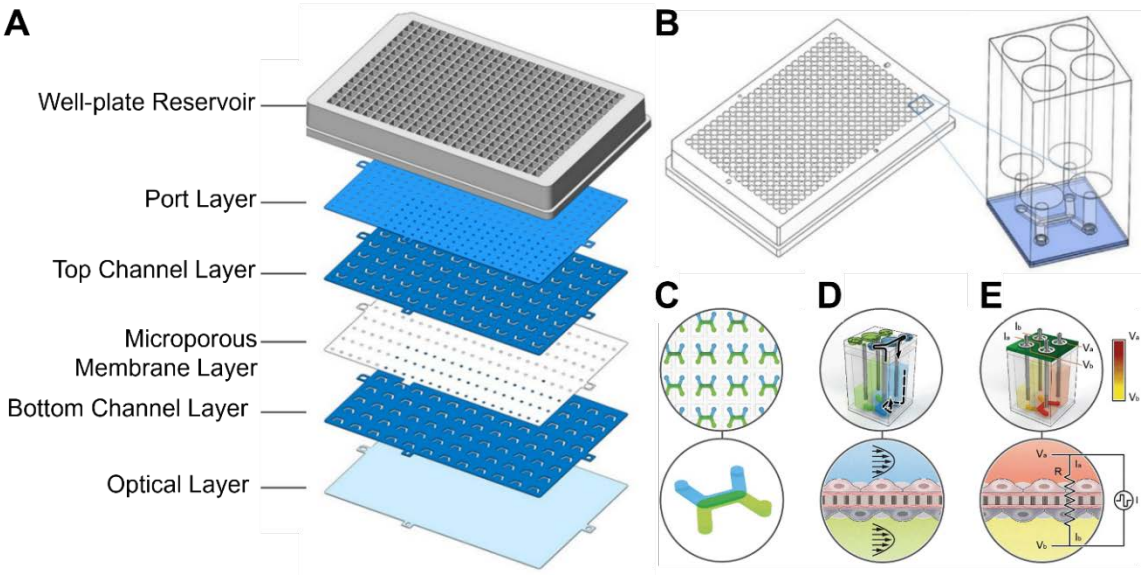

Figure 6.2: Illustration of a high throughput organ-on-chip platform. (A) Exploded view of the multi-layer platform. (B) The geometry of one organ-on-chip in the multi-well plate. (C) Each chip contained two channels separated by a permeable membrane. (D) Vertical tubes coupled to the wells provided fluid flow through the microchannels. (E) The tubes served as electrodes to measure tissue electrical resistance.[14]

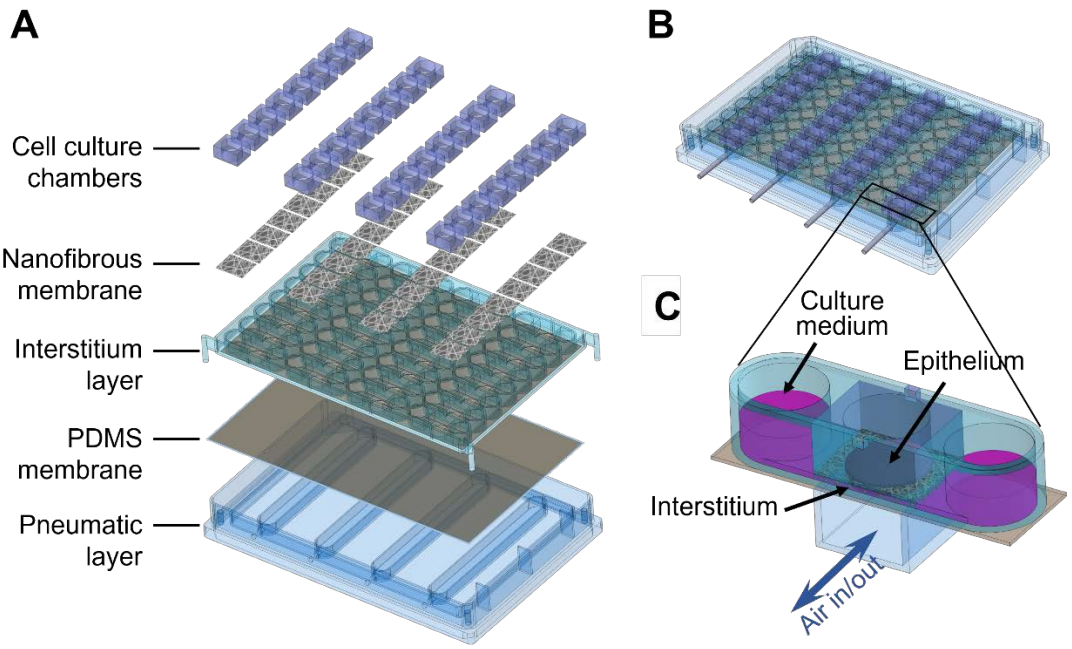

Figure 6.3: Illustration of high throughput lung interstitium chip platform. (A) Exploded view of the platform. (B) Assembled platform. (C) Single chip in the platform.

The lung interstitium chip can be modified and incorporated into a 96-well plate layout. As shown in Figure 6.3, the interstitium layer has a 96-well plate layout, with no wells in rows 2, 5, 8, and 11, and attached to the bottom PDMS membrane. Individual cell culture chambers are attached to the bottom nanofibrous membrane and inserted into the empty positions of the interstitium layer, with a gap of 1mm between the fibrous membrane and PDMS membrane. The pneumatic layer contains four pneumatic channels aligned with the cell culture chamber rows. This platform consists of 32 chips, each containing a cell culture chamber and two adjacent side wells serving as media reservoirs. The interstitium with fibroblasts can be injected through the side wells, and interstitium shear stress can be generated by placing the platform on a side-to-side rocker. This platform retains the characteristics of the individual chip, which closely intimates the key anatomical (epithelial cells co-cultured with fibroblasts encapsulated in 3D interstitial

matrix via nanofibrous membrane) and physiological (interstitium matrix stiffness, interstitial flow, and 3D breathing-like mechanical stretch) characteristics of human lung alveolus, while allowing high throughput screening.

6.3 References

[1] D. Huh, B.D. Matthews, A. Mammoto, M. Montoya-Zavala, H.Y. Hsin, D.E. Ingber, Reconstituting organ-level lung functions on a chip, Science 328(5986) (2010) 1662-8.

[2] D. Huh, D.C. Leslie, B.D. Matthews, J.P. Fraser, S. Jurek, G.A. Hamilton, K.S. Thorneloe, M.A. McAlexander, D.E. Ingber, A human disease model of drug toxicity-induced pulmonary edema in a lung-on-a-chip microdevice, Sci Transl Med 4(159) (2012) 159ra147.

[3] K.H. Benam, R. Novak, J. Nawroth, M. Hirano-Kobayashi, T.C. Ferrante, Y. Choe, R. Prantil-Baun, J.C. Weaver, A. Bahinski, K.K. Parker, Matched-comparative modeling of normal and diseased human airway responses using a microengineered breathing lung chip, Cell systems 3(5) (2016) 456-466.

[4] N.J. Douville, P. Zamankhan, Y.C. Tung, R. Li, B.L. Vaughan, C.F. Tai, J. White, P.J. Christensen, J.B. Grotberg, S. Takayama, Combination of fluid and solid mechanical stresses contribute to cell death and detachment in a microfluidic alveolar model, Lab Chip 11(4) (2011) 609-19.

[5] A.O. Stucki, J.D. Stucki, S.R. Hall, M. Felder, Y. Mermoud, R.A. Schmid, T. Geiser, O.T. Guenat, A lung-on-a-chip array with an integrated bio-inspired respiration mechanism, Lab Chip 15(5) (2015) 1302-10.

[6] G.R. Ainslie, M. Davis, L. Ewart, L.A. Lieberman, D.J. Rowlands, A.J. Thorley, G. Yoder, A.M. Ryan, Microphysiological lung models to evaluate the safety of new pharmaceutical modalities: a biopharmaceutical perspective, Lab on a Chip 19(19) (2019) 3152-3161.

[7] A. Miyazawa, S. Ito, S. Asano, I. Tanaka, M. Sato, M. Kondo, Y. Hasegawa, Regulation of PD-L1 expression by matrix stiffness in lung cancer cells, Biochem Biophys Res Commun 495(3) (2018) 2344-2349.

[8] K. Wang, L. Shi, W. Linthicum, K. Man, X. He, Q. Wen, L.W. Rojanasakul, Y. Rojanasakul, Y. Yang, Substrate Stiffness-Dependent Carbon Nanotube-Induced Lung Fibrogenesis, Nano Lett 19(8) (2019) 5443-5451.

[9] M.E. Blaauboer, F.R. Boeijen, C.L. Emson, S.M. Turner, B. Zandieh-Doulabi, R. Hanemaaijer, T.H. Smit, R. Stoop, V. Everts, Extracellular matrix proteins: a positive feedback loop in lung fibrosis?, Matrix Biol 34 (2014) 170-8.

[10] A. Camelo, R. Dunmore, M.A. Sleeman, D.L. Clarke, The epithelium in idiopathic pulmonary fibrosis: breaking the barrier, Frontiers in pharmacology 4 (2014) 173.

[11] J.C. Mejías, M.R. Nelson, O. Liseth, K. Roy, A 96-well format microvascularized human lung-on-a-chip platform for microphysiological modeling of fibrotic diseases, Lab on a Chip 20(19) (2020) 3601-3611.

[12] O. Jung, Y. T. Tung, E. Sim, Y. C. Chen, E. Lee, M. Ferrer, M.J. Song, Development of human-derived, three-dimensional respiratory epithelial tissue constructs with perfusable microvasculature on a high-throughput microfluidics screening platform, Biofabrication 14(2) (2022) 025012.

[13] N.R. Wevers, R. van Vught, K.J. Wilschut, A. Nicolas, C. Chiang, H.L. Lanz, S.J. Trietsch, J. Joore, P. Vulto, High-throughput compound evaluation on 3D networks of neurons and glia in a microfluidic platform, Scientific reports 6(1) (2016) 1-10.

[14] H. Azizgolshani, J. Coppeta, E. Vedula, E. Marr, B. Cain, R. Luu, M. Lech, S. Kann, T. Mulhern, V. Tandon, High-throughput organ-on-chip platform with integrated programmable fluid flow and real-time sensing for complex tissue models in drug development workflows, Lab on a Chip 21(8) (2021) 1454-1474.